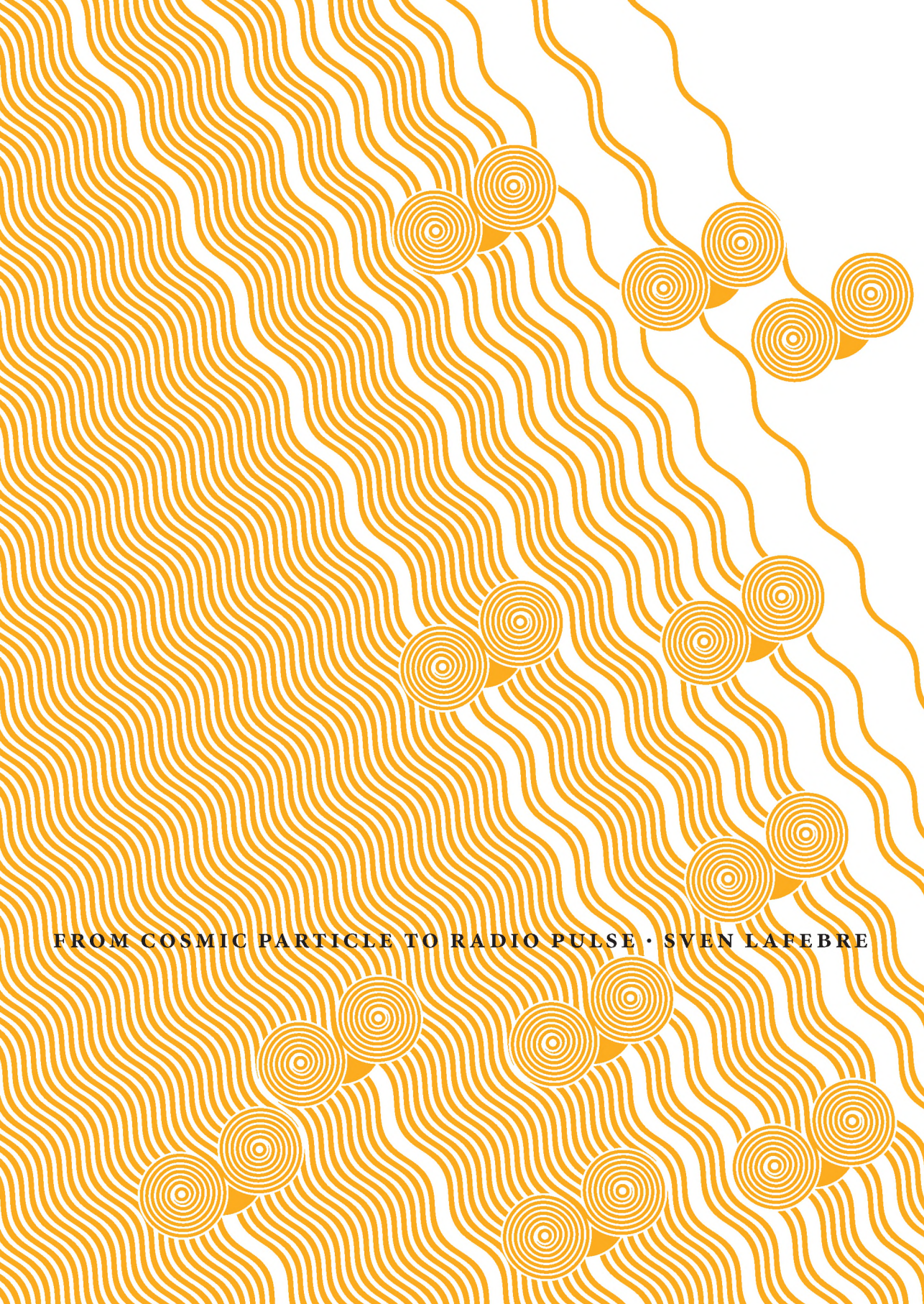
FROM COSMIC PARTICLE TO RADIO PULSE · SVEN LAFEBRE

FROM COSMIC PARTICLE TO RADIO PULSE

FROM COSMIC PARTICLE
TO RADIO PULSE

VAN KOSMISCH DEELTJE
TOT RADIOPULS

Een wetenschappelijke proeve
op het gebied van de Natuurwetenschappen,
Wiskunde en Informatica

PROEFSCHRIFT

ter verkrijging van de graad van doctor
aan de Radboud Universiteit Nijmegen
op gezag van de rector magnificus prof. mr. S.C.J.J. Kortmann,
volgens besluit van het College van Decanen
in het openbaar te verdedigen op vrijdag 19 december 2008
om 10:30 uur precies

door

SVEN JACOB LAFEBRE

geboren op 7 april 1980
te Tilburg

PROMOTORES	prof. dr. Heino Falcke
	prof. dr. Jan Kuijpers
MANUSCRIPTCOMMISSIE	prof. dr. Sijbrand de Jong
	dr. Jörg Hörandel
	dr. Tim Huege (Forschungszentrum Karlsruhe)

From cosmic particle to radio pulse
Thesis, Radboud University
Illustrated; with bibliographic references and summary in Dutch

ISBN 978·90·9023556·1

Set in 9/12 pt Minion using pdfLaTeX
Printed in the Netherlands

This work is part of the research programme of the 'Stichting voor Fundamenteel Onderzoek der Materie (FOM)', which is financially supported by the 'Nederlandse Organisatie voor Wetenschappelijk Onderzoek (NWO)'.

Citra stultitiae condimentum,
nullum omnino suave esse.

— DESIDERIUS ERASMUS
STULTICIÆ LAUS, 1509

Contents

1 · *Introduction*

1.1 · COSMIC PARTICLES

Nearly one hundred years ago, Austrian scientist Victor Hess embarked on a series of balloon flights to measure the amount of ionizing radiation at different altitudes. In those days, atmospheric ionization processes were attributed to radiation as a result of radioactive decay from particles in the Earth's crust, and it was expected that the amount of ionization would decrease with altitude. But as Hess and his balloon rose, so did the radiation levels he observed (Hess, 1912). His conclusion that some kind of radiation must come from the cosmos penetrating into our atmosphere earned him a Nobel Prize in 1936. The phenomenon he uncovered has since become known as *cosmic rays*, an amalgam of particles of diverse nature impinging on the Earth from space, such as protons, atomic nuclei, electrons, and high-energy photons and neutrinos. Therefore, most high-energy cosmic rays are in fact not rays at all, but hadronic in nature.

The full energy range of cosmic particles is enormous. It extends over many orders of magnitude from approximately 10^6 eV at the lowest end to 10^{20} eV at the highest boundary currently known. Low-energy cosmic particles are very common: on Earth, we receive a particle with an energy $> 10^{11}$ eV about once per square meter per second, but this number falls off dramatically to one per square meter per year at $> 10^{16}$ eV. At the highest energies $> 10^{19}$ eV, events are incredibly rare and a square kilometer only sees one of them per century on average (Cronin et al., 1997). Observing these isolated incidents is a very challenging process.

Where and how are cosmic particles produced? This is one of the most basic topics in the field of astroparticle physics, but even after decades of research, there is no universally accepted theory answering this question. We can distinguish three classes of sources, however, each of which is responsible for a different energy range of the cosmic-ray spectrum.

For the lowest energies, up to about 10^{10} eV, the bulk of cosmic particles received on Earth are produced in Solar flares. At higher energies, the picture becomes less transparent. Up to about 10^{18} eV, the most likely candidate sources of cosmic particles are to be sought outside the Solar system, but still within our own Galaxy because of the confinement of particles at these energies by the interstellar magnetic field to our own Milky Way and its halo. Recently, the advent of gamma-ray telescopes such as HESS

(Aharonian et al., 2005) and MAGIC (Albert et al., 2006) have supported the scenario of particle acceleration at shock fronts of supernova remnants throughout the Galaxy. For the first time, this development has allowed astroparticle physicists to do astronomical observations using high-energy particles in the energy range around 10^{12} eV, looking at sources rather than merely detecting single-particle events.

Only the fiercest sources in the universe, absent within our own Galaxy, are capable of producing particles with energies above 10^{16} eV. Two classes of theoretical models have emerged to explain their existence. The so-called *bottom-up scenarios* advocate violent classical astrophysical sources as producers of these particles, such as gamma ray bursts, supermassive black holes, magnetars, or active galactic nuclei. The more exotic class of *top-down models* envisions ultra-high-energy cosmic rays as decay products of extremely massive particles. These massive particles are then either emitted by topological defects from the early universe, or they are themselves relics from the early universe, surviving until today. Other exotic explanations involve supersymmetric hadrons, nonstandard neutrinos or violations of Lorentz invariance.

Whatever their sources may be, actual cosmic-ray astronomy in which a source is studied by looking at its cosmic-ray signal is not yet possible at these ultra-high-energies because of the low number of particles that reaches Earth. What little we do know is that there is a correlation between the arrival directions of these particles and the distribution of matter in the local supercluster of galaxies (Abraham et al., 2007), allowing us to tentatively connect the highest-energy events to the more traditional sources. However, this is by no means a conclusive result.

1.2 · AIR SHOWERS

Although the cosmic-ray flux of particles with energies in excess of $\sim 10^{15}$ eV is too low to be measured directly in any realistic experiment, particles at these energies generate an *extensive air shower*. After traversing a certain distance through the atmosphere of the Earth, the cosmic-ray particle initiates a nuclear reaction as it collides with the nucleus of an atom present in the atmosphere. In this reaction several new particles are produced, each possessing a significant fraction of the original cosmic particle's energy. These secondary particles may, in turn, initiate collisions with other atmospheric nuclei

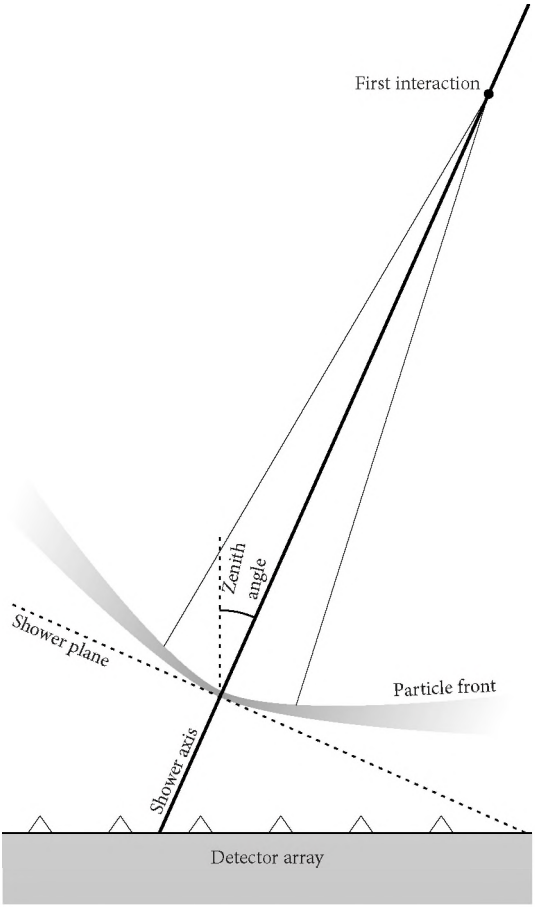

FIG. 1.1 · Schematic view of the geometry of an air shower. The particle front is only a few meters thick in the center.

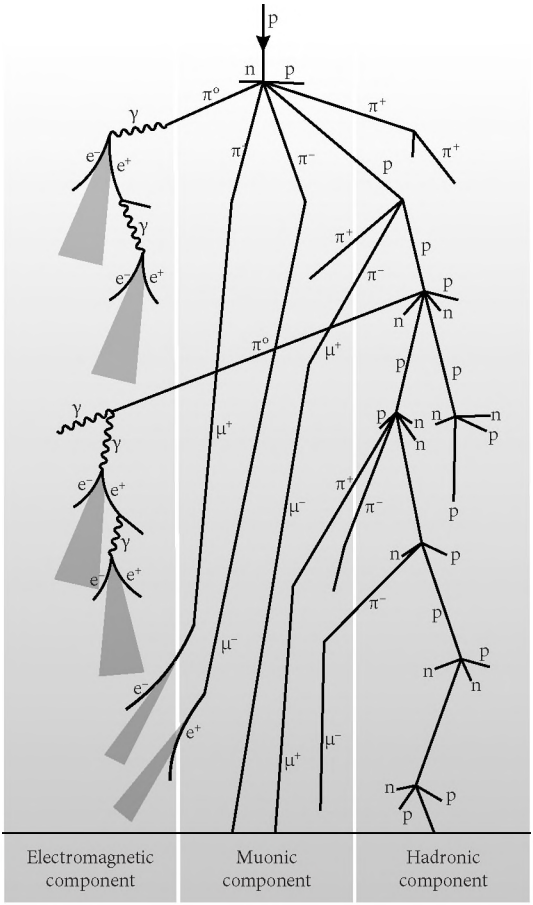

FIG. 1.2 · Overview of the various particle production channels in the three main components in a proton-induced air shower.

etcetera, resulting in a cascade of all kinds of particles. The number of particles scales nearly linearly with the primary cosmic ray's energy. Typically, the maximum number of leptons in an air shower initiated by a 10^{19} eV proton reaches approximately 6.5 billion.

Because of the momentum and energy of the initial cosmic ray, the secondary particles rush down through the atmosphere at nearly the speed of light. They are clustered in a thin layer, which is no more than a few meters thick in the center, and up to a few hundred meters near the outer rim; this is shown schematically in Fig. 1.1. This pancake of particles can extend up to several kilometers in diameter depending on the energy of the initial cosmic particle.

The basic physical principles behind extensive air showers have been studied for quite some time. More than sixty years ago, Rossi & Greisen (1941) derived equations for the structure of electromagnetic cascades on theoretical grounds. This description involves coupled equations of production and loss terms for different particle species. An excellent review of air shower physics is provided by Gaisser (1990).

There is a large number of possible creation and decay channels for each of the particle species in an air shower. Some of the most important processes are drawn schematically in Fig. 1.2. In general, we can divide these processes into three largely independent components. The hadronic part, which is nearly absent in photon-induced air showers, consists mainly of light baryons and mesons, such as protons (p), neutrons (n), and pions ($\pi^{\pm}$, π°). The muonic part, comprising $\mu^{\pm}$ particles, provides the primary means of observing air showers in ground-based particle arrays, since muons have small cross-sections and will generally reach the Earth's surface without interactions. The third component is the electromagnetic part, the main contributing species of which are photons (γ), electrons (e^{-}) and positrons (e^{+}). This electromagnetic part of the air shower is generated nearly entirely by two basic processes: *pair creation*, in which a photon creates an $e^{\pm}$ pair, and *bremsstrahlung*, in which an electron or positron emits a photon. Both processes occur under the influence of the electromagnetic field of atmospheric atomic nuclei. At lower energies, other effects such as collisional losses and Compton scattering also come into play.

As an example of the theoretical treatment of air showers, let us consider the cascade equations for pair creation and bremsstrahlung only. Since these processes involve creation and destruction of a photon, a set of coupled transport equations describes the particle flux in the atmosphere. We can write down these equations for the number of photons n_γ and the number of electrons plus positrons n_e as a function of atmospheric depth X, defined in g/cm^2:

$$\frac{\mathrm{d}n_\gamma}{\mathrm{d}X} = -\frac{X_\circ}{\lambda_{\gamma\to e}} n_\gamma(\epsilon_\gamma, X) + \int_{\epsilon_\gamma}^{\infty} n_e(\epsilon_e', X) \frac{\mathrm{d}n_{e\to\gamma}}{\mathrm{d}\epsilon_\gamma\,\mathrm{d}X}\,\mathrm{d}\epsilon_e'$$

$$\frac{\mathrm{d}n_e}{\mathrm{d}X} = -\frac{X_\circ}{\lambda_{e\to\gamma}} n_e(\epsilon_e, X) + \int_{\epsilon_e}^{\infty} n_e(\epsilon_e', X) \frac{\mathrm{d}n_{e\to e}}{\mathrm{d}\epsilon_e\,\mathrm{d}X}\,\mathrm{d}\epsilon_e' + 2\int_{\epsilon_e}^{\infty} n_\gamma(\epsilon_\gamma', X) \frac{\mathrm{d}n_{\gamma\to e}}{\mathrm{d}\epsilon_e\,\mathrm{d}X}\,\mathrm{d}\epsilon_\gamma'$$

where $n_i(\epsilon, X)$ is the number of particles of type i with energy ϵ at depth X, and $X_\circ \simeq$

$36.7\,\mathrm{g/cm^2}$ is the radiation length for electrons in air. The first term on the right hand side in both equations is the loss term. The second term in the equation for $\mathrm{d}n_\gamma/\mathrm{d}X$ represents photon production through bremsstrahlung; the second and third terms for $\mathrm{d}n_\mathrm{e}/\mathrm{d}X$ represent production terms for bremsstrahlung and pair creation, respectively.

One can imagine that, in practice, it soon becomes hard to solve for the particle distributions in an air shower from such coupled equations analytically, especially when many different interactions and species are considered. Moreover, the transport equations given above are one-dimensional, and do not describe lateral particle distributions. Since the latter information is indispensable in simulations for experiments employing detector arrays, it is often more useful and more accurate to turn to Monte-Carlo methods instead. One such Monte-Carlo code is CORSIKA (Heck et al., 1998), originally conceived to aid the analysis of data from the KASCADE experiment (see page 7).

Chapter 2 of this thesis describes the adaptation and implementation of a version of CORSIKA that runs on a parallel supercomputer. This code was used in preparation for simulations of radio pulses to be observed with radio telescopes such asLOFAR(see sect. 1.6). Chapter 3 then exploits universal properties of extensive air showers to provide accurate multi-dimensional parameterizations of the electron and positron distributions in these simulations.

1.3 · OBSERVING COSMIC PARTICLES

Cosmic particles at low energies that do not produce a significant air shower are generally observed in the same basic way as Victor Hess did so many years ago. In this type of experiment, balloons or satellites are equipped with particle detectors allowing the cosmic-ray primaries to be observed directly. The great advantage of this kind of observation is that the particle energy and species can be derived accurately.

Moving to higher energies of more than 10^{13} eV the amount of events decreases rapidly, so other means have to be employed to investigate them. These techniques involve detecting the secondary particles in the extensive air shower and reconstructing the original particle's properties from such data, which results in less accurate findings.

In present-day air shower research, there are three well-established observing techniques. One of them, employed by the HESS and MAGIC telescopes, is the observation of optical Cherenkov emission. The particles in an air shower generally propagate faster than the local speed of light in the atmosphere. This gives rise to Cherenkov radiation, which can be seen as light on the ground in clear, moonless nights. If the Cherenkov track is detected by two or more telescopes, the source of the original particle can be traced back. Because the refractive index of the atmosphere is near unity, the radiation is emitted almost parallel to the direction of the particle, illuminating only a small patch on the ground, demanding a relatively high particle flux to obtain a significant number of sightings. This fact, and a low duty cycle of around 0.1, makes the technique useful only up to energies of about 10^{15} eV.

Another observing method involves registering the secondary particles in the air shower using particle detectors. One major advantage of this technique is that an enormous detection area can be covered by erecting only a few hundred detectors. At the highest energies, the most important current example of an experiment using this technique is the *Pierre Auger Observatory* (Abraham et al., 2004), which uses 1600 particle detectors to cover an area of approximately 3000 km^2. Though the duty cycles of such experiments are much higher than those of telescopes looking for optical signals, information about the original primary particle is obtained in a very indirect way. Estimates for the primary energy and species can only be made using complicated, model-dependent simulations. This is a useful technique for energies above 10^{14} eV.

As an air shower develops, the nitrogen molecules in the atmosphere are excited. With a third observation method the optical and ultraviolet fluorescence signal emitted by these nitrogen molecules is detected. Since this radiation is emitted essentially isotropically, the observer does not have to look into the beam of particles itself, increasing the effective observing area. In fact, a satellite such as the EUSO observatory (The EUSO Collaboration, 2004), will look down to see this effect in the atmosphere from the International Space Station. As with Cherenkov observations, integral information about the air shower is obtained, allowing a more direct reconstruction of the primary particle's energy. Similarly, its drawback is the limited duty cycle of around 10 %. The Pierre Auger Observatory employs air fluorescence detectors at the same time, combining these results with measurements from the particle detectors when possible. Since only a minimal fraction of an air shower's energy is emitted as fluorescence light, this technique of observing only works at very high energies above 10^{18} eV.

1.4 · RADIO EMISSION FROM AIR SHOWERS

A fourth, still somewhat experimental observation method is the detection of air showers using radio antennas. This method and its future realisation with LOFAR forms the main thread of this thesis. By now, it has been firmly established that air showers produce radio signals. As early as in the mid-sixties, several groups (Jelley & Fruin, 1965; Borzhkovskii et al., 1966; Allan & Jones, 1966) reported short sparks of radiation in the 30–100 MHz range in coincidence with traditional air shower measurements. The underlying theoretical principle, however, was never established convincingly. It was suggested by Askaryan (1962) that a negative charge excess in the shower as a result of annihilation of shower positrons would give rise to coherent Cherenkov emission as the remaining electrons traverse the atmosphere. Since the size of the region where this radiation is emitted is smaller than a wavelength at the frequencies mentioned, the radiation would be coherent, boosting the power of the received signal by the square of the number of particles.

At the Haverah Park array, a radio signal was indeed detected in conjunction with extensive air showers, but a dependence of this signal on the shower's angle with the Earth's magnetic field was found (Allan & Neat, 1967; Allan & Clay, 1969). This indicates that Askaryan-type emission probably does not dominate. By the late 1960s, the

governing view was that the electron-positron pairs, created continuously in air showers, are separated in the geomagnetic field, leading to a transverse current in the shower (Kahn & Lerche, 1966; Colgate, 1967). The dipole radiation produced by this current, when Lorentz-transformed into the Earth's reference frame, is beamed mainly in a narrow cone in the direction of propagation, compressed in time into a short electromagnetic pulse. A good review of the status in those days was written by Allan (1971). More experimental groups reported detections of air showers by means of radio emission well into the 1970s (Felgate & Stubbs, 1972; Mandolesi et al., 1976; Baggio et al., 1977), but after this initial burst of interest in the radio signal of air showers, there was a long silence until only a few years ago.

Today, it is believed that the most important contribution to the radio pulse is produced through *geosynchrotron radiation* (Falcke & Gorham, 2003). Trajectories of charged particles in an air shower, predominently electron-positron pairs, are slightly curved by the Earth's weak magnetic field. This gyrating motion will produce synchrotron radiation, which is emitted in a narrow cone in the direction of motion of the particles. Since the Lorentz-contracted thickness of the layer of particles travelling through the atmosphere is only a few meters, this radiation is expected to be coherent at frequencies up to ~ 100 MHz (Huege & Falcke, 2003), producing a signal power that does not depend linearly on to the number of particles but quadratically. The proposed geosynchrotron approach is probably equivalent to the previous hypotheses based on transverse currents.

It was not until the recent emergence of cheap computational power, allowing for Monte-Carlo calculations of the expected signal rather than analytical estimates (Dova, 1999), that a renewed theoretical interest has manifested itself in the radio-detection of extensive air showers. One of the tools developed to this end is a code to simulate *Radio Emission from Air Showers*, or simply REAS (Huege & Falcke, 2005b; Huege et al., 2007). This code takes distributions of electrons and positrons as input, which can be obtained either through a parameterized form, or in the form of output from air shower codes such as CORSIKA. Though its implementation is quite sophisticated, the basic concept behind REAS is very simple: for a number of locations on the ground, the expected electromagnetic field from the motion of a random charged particle in the air shower is calculated. This field is added to the contributions from other particles in the shower until enough statistics are accumulated.

In chapter 4 of this thesis a multi-dimensional parameterization of radio pulses computed by combining REAS simulations with the CORSIKA results from chapters 2 and 3. Chapter 5 presents the shape of the electromagnetic radio front as a function of distance from the primary particle's projected impact location. This is an important tool to estimate the depth at which an extensive air shower reaches its maximum.

The electromagnetic pulses calculated by the REAS code do not take every possible effect into account. Among the neglected contributions are:

Creation/annihilation radiation — When charged particles are created, a short pulse of radiation is emitted as the field of the new charge is established.

Cherenkov radiation — The atmosphere is approximated as a vacuum in terms of the pulse calculation (not for the particle distributions), neglecting a component of Cherenkov radiation from the energetic particles in an air shower.

Transition radiation — The transition of a charged particle from one medium into another causes its field shape to change. Since the atmosphere is not constant in density, traversing it can be seen as constantly entering a denser medium.

Charge excess — A moving charge produces a moving electric field. Since the overall charge of a shower becomes increasingly negative by positrons annihilating with atmospheric electrons, this produces a noticeable contribution as the shower traverses the atmosphere.

These omissions may seem justified by early experiments, which indicated that emission is probably geomagnetic in origin. Future observations such as with LOFAR will have to prove this conjecture.

Detecting air showers through their radio signal may be advantageous for a number of reasons. First of all, the antennas themselves are cheap and easy to deploy. Furthermore, radio waves undergo practically no attenuation in air: this allows one to see an integral signal over the entire shower evolution instead of the remaining particles at the observer level only. Additionally, contrary to for example Cherenkov or fluorescence detectors, radio antennas have a duty cycle which is nearly 100 %. All in all, radio observations of extensive air showers could potentially make very valuable additions to existing and future cosmic-ray experiments.

1.5 · THE LOPES PROJECT

A recent breakthrough experiment in the detection of air showers through their radio signature has been achieved wiht the *Lofar Prototype Station* or LOPES. As a proof-of-principle experiment for the geosynchrotron approach to radio emission from air showers, the LOPES array was erected in 2003 (Horneffer, 2006)at the site of KASCADE, the *Karlsruhe Shower Core and Array Detector* (Antoni et al., 2001), an established air shower experiment which employs both scintillators and calorimeters (see Fig. 1.3, left). To allow simultaneous data acquisition of particles and radio emission, the radio array was set up to be triggered by KASCADE.

LOPES currently consists of 30 simple dipole antennas, shown in the right panel of Fig. 1.3, similar to those used in LOFAR. The two arms of each dipole are bent downwards to form a Λ-shape, increasing the antenna's sensitivity towards the horizon. Though the antenna design assigns two of these dipoles per antenna, crossing in the center to obtain sensitivity to two polarisation directions, initially only dipoles in the east-west direction were inserted into the antenna frame.

Since the beginning of 2004, air shower events between 10^{16} and $10^{17.9}$ eV have been recorded, about one in thousand of which also produced an appreciable signal in the radio antennas. Analysis of a few years of data (Falcke et al., 2005) shows that there is a linear correlation between the number of muons in the shower (as measured

FIG. 1.3 · Overview of the KASCADE particle detector array (left) and one of the LOPES antennas (right) which were set up between the particle detectors.

by Kascade) and the radio pulse height (as measured by LOPES); see Fig. 1.4. Additionally, a correlation between the received signal and the geomagnetic field was reported. These are two important results: the latter is a confirmation of the geomagnetic origin of the emission, and the former validates the assumption of the effect being coherent.

1.6 · THE LOFAR TELESCOPE

In the rural north of the Netherlands a new and unconventional radio telescope is being erected (Röttgering, 2003). This telescope, LOFAR or *Low Frequency Array*, will consist of a dense core of several kilometers in diameter (cf. Fig. 6.1 on page 93), containing approximately 3000 simple dipole antennas, a prototype of which is shown in Fig. 1.5. This compact core will be complemented by at least 17 remote stations, each with a diameter of 100 m, containing 48 low-band antennas each. The current funding supports an extent of the array to ~ 100 km, but the modular design of hardware and software allows the addition of further stations at a later stage.

The total bandwidth of 30–240 MHz is covered by two types of antennas, which are tuned to 30–80 MHz and 110–240 MHz respectively. The interference-saturated FM band is excluded. The signals of all antennas are combined using software rather than hardware, making the entire telescope incredibly flexible and versatile compared to conventional radio dishes. LOFAR development is currently in its final test phase, with the first antennas in the field, and the first serious scientific observations are expected to take place as of spring 2009.

There are four key astrophysical projects within the LOFAR science case, three of which propose to observe astronomical objects. The first project, and also the main

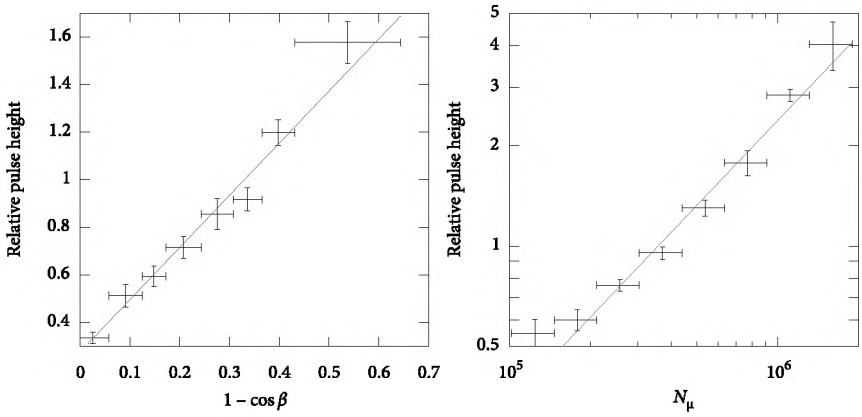

FIG. 1.4 · Correlation between pulse heights measured by LOPES and geomagnetic field angle β (left) and muon number N_μ as reconstructed by KASCADE(right). (Reproduced from Horneffer (2006).)

reason for LOFAR's conception, involves the *age of reionization*. It is believed that at redshifts between 6 and 12, the neutral hydrogen in the universe was ionized by radiation from the first stars and galaxies being formed: the redshifted hydrogen line from that epoch is hoped to be visible in the LOFAR frequency range. The 'clumpiness' of the H and H^+ regions will provide information on the formation of the first galaxies.

A second LOFAR goal will be to carry out *large-scale all-sky surveys*. Deep surveys of the accessible sky at LOFAR's entire frequency range will provide catalogues of radio sources for investigating fundamental areas of astrophysics, such as clusters of galaxies and the formation of massive black holes. As these surveys will probe unexplored parameter space, it is likely that they will unveil new phenomena.

The third project depends critically on the large, instantaneous beam and high time resolution, which will make LOFAR uniquely suited to monitor a large fraction of the sky simultaneously. This would, for the first time, allow an unbiased survey of *radio transients*, providing information on time scales ranging from seconds to many days, on sources from extragalactic gamma ray burst afterglows to exoplanets. Preliminary studies for using radio interferometers to detect radio flares at large angular resolution were carried out by Nigl (2007).

The fourth project addresses the study of high-energy cosmic rays. With the principle of radio emission from air showers confirmed by LOPES, we will now use LOFAR to take measurements in a broader energy range. LOFAR's large sky coverage and high time resolution make it ideally suited for the study of short, unpredictable phenomena like cosmic-ray events. The array will constitute a significant detection area of 0.26 km^2 sr,

FIG. 1.5 · View of some of the antennas in LOFAR's initial test station, showing the average distance between the antennas.

and will be densely populated. The array is expected to be sensitive to the signals from air showers initiated by cosmic particles in the range of 10^{15} to 10^{19} eV.

One of the major differences with LOPES is that we cannot rely on an external trigger for cosmic-ray detection. Instead, a radio-only trigger has to be devised. Various scenarios have been designed for different energy scales. For the lowest energies, at 10^{15} to 10^{17} eV, radio pulses from air showers are too weak for individual antennas to be picked up. By forming a wide beam using multiple antennas however, the detection threshold can be lowered at the cost of sky coverage. For energies between 10^{17} and 10^{19} eV, the produced radio pulse is bright enough to be picked up by individual antennas. To detect them, the signals of some of the dipoles will be monitored for short pulses continuously. The detailed description of this trigger is the subject of chapter 6 of this thesis.

1.7 · FURTHER INITIATIVES

An alternative way of deriving primary particle species is by studying simultaneous air shower events, measured a distance of several kilometers apart but coming from the same direction. These events could be the result of compound hadronic cosmic particles disintegrating in the Solar photon field. A study of this effect in chapter 7 shows that such events occur quite frequently. Realistic event rates in current air shower experiments are expected to be negligible, however, leaving actual composition determination through this effect for the far future.

To further investigate radio signals from extensive air showers, there are advanced plans to erect radio antennas inside the Pierre Auger array as well (Van den Berg & et al., 2007). This project would extend the energy range of radio detection of

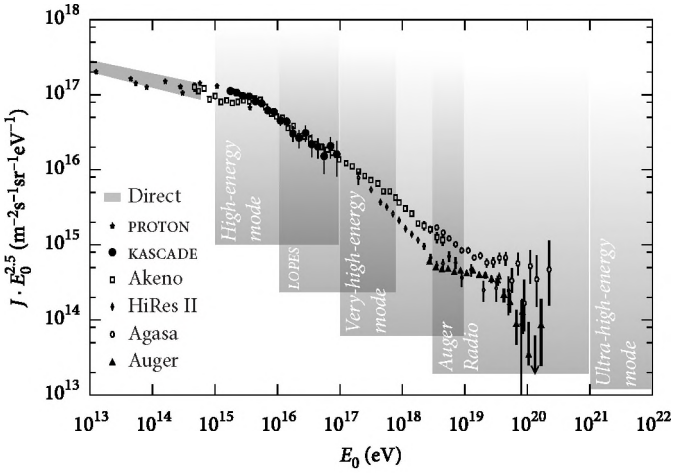

FIG. 1.6 · Overview of the various cosmic ray observation modes for LOFAR and connected experiments, together covering the entire energy range from 10^{15} to 10^{22} eV. Superimposed are the results of cosmic-particle flux measurements by selected experiments.

cosmic rays to $\sim 10^{21}$ eV, and provide valuable complementary data on shower evolution.

For the very highest energies of 10^{21} eV and above, the cosmic-ray flux is too low for a detector with an effective area like LOFAR's to expect a significant number of events. However, the LOFAR telescope permits using the entire volume of the Moon as a detector for both cosmic rays and neutrinos above 10^{21} eV (Scholten et al., 2006). Since our satellite has no atmosphere, cosmic rays smash right into the surface. Inside the Lunar regolith, the particle would initiate a confined shower, giving rise to Cherenkov radiation which, depending on angle and wavelength, can escape from the Moon and emerge from the surface. The flash would be very brief, but bright enough to be visible from Earth. The optimal wavelength to look for this phenomenon would be around 300 MHz. This approach could be used for the detection of neutrinos as well, which would have a reasonable chance of interaction when traversing the Moon.

The combined LOPES, LOFAR, and Radio Auger projects would enable the direct study of cosmic rays in the continuous range from 10^{15} eV all the way up to as yet unexplored energies of 10^{22} eV, as shown in Fig. 1.6, possibly establishing radio detection as a new reliable means to study cosmic-ray air showers.

2 · *The LOFAR air shower front evolution library*

S. Lafebre, T. Huege, H. Falcke, and J. Kuijpers

This chapter is an updated and expanded version of Lafebre et al. (2007)

We describe the considerations for and implementation of an altered version of the CORSIKA air shower simulation code, which runs on normal and parallel computers. The existing CORSIKA code was adapted and extended in such a way that it can run multiple showers concurrently. This code produces output suitable for simulating secondary radiation effects from air showers by producing particle distributions throughout the atmosphere as opposed to the particle flux on ground level only. A statistical test, comparing longitudinal and lateral spatial distributions and energy distributions of a sample of 1000 showers, proved the results on a BlueGene supercomputer to be compatible with those obtained with conventional CORSIKA output. We produced accurate parameterizations of the spatial and energy distributions of this sample. The code we have developed is suitable for mass-production of air shower simulations, and we will use it in future simulations for radio detection of air showers with LOFAR.

2.1 · INTRODUCTION

Recently, the development of digital radio telescopes such as LOFAR (Bregman, 2000; Falcke et al., 2006) has initiated a wave of renewed interest in the coherent radio emission from cosmic-ray air showers (Falcke & Gorham, 2003). This phenomenon was originally predicted by Askaryan (1965) and confirmed by Jelley & Fruin (1965) using an array of simple radio antennas. Though the phenomenon has been experimentally reconfirmed lately (Falcke et al., 2005; Ardouin et al., 2005), some details of the mechanism need further study. In order to fill this gap, a series of air shower simulations was carried out recently, which successively used an analytical approach (Huege & Falcke, 2003), a parameterized particle distribution (Huege & Falcke, 2005a) and particle histograms from CORSIKA (Huege et al., 2007), a popular code to simulate extensive air showers (Heck et al., 1998). The CORSIKA-based geosynchrotron simulations employ a realistic description of the air shower properties on a shower-to-shower basis, and we intend to pursue this approach further by running shower simulations for the development of cosmic-ray detection with the LOFAR poject.

To obtain a statistically meaningful confidence level of the results over the entire parameter range of configurations we want to test (primary energies, zenith angles, particle types), the calculation time of the simulations greatly exceeds the computational capacity of conventional machines. The projected run time of all simulations we intend to do would be around 30 years, for example, on current off-the-shelf desktop PCs. Unfortunately, using existing air shower libraries is not an option either: these libraries commonly only consist of histograms or distributions of particles on the lowest observation level, usually the Earth's surface. Since the radio emission we are interested in is believed to originate from charged particles in the atmosphere (Huege & Falcke, 2003), such libraries are are not suited for radio emission simulations. We therefore have to build our own library, and have to rely on supercomputers such as the recently installed BlueGene machine for LOFAR (Van der Schaaf et al., 2004), named *Stella* (Supercomputer Technology for Linked LOFAR Applications). This supercomputer is intended to perform cross-correlations and other data analysis for the LOFAR telescope, but as there is a significant time window between the installation of the supercomputer and the full operation

of LOFAR, there is considerable calculation time available on this machine. This was an extra incentive to start this project.

In this work, we describe the implementation of an adapted CORSIKA version which works on this supercomputer, and we demonstrate that the results it produces are valid and accurate. Additionally, we present an improved longitudinal parameterization of the test sample of shower simulations we performed.

2.2 · AVAILABLE INFRASTRUCTURE

The Stella BlueGene/L supercomputer consists of 12 288 nodes, distributed over six 19″ racks, reaching a peak processing power of about 30 Tflops/s for the entire machine. It is divided into 'partitions' of 1024, 512 and 256 compute nodes, to allow multiple jobs to be run at the same time. Each node consists of a 700 MHz PowerPC 440 processor with two floating point lines and 512 MBytes of memory. On each node, a minimal Linux operating system runs. This operating system can run only one single user process per node: this means that system call functions and multithreading in a user process are not supported on these processors. Direct communication between nodes is done exclusively through MPI, the *Message Passing Interface* standard (Walker, 1994). For Stella, all compiling is done with the GNU project C/C++ and Fortran compilers, version 3.4.3.

To test our implementation locally, we had access to two small computer clusters. The first cluster has 6 3.6 GHz Pentium IV processors running a 32 bit Linux operating system. We will identify this cluster as A throughout this paper. On this cluster, we used the GNU compilers version 3.3.4 and the mpich version 1.2.6 implementation of MPI. The other cluster, denoted B, has 10 3.0 GHz Pentium IV processors and runs a 64 bit Linux operating system. The installed GNU compilers are version 3.4.5 and LAM/MPI version 7.0.6 provides the MPI interface.

The A and B clusters were used in the development phase of the code, which will be treated in the next section. We also used them for our analysis in Sects. 2.4 and 2.5.

2.3 · IMPLEMENTATION

There are several ways to implement a parallel version of an existing code. The easiest solution is to tie different processes of the program together using a scripting language such as Perl or Bash that spawns processes to the different nodes as they are available. The major advantage of using this approach is that it can be implemented in a matter of weeks and that it can be adapted easily to make parallel versions of other codes. A disadvantage is that most supercomputing facilities, including Stella, do not support these scripting solutions: they require that only one binary is running on every node. System calls to create additional processes are not allowed.

The most elegant implementation, on the other hand, is producing one fully parallelized binary, which communicates with other processor nodes to determine work packages to be done and to share results. One obvious advantage is the sequential shower output; instead of producing a few hundred showers every fifty hours or so, this setup

would produce one shower every few minutes. On the face of it, such an approach seems particularly suitable in the case of air shower simulations, since they can be distributed over many processors without much trouble by splitting them into subshowers. As the amount of particles in an air shower may easily reach billions, the number of subshowers would always exceed the number of nodes, ensuring the availability of work for all nodes at all times.

Implementing such a CORSIKA version might not be easy, however. One problem one would definitely run into, is providing the random numbers for the simulation. In standard CORSIKA, random numbers are taken sequentially from a series. Sharing one sequence across nodes is not an option in a parallel implementation, since the order in which nodes request random numbers might change when the simulation is repeated, even when the number of nodes remains the same. Providing each node with a separate random number sequence might be a better choice, but one has to make sure jobs are distributed across nodes in a unique way, which would be an incredibly difficult task for parallel computers of different geometries. Ensuring reproducibility will be, in our opinion, the crucial problem in a fully parallelized CORSIKA version and implementing and testing a solution would certainly take several years of manpower.

As a tradeoff, we decided to produce a single binary which acts like a script, but which makes *function* calls to a CORSIKA routine instead of *system* calls to the CORSIKA binary. This way, we could obey the strict conditions, but we were still able to finish the adaptations within a reasonable amount of time. Within the chosen solution, different components can be identified: a wrapper, which does the bookkeeping and distribution, and the CORSIKA routines, in which the actual calculations are done.

The communication between the different nodes with one another is done via the Message Passing Interface (MPI). The wide support and availability of this standard ensures that our code can be run without problems on other machines in the future. Additionally, this is the preferred way for node communication on Stella.

In distributed programming, some sort of bookkeeping needs to be done: work packages need to be handed out, finished jobs should be marked as such and all processors should be kept busy at all times. Two ways of bookkeeping were considered here. In the first method all the necessary information is kept at every node. This information is updated locally whenever a change occurs, after which this change is passed around to the other nodes. This method requires that all nodes are made aware of such notifications, even when they are working on something else. Alternatively, there can be a 'master node' that does not run any simulations: its only task is to ditribute the work packages to the other nodes and to wait for signals from them as their jobs finish. Though obviously less efficient, as one node is permanently unused, this method is preferred because of its simplicity. One should also take into consideration that we expect to run the code on partitions consisting of as many as 1024 nodes, making such a loss practically negligible.

When the wrapper is started, one of the available nodes is designated to take on the role of master node. First of all, this node should know what showers should be simulated. This information is read in from a file containing the configuration parameters for a simulation: primary particle energy, type and entrance zenith and azimuth angles, as well as the number of simulations to be run with these parameters. All other run parameters are either fixed or calculated from these. After obtaining the parameters for a work package, the master node waits for a message from a client node indicating it is free and accepting a new job. The master node answers such requests by sending the parameters for a simulation to be carried out. The client node will then start a simulation by making a call to the actual CORSIKA function. After this simulation finishes, it sends a message requesting a new work package. This cycle continues until there are no more work packages to hand out; in this case the master node tells free client nodes to do nothing and not to send any further job requests. When there are no more active client nodes, the master node exits the program.

Additionally, the master node keeps track of which work packages were handed out and which have been finished. It also marks corrupted jobs when an error was reported by a client node. This meta-information is written to a terminal or log file, which can be reviewed later by the user.

As stated earlier, the CORSIKA code was be altered in such a way that its main routine can be called as a function rather than a stand-alone program. The shower parameters are then forwarded as arguments to the CORSIKA function call. The code we adapted is CORSIKA version 6.5001, released on March 6, 2006. The options selected to prepare the base Fortran file were UNIX, BYTERECL, QGSJET, QGSII, URQMD, THIN, ROOTOUT and ROOTRACK. For a description of these options, see Heck & Knapp (2005). The interaction models used were QGSJET-II-03 for high-energy interactions and URQMD 1.3.1 for low energies. The lower energy cutoff for electrons and positrons was 0.4 MeV. A modified version of the *Corsika Data Access Tools* (COAST) was used to access the data of individual particles tracked in CORSIKA (Ulrich, 2007).

One of the problems encountered is that CORSIKA heavily relies on Fortran 'data blocks', structures that can be used across functions within the same program. Unfortunately, this also means that they are not re-initialized when several calls to the CORSIKA function are made sequentially in the same process. Where this caused problems, we substituted the data block initialisation with run-time initialisations manually. The different interaction model codes used by CORSIKA also suffered from this problem and we applied the same patch there.

Another problem are the frequent calls to Fortran 'stop' statements in the CORSIKA code. When a 'stop' is called the process ends, and the client node never reports back to the master node. Instead, the client node should report an error to the master node in such an event and ask for a new simulation to be done. This was solved by substituting all 'stop' statements with a call to a function that communicates the error to the server node and tries to abort the simulation in a more controlled way.

Since the non-static run parameters for the simulations are already passed to CORSIKA by means of function arguments, they should be ignored when reading the data card which contains the static directives for running the simulation. Parsing of the keywords ERANGE, NSHOW, OBSLEV, PHIP, PRMPAR, RUNNR and THETAP, as well as the second parameter of the THIN keyword, is therefore blocked and a warning is written to the log file instead. A description of the various keywords in CORSIKA can be found in Heck & Knapp (2005).

There were numerous other small changes to the original CORSIKA code, which we will not discuss here; a full list of changes is available from the author. Simulations in the library can be downloaded from the author's website.[1]

2.4 · RUNNING AND TESTING THE CODE

To test the validity and reliability of the results obtained with our code, we made comparisons between identical showers simulated by, respectively, standard CORSIKA and the parallel version with exactly the same run directives (including random seed), on the same architecture. In this case, we used cluster A. As might be expected, the resulting output files and histograms are identical as long as both CORSIKA codes are compiled with similar compiler options. It is therefore concluded that our code produces valid results on this architecture. From here on, when we speak of comparisons between Stella simulations and 'valid' code, we have compared results of the adapted CORSIKA code on Stella with the adapted (but valid) CORSIKA code on cluster A.

We compared several showers which were simulated on Stella with a set that was generated on cluster A, again with the same run directives. These showers turned out *not* to be identical: most likely, this is due to the fact that numbers may be rounded in a slightly different way on systems with a different architecture, even when the different codes were compiled by the same compiler with exactly the same parameters. Such a small deviation may manifest itself once in a while in a different decision at some point (for example in the creation of different collision products), after which the entire evolution from that point onward will be completely different. This even extends to other subshowers, as the number of values taken from the random number sequence will probably be different as well.

An illustration of this effect is given in Fig. 2.1, where we show two longitudinal profiles $N(X)$ for the sum of electrons and positrons as a function of the atmospheric depth X. In this plot, we show a shower induced by a proton with an energy of $E = 10^{16}$ eV, azimuth angle $\phi_0 = 0$ and zenith angle $\theta_0 = 0$, e.g. straight from above. Though the run directives were identical, including random seeds, clearly the profiles are not, although they resemble each other somewhat. This behaviour is typical for the entire sample when comparing showers from different architectures.

Because the results we obtain on different architectures are not identical, we need to turn to statistical methods to see whether the simulations on Stella architecture

[1] http://www.astro.ru.nl/~svenlafe/research/lasfel

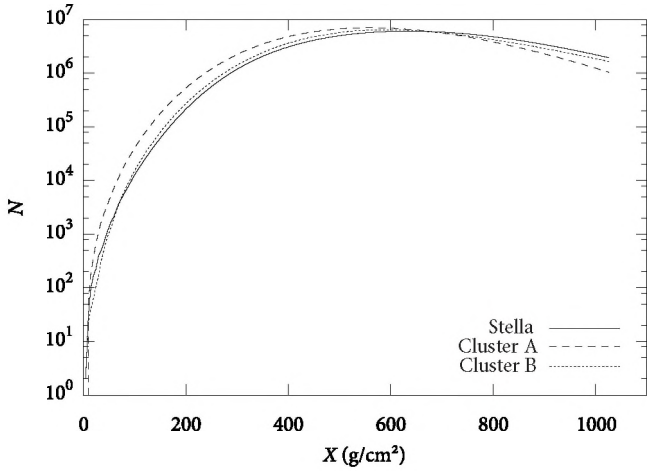

FIG. 2.1 · Example of a longitudinal profile of the sum of electrons and positrons in a proton-induced shower of 10^{16} eV. Three showers were run with the same run directives and random seed, but on different architectures. Though the agreement is better than one would expect statistically, the profiles are far from identical.

produce accurate results. It was decided to run a test batch of 1000 showers with the same run parameters (but with varying random seeds) on three different architectures and perform some statistical comparison tests on the results to check validity. Adding a third, independent architecture (cluster B) allowed us to get an unbiased idea of the differences to be expected. The difference between clusters A and B is very small: cluster A has a 32 bit Intel architecture, while cluster B is 64 bit.

We chose to simulate proton showers at 10^{16} eV for our tests. Proton showers are statistically more diverse than for example iron showers, due to the lower primary mass, making comparisons between them a stricter criterion for statistical compatibility. The energy of 10^{16} eV was chosen to be at the intended lower end of our library's energy spectrum, so that the results of the simulations will be useful in themselves without taking too much time to produce. All particles were injected from zenith ($\theta_0 = 0$, $\phi_0 = 0$). The magnetic field strength was adjusted to suit the LOFAR core location, i.e. $B_{xy} = 18.6\,\mu\text{T}$, $B_z = 45.5\,\mu\text{T}$. We used 10^{-6} level optimum thinning (as explained in Pierre Auger Collaboration & Kobal (2001)) in order to cut calculation times, with a maximum weight of 10 per particle (see Heck & Knapp (2005) for an explanation of these parameters). The random number sequence for each shower was determined uniquely by the simulation number (0–999).

Running the simulations to obtain the test sample on a 1024 node partition on Stella took 82 hours in real time – the time to finish the most computationally intensive

TAB. 2.1 · Comparison of the average value of various shower observables over a sample of 1000 simulations for three architectures for different species in the air shower. From top to bottom, the number of particles arriving at detector level N_{sea}, the number of particles at shower maximum N_{max} and the atmospheric depth of the shower maximum X_{max} are compared. Errors indicate 1σ statistical confidence levels.

	Cluster	Species					
		γ	e^+	e^-	μ^+	μ^-	Hadrons
N_{sea}	Stella	$1.36 \pm 0.60 \cdot 10^7$	$0.65 \pm 0.33 \cdot 10^6$	$1.15 \pm 0.56 \cdot 10^6$	$3.86 \pm 0.77 \cdot 10^4$	$3.84 \pm 0.76 \cdot 10^4$	$0.84 \pm 0.38 \cdot 10^4$
	Cluster A	$1.35 \pm 0.62 \cdot 10^7$	$0.64 \pm 0.34 \cdot 10^6$	$1.14 \pm 0.58 \cdot 10^6$	$3.84 \pm 0.74 \cdot 10^4$	$3.82 \pm 0.73 \cdot 10^4$	$0.83 \pm 0.37 \cdot 10^4$
	Cluster B	$1.36 \pm 0.62 \cdot 10^7$	$0.65 \pm 0.34 \cdot 10^6$	$1.15 \pm 0.58 \cdot 10^4$	$3.86 \pm 0.76 \cdot 10^4$	$3.83 \pm 0.76 \cdot 10^4$	$0.84 \pm 0.39 \cdot 10^4$
N_{max}	Stella	$4.06 \pm 0.33 \cdot 10^7$	$2.43 \pm 0.21 \cdot 10^6$	$4.02 \pm 0.34 \cdot 10^6$	$4.28 \pm 0.76 \cdot 10^4$	$4.25 \pm 0.74 \cdot 10^4$	$2.18 \pm 0.41 \cdot 10^4$
	Cluster A	$4.07 \pm 0.33 \cdot 10^7$	$2.44 \pm 0.20 \cdot 10^6$	$4.04 \pm 0.33 \cdot 10^6$	$4.27 \pm 0.73 \cdot 10^4$	$4.25 \pm 0.72 \cdot 10^4$	$2.18 \pm 0.40 \cdot 10^4$
	Cluster B	$4.07 \pm 0.34 \cdot 10^7$	$2.44 \pm 0.21 \cdot 10^6$	$4.03 \pm 0.34 \cdot 10^6$	$4.28 \pm 0.75 \cdot 10^4$	$4.25 \pm 0.74 \cdot 10^4$	$2.19 \pm 0.41 \cdot 10^4$
X_{max} (g/cm^2)	Stella	667 ± 85	629 ± 86	640 ± 86	790 ± 91	791 ± 91	570 ± 89
	Cluster A	667 ± 83	629 ± 83	639 ± 83	793 ± 90	792 ± 90	572 ± 87
	Cluster B	665 ± 84	628 ± 84	638 ± 84	790 ± 91	789 ± 90	569 ± 87

simulation. The total summed calculation time for Stella was $71 \cdot 10^3$ hours. On cluster A, the real time was around 1100 hours ($7.3 \cdot 10^3$ hours summed calculation time) and around 460 hours ($9.3 \cdot 10^3$ hours summed) on cluster B. For an infinite amount of runs, performance on any n-node parallel machine scales with $n - 1$, as one node is used for bookkeeping. For a finite number of simulations, there is an overhead which is determined by the delays between nodes to finish their last run.

In the remainder of this section, we analyse and compare spatial and energy distributions from the simulated air showers.

The total number of particles arriving at detector level was compared first. For our simulations, the atmospheric depth of the detector level was calculated from the altitude of the LOFAR telescope, close to sea level, corresponding to $X \sim 1036\,\mathrm{g/cm^2}$ for vertical showers. This detector level distribution is a fair shower characteristic for primary energies from $\sim 10^{14}$ eV or so: showers above this energy deliver a significant number of particles onto the ground. For various species in the shower, this number was averaged over the ensemble of 1000 showers for the samples of different architectures. These fluxes are listed in the top part of Tab. 2.1.

Also shown in this table are the number of particles for each different shower component at its maximum $N_{\max}$, along with the atmospheric depth $X_{\max}$ belonging to this maximum for the different clusters. Differences between architectures are negligible for all components for all quantities, and it is not affected either on Stella as it lies well within the statistical error margin of the ensemble. For electrons and positrons, a first order theoretical approximation for the depth of the shower maximum is given by

$$X_{\max} = X_0 \ln \frac{E}{E_c}, \tag{2.1}$$

where $X_0 = 36.7\,\mathrm{g/cm^2}$ is the typical interaction length of an electron, and $E_c = 86$ MeV is the critical energy below which ionisation losses will dominate over bremsstrahlung photon production. For $E = 10^{16}$ eV, we find a theoretical value of $X_{\max} = 682\,\mathrm{g/cm^2}$, which lies well within our statistical errors.

In the remainder of this section, we focus on electrons and positrons in the shower only, as these are the dominant species in the production of the radio emission we intend to study. Therefore, When we speak of the number of particles from here on, we mean the sum of the number of positrons and electrons.

The number of particles in the shower along the entire longitudinal development was averaged over the atmospheric depth X for all 1000 showers in the sample for each architecture. The averaged longitudinal particle distributions obtained in this manner are shown in the top panel in Fig. 2.2. The bottom panel of this figure shows the deviation δ of each distribution from average of the other two. The solid line, for example, is given by

$$\delta_S = \frac{2N_S}{N_A + N_B} - 1, \tag{2.2}$$

where the indices S, A, B are for Stella and clusters A and B respectively.

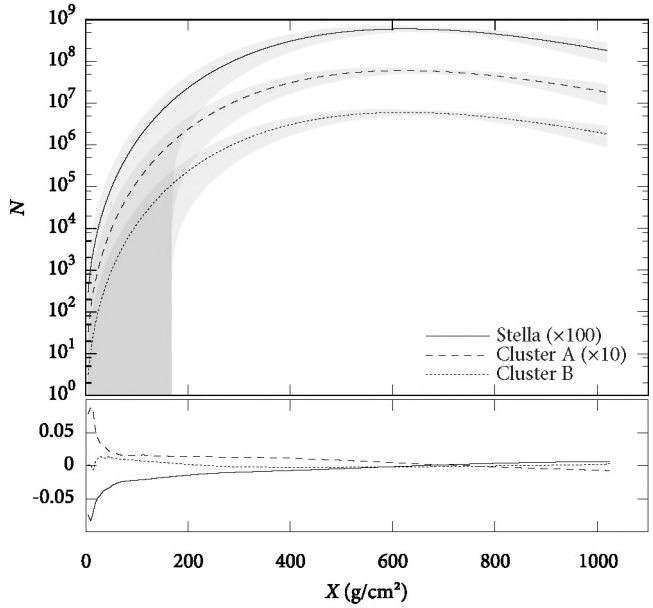

FIG. 2.2 · Averaged longitudinal profile of the sum of electrons and positrons for 1000 vertical proton-induced showers of 10^{16} eV. In the upper panel, the lines for cluster A and Stella have been shifted up by a factor of 10 and 100, respectively. The coloured areas mark 1σ statistical errors. The lower panel shows the relative difference of each longitudinal profile compared to the other two.

The rather large deviations of nearly 10 % for very low depths can be attributed to low number statistics, as the number of particles in the shower at these depths is no more than a few hundred. This is also reflected in the error margins in this figure, drawn as coloured areas in this figure. These areas indicate the 1σ statistical error level from 1000 runs. It is clear that the deviations between architectures lie well within this area, allowing us to conclude that no significant difference exists between clusters A and B on the one hand and Stella on the other.

The lateral particle distributions are plotted in Fig. 2.3. In this figure, the lateral particle density dN/dA in particles per m^2, averaged over all 1000 showers in the sample and all 50 observation levels, is plotted against the distance r to the shower axis. The lower panel again shows the deviation δ. Far away from the shower, the deviations can be attributed to statistical noise. For very small distances, though the number of particles is many orders of magnitudes higher, so is the spatial resolution used in the histograms, making the number of particles per bin much lower than at intermediate

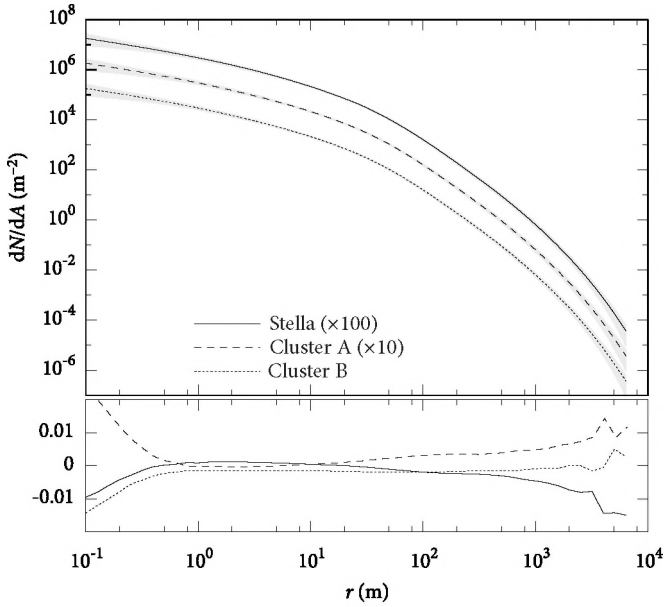

FIG. 2.3 · Lateral profile of the sum of electrons and positrons averaged over 1000 vertical proton-induced showers of 10^{16} eV, and averaged over 50 observation levels in the full shower evolution. As in Fig. 2.2, the lines for cluster A and Stella have been shifted up by factors of 10 and 100 to tell them apart and the lower panel shows the difference relative to the other two profiles.

distances of 10–100 m. As with the longitudinal distribution, the 1σ margins are much broader than the deviations between architectures, allowing us to conclude that there is no systematic error in the Stella results.

Fig. 2.4 shows the energy distribution of particles. In this figure, the particle energy density $dN/d\epsilon$ in particles per energy unit, averaged over the entire shower length and all 1000 showers in the sample, is plotted against the particle energy, together with the statistical spread. In the lower panel, each shower's deviation δ from the other two is shown. Note the indentation in the energy distribution at an energy of approximately $1.1{\cdot}10^6$ eV. The origin of this feature, which is obviously unphysical (cf. for example Nerling et al., 2006), is a bug in the Coast library that was unknown at the time the library was being constructed. The feature is present in Coast output from non-parallelized and parallelized CORSIKA alike. Since the geosynchrotron signal from air showers is mostly emitted by particles of higher energies, the feature does not have a significant effect on radio signal simulations performed from these histograms. This is explained in section 2.B

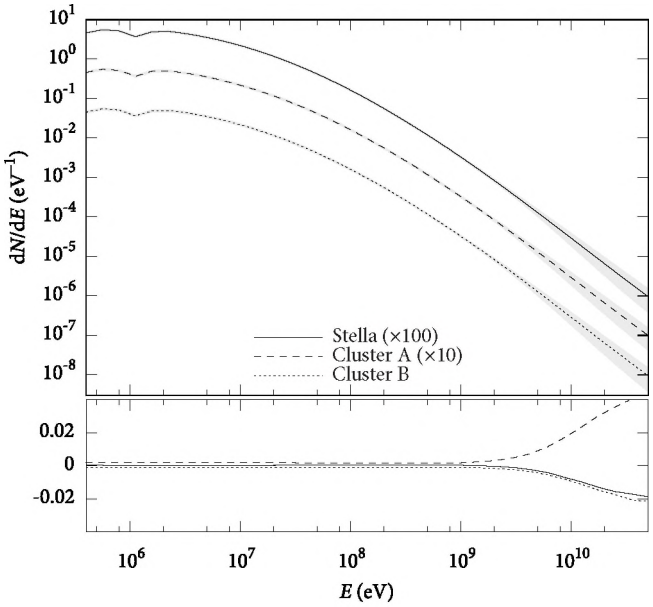

FIG. 2.4 · Averaged energy profile of the sum of electrons and positrons for 1000 vertical proton-induced showers of 10^{16} eV. Again, coloured areas show 1σ statistical error levels and lines for cluster A and Stella have been shifted up by factors of 10 and 100 to tell them apart.

on page 30.

The high number of particles at high energies for cluster A is striking and probably relates to the higher number of particles in the early shower development (see Fig. 2.2). This is not a significant difference compared to the statistical error margin, however, and we conclude that results for the three architectures are compatible.

In none of the comparative tests we carried out we could find any significant difference in the quantities involved or the statistical spread in them. We therefore conclude that the air shower simulation results we obtain with Stella are valid. The new code was employed to perform simulations used in chapters 3, 4, and 5 of this thesis.

2.5 · LONGITUDINAL SHOWER PROFILE

The sample of 3000 showers we obtained for validating Stella output is large enough in itself to use for analysis of extensive air showers at 10^{16} eV. In this section, we describe our efforts of parameterization of the particle histograms we obtained.

There are several well-known parameterizations of longitudinal air shower

profiles. One was introduced by Gaisser & Hillas (1978). It is given by

$$N(X) = N_{\max}\left(\frac{X}{X_{\max}}\right)^{X_{\max}/\lambda_H} \exp\left(\frac{X_{\max} - X}{\lambda_H}\right), \tag{2.3}$$

where λ_H is a characteristic length, fixed at 77 g/cm^2 in the original reference.

We performed a nonlinear least-squares fit for every individual shower profile for λ_G, $X_{\max}$ and $N_{\max}$. The average reconstructed values for each of the three parameters are:

$$\begin{aligned} \lambda_H &= 69 \pm 13\ \text{g/cm}^2, \\ X_{\max} &= 6.3 \pm 0.8 \cdot 10^2\ \text{g/cm}^2, \\ N_{\max} &= 6.4 \pm 0.5 \cdot 10^6. \end{aligned} \tag{2.4}$$

The average normalised residual of the fits is $(\chi/N_{\max})^2 = 9.0 \cdot 10^{-5}$. Given the distributions of the independently reconstructed parameters, these values represent an average shower quite well.

The cascade theory behind (2.3) demands that the first interaction point of the shower be at $X = 0$. Since this is generally not the case in Monte Carlo simulations, a variation of the parameterization allows the shower evolution to start from a variable first interaction point X_i, as opposed to a fixed point at the top of the atmosphere:

$$N(X) = N_{\max}\left(\frac{X - X_i}{X_{\max} - X_i}\right)^{X_{\max} - X_i/\lambda_H} \exp\left(\frac{X_{\max} - X}{\lambda_H}\right). \tag{2.5}$$

Allowing for such an extra degree of freedom was found to have no significant influence on the value of the other parameters. Moreover, the reconstructed value of X_i is not correlated with the actual first interaction point. For more than half of the fits the value is not even positive, making the addition doubtful from a physical point of view; incorporating the parameter X_i was therefore discarded. This confirms earlier findings by Pryke (2001) and Song (2004).

Another parameterization of the longitudinal particle distribution is the parameterization by Greisen (1960), which describes purely electromagnetic air showers. In the Greisen parameterization, the particle distribution is approximated by

$$N(X) = N_{\max} \exp\left(\frac{X - X_{\max}}{\lambda_G}\right) s^{-3X/2\lambda_G}. \tag{2.6}$$

Our definition here for $N(X)$ differs slightly from traditional representations in that it is written to explicitly show the physical quantity $N_{\max}$, the number of electrons and positrons in the shower at $X_{\max}$, which is an energy-dependent normalisation factor that can be written as

$$N_{\max} \equiv \frac{N_0 e^{X_{\max}/\lambda_G}}{\sqrt{\ln(E/E_c)}} = \frac{N_0 e^{X_{\max}/\lambda_G}}{\sqrt{X_{\max}/\lambda_G}}, \tag{2.7}$$

TAB. 2.4 · Performance of three parameterization schemes for longitudinal distributions. Values for ϵ_i are defined in (2.10). Variance reduction values $(\chi/N_{\max})^2$ are averaged over the entire sample.

Representation	ϵ_1	ϵ_2	ϵ_3	ϵ_4	ϵ_5	ϵ_6	$(\chi/N_{\max})^2$
Gaisser-Hillas	1.000	0.000	0.000	0.000	0.000	0.000	$9.0 \cdot 10^{-5}$
Greisen	1.000	0.000	0.037	0.056	0.062	0.062	$1.1 \cdot 10^{-4}$
This work	1.000	-0.013	0.005	0.053	0.181	0.207	$8.1 \cdot 10^{-5}$

where $N_0 = 0.31$. In (2.6), the shower age s is a normalised measure for the atmospheric depth, defined as

$$s(X) \equiv \frac{3X}{X + 2X_{\max}}. \tag{2.8}$$

By definition, $0 \leq s < 3$, where $s = 0$ corresponds to the top of the atmosphere, $s = 1$ at the shower maximum, and $s = 3$ at infinite atmospheric depth. The natural definition of s puts the point $s = 0$ at the first interaction point instead of the top of the atmosphere, but this point cannot be determined in observations.

Theoretically, for purely electromagnetic air showers, e.g. initiated by photons or electrons, one should find $\lambda_G = X_0 = 36.7\,\mathrm{g/cm^2}$. Particle production in such showers is limited to pair creation ($\gamma \to e^+ + e^-$) and bremsstrahlung ($e^\pm \to e^\pm + \gamma$). Using (2.1), we find for such showers that $X_{\max} = 682\,\mathrm{g/cm^2}$ and $N_{\max} = 5.6 \cdot 10^5$ on average, for a value of $N_0 = 0.31$. These values do not give a reasonable approximation of the curves in Fig. 2.2, however, since the proton showers in our sample have additional channels for creation of $e^\pm$ particles from the hadronic components. By varying the value of λ_G, however, we can an reconstruct the profile accurately, fitting λ_G, $X_{\max}$ and $N_{\max}$ to the Greisen parameterization in the same way as we did for the Gaisser-Hillas parameterization. This yields nearly identical results for each individual reconstruction: the average normalised residual of the Greisen fits is $(\chi/N_{\max})^2 = 1.1 \cdot 10^{-4}$, slightly worse than the Gaisser-Hillas fit. It is hardly surprising that these values are nearly the same, as both functional representations are essentially identical (see appendix). The average values of the reconstructed parameters are

$$\begin{aligned} \lambda_G &= 45 \pm 7\,\mathrm{g/cm^2}, \\ X_{\max} &= 6.4 \pm 0.8 \cdot 10^2\,\mathrm{g/cm^2}, \\ N_{\max} &= 6.5 \pm 0.5 \cdot 10^6. \end{aligned} \tag{2.9}$$

Note that $\lambda_H = 1.53\lambda_G$, consistent with (2.23).

From the Greisen and Gaisser-Hillas parameterizations, let us devise a different form for $N(X)$. Let us start from the Gaisser-Hillas representation, since this gives

better results, and generalise equations (2.3) and (2.6) to

$$N_L(X) = N_{\max} \exp\left[\frac{1}{\mu}\left(\ln\frac{X}{X_{\max}} - \sum_{i=1}^{n} \epsilon_i \left(1 - \frac{X}{X_{\max}}\right)^i\right)\right]. \tag{2.10}$$

We determined optimal values for ϵ_i from the average of our sample of simulations, setting $n = 6$: using higher order terms does not significantly decrease the variance reduction further. The values we obtained are given in Tab. 2.2. Also given in this table are the ϵ_i values for equations (2.3) and (2.6) and, for each representation, the average variance reductions of fitting (2.10) to each individual simulated shower. Using the description presented here set a slightly better variance reduction is obtained on average than with parameterizations according to either Greisen or Gaisser-Hillas.

2.6 · CHARGE EXCESS

Air showers tend to develop a net negative charge as they evolve, for example through positrons interacting with atmospheric electrons. As this charge excess moves through the atmosphere at superluminal velocity, it gives rise to Cherenkov radiation (Askaryan, 1965). Currently, the relative role of this effect is uncertain. Looking into the charge excess may allow us to determine the relative importance of the effect compared to that of coherent synchrotron emission (Huege & Falcke, 2003), which is thought to be dominant.

The charge excess q of electrons over photons as a function of shower depth X is defined as

$$q(X) = \frac{N_{e^-}(X) - N_{e^+}(X)}{N_{e^-}(X) + N_{e^+}(X)}. \tag{2.11}$$

For each architecture, $q(X)$ is plotted in Fig. 2.5. The relative amount of excess charge increases as the shower penetrates deeper into the atmosphere. The fit of the simulated values of q was made by two exponential functions, rising towards an asymptote:

$$q(X) = q_0 - q_1 e^{-X/X_1} - q_2 e^{-X/X_2} \tag{2.12}$$

where

$$q_0 = 0.322 \pm 0.005 \tag{2.13}$$

$$q_1 = 0.182 \pm 0.002 \qquad X_1 = 710 \pm 50\ \mathrm{g/cm^2} \tag{2.14}$$

$$q_2 = 0.09 \pm 0.01 \qquad X_2 = 36 \pm 8\ \mathrm{g/cm^2}. \tag{2.15}$$

This fit represents the simulated charge excess very well, as Fig. 2.5 shows. The value of q_0, the asymptote level, is influenced heavily by the energy threshold value below which electrons and postitrons are discarded from the simulation (Zas et al., 1992). In our simulations, this value was fixed at 0.4 MeV. Simulations with lower threshold result in more accurate particle distributions, but take a much longer time to run. The value of 0.4 MeV was chosen as a tradeoff value. At any rate, using a lower value is not

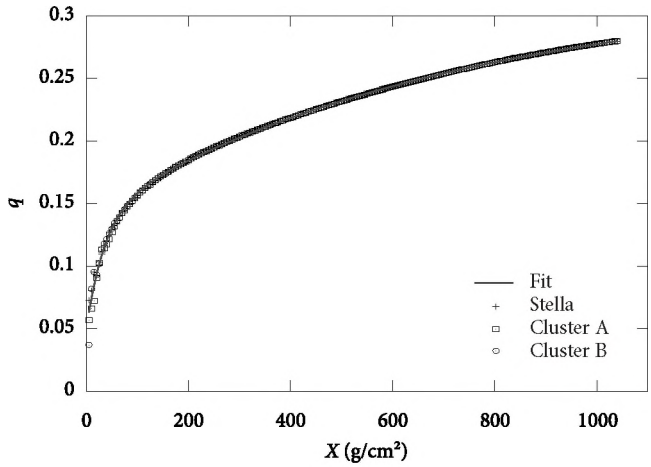

FIG. 2.5 · The charge excess q as a function of shower depth X. The points represent simulation result, the overplotted line is an empirical fit.

expected to contribute significantly to geosynchrotron radiation signal (Huege et al., 2007).

Fig. 2.6 shows the relative average charge excess q as a function of X and r. Though this relative excess is highest at distances around 500 m from the shower axis, the absolute charge excess has much the same structure as the overall spatial structure of the air shower, so that the largest absolute charge excess values are found near the shower core. Furthermore it should be noted that, because the particle distributions are averaged over the azimuthal angle, any local excess due to charge separation from deflection in the Earth's magnetic field is cancelled out. At this moment, the question whether the local charge excess due to this separation effect plays a larger role than the overall excess charge in the air shower is still open, as the average separation of positron-electron pairs is expected to be in the meter range. Such a separation could easily be recovered to a reasonable degree of accuracy at a later stage, however, since it is a systematic effect which, for a given field strength, depends solely on the average particle energy and the local atmospheric density.

2.7 · CONCLUSION

We have produced a semi-parallelized adaptation of the CORSIKA code, which is able to perform large numbers of different shower simulations simultaneously on MPI enabled computers, removing the need for external scripts to distribute showers. The code runs on large supercomputers as well as off-the-shelf desktop PCs.

Our extension of the CORSIKA code delivers reliable simulation results, iden-

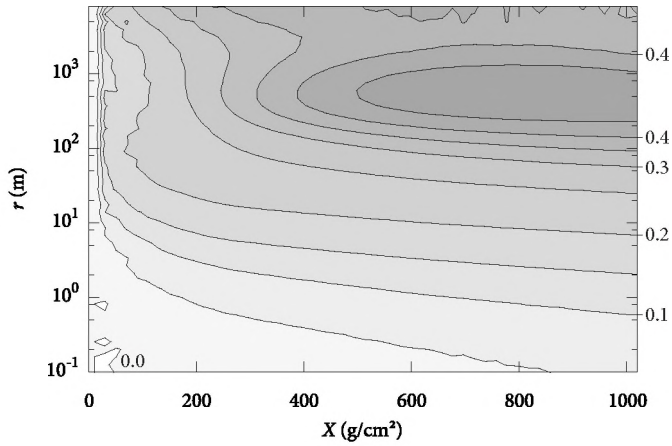

FIG. 2.6 · Two-dimensional structure of the average charge excess ratio q, as a function of atmospheric depth X and distance form the shower axis r. The color scale and black contour lines represent fractional charge excess value. Contour lines are spaced at intervals of 0.05.

tical to those of conventional CORSIKA runs and it has proven to run stably on a variety of architectures, including BlueGene/L and x86 machines. We have argued that simulation results on Stella, a BlueGene/L supercomputer accepting only MPI executables, are compatible with those of standard CORSIKA results.

We conclude that we can use our adapted CORSIKA version both for traditional shower simulations and for further analysis with REAS (Huege et al., 2007), a code which can be run on top of the CORSIKA output to simulate the radio emission profile from the particle distributions. We will use the code on Stella to produce air shower simulations in support of the LOFAR telescope, which will look at radio signatures from extensive air showers.

Using a test sample of 3000 showers at $E = 10^{16}$ eV, we have produced a modified Gaisser-Hillas parameterization, which yields an improvement in variance reduction of 10 % when fitted.

Consecutively, simulations were run on the Stella supercomputer, and the database has been expanded with air showers from protons, iron nuclei and photons from a variety of zenith angles ($\cos\theta = 1, 0.9, \ldots, 0.5$), over a wide range of energies ($\log(E/\mathrm{eV}) = 16, 16.5, \ldots, 20.5$). This database, the LOFAR Air Shower Front Evolution Library, is now publicly available, along with the source code of our CORSIKA adaptation.

Analysis of the library, both in terms of particle distributions of the extensive

TAB. 2.6 · The number of shower simulations per primary particle energy. Every run in this table is repeated six times, for azimuth angles of cos 1.0, cos 0.9, . . . , cos 0.5. The total number of runs is therefore 26322.

$\log E/\mathrm{eV}$	Number of runs			Total
	γ	p	Fe	
16.0	100	190	40	330
16.5	100	190	40	330
17.0	100	190	40	330
17.5	156	190	40	386
18.0	225	190	40	455
18.5	325	190	40	555
19.0	450	190	40	680
19.5	450	190	40	680
20.0	56	190	40	286
20.5	125	190	40	355
Total	2087	1900	400	4387

air showers and the radio signals that arise from these showers, is done separately. Our findings will be summarised in a parameterization of the radio pulses produced by the showers, as a function of the parameters involved.

ACKNOWLEDGEMENTS

We thank Dr. Dieter Heck for help with the CORSIKA code and many useful hints and discussions. We also thank Kjeld van der Schaaf and Hopko Meijering for support at Stella.

2.A · LONGITUDINAL PARAMETERIZATIONS

For a comparison of the Gaisser-Hillas and Greisen representations of the longitudinal development of air showers, let us generalise (2.6):

$$N_G(X) = N_{\max} \exp\left(\frac{1}{\mu}\Phi(X)\right) \tag{2.16}$$

where we have introduced $\mu = \lambda_G/X_{\max}$ and we have constructed $\Phi(X)$ in such a way that $\Phi(X_{\max}) = 0$:

$$\Phi(X) = \left(\frac{X}{X_{\max}} - 1\right) - \frac{3}{2}\frac{X}{X_{\max}} \ln\left(\frac{3X}{X + 2X_{\max}}\right). \tag{2.17}$$

Similarly, (2.3) can be rewritten as

$$N_H(X) = N_{\max} \exp\left(\frac{1}{\nu}\Psi(X)\right), \tag{2.18}$$

where $\nu = \lambda_H / X_{\max}$ and

$$\Psi(X) = \ln \frac{X}{X_{\max}} - \left(\frac{X}{X_{\max}} - 1 \right). \tag{2.19}$$

Since we know from Monte Carlo simulations that both representations are able to reproduce a given shower distribution to a reasonable degree, and that $N_{\max}$ and $X_{\max}$ are model independent parameters, we must assume that

$$N_G(X) \simeq N_H(X) \quad \Rightarrow \quad \frac{1}{\mu} \Phi(X) \simeq \frac{1}{\nu} \Psi(X). \tag{2.20}$$

Let us compare the Taylor expansions of the two functions $\Phi(X)$ and $\Psi(X)$ for X around $X_{\max}$. We note that the terms for order zero and one are zero in both cases:

$$\Phi(X) = -\frac{1}{3} \left(\frac{X}{X_{\max}} - 1 \right)^2 + \frac{5}{27} \left(\frac{X}{X_{\max}} - 1 \right)^3 + O(X^4), \tag{2.21}$$

$$\Psi(X) = -\frac{1}{2} \left(\frac{X}{X_{\max}} - 1 \right)^2 + \frac{1}{3} \left(\frac{X}{X_{\max}} - 1 \right)^3 + O(X^4). \tag{2.22}$$

For (2.20) to hold, we conclude that the second order terms of the equations above must be nearly the same. In other words,

$$\nu \simeq \frac{3}{2} \mu, \qquad \text{or} \qquad \lambda_H \simeq \frac{3}{2} \lambda_G. \tag{2.23}$$

2.B · EFFECT OF FLAWED ENERGY DISTRIBUTIONS

As noted in section 2.4 on page 22, there is an unphysical property in the electron and positron distribution at $\epsilon \approx 1.1$ MeV. This feature is the result of a bug in the Coast software which was, unfortunately, solved only after completion of the CORSIKA library. Its origin lies in the communication between CORSIKA and Coast.

In CORSIKA, a particle's trajectory is sampled in many steps to account for possible interactions and energy losses. When in one of these steps the particle is to be registered into the Coast histograms, ionization energy losses since the last sampling point are neglected in the faulty version of the code. In the final histogram, particles then end up being registered at a higher energy.

The specific energy being lost depends on the track length of the particle since the last interaction point. This track length in turn depends on the particle energy. At the maximum track length CORSIKA uses, the forgotten ionization loss is less than 0.01 for $\epsilon \gtrsim 30$ MeV. The relative error peaks at around 1.41 MeV, below which the CORSIKA track length decreases rapidly. At this point, the error is ~ 0.1, producing a noticeable bump in the overall energy spectrum.

The geosynchrotron radiation process is quite inefficient at these low energies, however, and the differences between radio pulses simulated with faulty and correct energy distributions is no more than 5 %, and only a few percent on average.

3 · *Universality of electron and positron distributions in extensive air showers*

S. Lafebre, R. Engel, H. Falcke, J. Hörandel, T. Huege, J. Kuijpers, R. Ulrich
This chapter is submitted to Astroparticle Physics

Using a large set of simulated extensive air showers, we investigate universality features of electron and positron distributions in very-high-energy cosmic-ray air showers. Most particle distributions depend only on the depth of the shower maximum and the number of particles in the cascade at this depth. We provide multi-dimensional parameterizations for the electron-positron distributions in terms of particle energy, vertical and horizontal momentum angle, lateral distance, and time distribution of the shower front. These parameterizations can be used to obtain realistic electron-positron distributions in extensive air showers for data analysis and simulations of Cherenkov radiation, fluorescence signal, and radio emission.

3.1 · INTRODUCTION

One of the greatest mysteries in particle astrophysics is the nature and origin of the highest-energy cosmic rays above 10^{17} eV. The study of extensive air showers produced in our atmosphere by these particles is the primary means of obtaining information about high-energy cosmic rays. Many techniques to observe these air showers, including the detection of atmospheric fluorescence and Cherenkov light (Baltrusaitis et al., 1985) and radio signal emission (Falcke et al., 2005), depend on the knowledge of the distribution of charged particles in air showers. Primarily, the distributions of electrons and positrons as most abundant charged particles are of importance. Theoretical predictions of the main production and energy loss processes in electromagnetic showers have been available for a long time (Rossi & Greisen, 1941; Nishimura, 1965). Modern Monte Carlo techniques greatly enhance the accuracy of these estimates and allow us to calculate the electron-positron distributions not only in electromagnetic showers but also showers initiated by hadrons.

In this work, we use simulations to investigate electron-positron distributions in extensive air showers and their dependence on energy, species, and zenith angle of the primary particle and on the evolution stage of the shower. Previous studies have shown that many distributions depend only on two parameters: the number of particles in the extensive air shower and the longitudinal position in the shower evolution where this maximum occurs (Hillas, 1982; Giller et al., 2005a,b; Góra et al., 2006; Chou & et al., 2005; Nerling et al., 2006; Billoir et al., 2007; Schmidt et al., 2008). This concept, which is referred to as *universality*, allows us to develop parameterizations of the electron-positron distributions as a function of relevant quantities such as energy, lateral distance, and momentum angles, in terms of only a few parameters.

3.2 · METHOD

Electron and positron distributions in the atmosphere were studied through detailed Monte Carlo simulations. Unless specified otherwise, extensive air shower simulations were performed according to the specifications below.

All simulations were carried out using the CORSIKA code, version 6.5 (Heck et al., 1998). We used the QGSJET-II-03 model (Ostapchenko, 2006a,b) to describe high-

energy interactions and the URQMD 1.3.1 code (Bass et al., 1998; Bleicher et al., 1999) at lower energies. Electromagnetic interactions were treated by the EGS4 code (Nelson et al., 1985). We applied a low energy cutoff of 151 keV and level 10^{-6} optimum thinning (Pierre Auger Collaboration & Kobal, 2001; Risse et al., 2001). The U.S. Standard Atmosphere (National Aeronautics and Space Administration (NASA), 1976; Knapp & Heck, 1993) was used as atmospheric model. It should be noted that, because simulations for our analysis were performed using only a single nuclear interaction model, the shape of the distributions presented may change somewhat when different models such as SIBYLL or QGSJET-I are employed. On the other hand, the $e^{\pm}$ distributions in proton and iron showers exhibit very good universality. Hence, the overall behaviour of the distributions should not change significantly.

The standard output of CORSIKA is a list of momenta, position coordinates, and arrival times of those particles that cross a horizontal plane representing the ground detector. This output format is not ideally suited for universality studies. First of all, particle distributions need to be calculated at many depth layers for each individual shower. Secondly, considering inclined showers, different core distances in the horizontal detector plane correspond to different shower development stages.

A multi-purpose interface called *COAST* (Corsika Data Access Tools) has been developed for accessing the data of individual particles tracked in CORSIKA (Ulrich, 2007). For each track segment of a particle simulated in CORSIKA, a COAST interface function is called with the particle properties at the start and end of the propagation step. In addition, all standard CORSIKA output information is passed to the COAST interface. This allows one to directly access the overall information of the simulated showers (e.g. energy, direction of incidence, depth of first interaction) as well as details on all individual track segments of the simulated shower particles.

The COAST interface was used in this work to produce histograms of different particle distributions. Planes perpendicular to the shower axis were defined and particles were filled in the corresponding histograms if their track traversed one of these planes. The energy, momentum, time, and position of a particle crossing one of the planes was calculated by interpolation from the start and end points of the track segment. In total, 50 planes at equidistant levels in slant depth X between the point of first interaction and sea level ($X \simeq 1036\,\mathrm{g/cm^2}$ for vertical showers) were used for histogramming, whereas the depth of a plane was measured along the shower axis. Note that these planes are, in general, not horizontal and cover different atmospheric densities. In our universality studies below, we will use only the densities at the intersection points of the planes with the shower axis.

At each of the 50 planes, two three-dimensional histograms were filled for electrons and positrons respectively. The first histogram contains logarithmically binned distributions of the arrival time, lateral distance from the shower axis, and the kinetic energy of the particles. The second histogram contains the angle between the momentum vector and the shower axis, the angle of the momentum vector projected into the plane

with respect to the outward direction in the plane, and the kinetic energy of the particles.

Showers were simulated for protons, photons, and iron nuclei at primary energies of 10^{17}, 10^{18}, and 10^{19} eV. For each combination of primary particle and energy, showers with zenith angles of 0, 30, 45, and 60° were calculated. Non-vertical showers were injected from the north, northeast, east, southeast, and south to accommodate deviations due to the geomagnetic field. Each parameter set was repeated 20 times, amounting to a total of 2880 simulated showers. The showers were produced with a parallelized CORSIKA version (Lafebre et al., 2007) on a cluster of 24 nodes. Access to this library may be obtained through the authors.

As a reference set, averaged distributions at the shower maxima of 20 vertical air showers initiated by 10^{18} eV protons are used. This set is compared to averaged distributions of other parameters, only one of which is changed at a time. If not explicitly stated, all distributions in this work refer to the sum of electrons and positrons. In particular, when the term 'particles' is used, the sum of electrons and positrons is meant.

3.3 · LONGITUDINAL DESCRIPTION

There are several ways to describe the longitudinal evolution of an air shower.

Slant depth X measures the amount of matter an air shower has traversed in the atmosphere, in g/cm^2.

Relative evolution stage is defined here in terms of the depth relative to the slant depth $X_{\max}$, where the number of particles in the air shower reaches its maximum

$$t \equiv \frac{X - X_{\max}}{X_0}, \tag{3.1}$$

with $X_0 \simeq 36.7\,\mathrm{g/cm^2}$ being the radiation length of electrons in air. Because the shower maximum always lies at $t = 0$, describing multiple showers in terms of this quantity rather than X is expected to lead to a higher degree of universality.

Shower age is defined here so that $s = 0$ at the top of the atmosphere, $s = 1$ at the shower maximum, and $s = 3$ at infinite depth

$$s \equiv \frac{3X}{X + 2X_{\max}} = \frac{t + X_{\max}/X_0}{t/3 + X_{\max}/X_0}. \tag{3.2}$$

The concept of shower age arises naturally from cascade theory in purely electromagnetic showers (Rossi & Greisen, 1941). For example, the electron energy distribution is a function of shower age. Eq. (3.2) is, however, only a simple, frequently used phenomenological approximation to the shower age parameter defined in cascade theory. It has the advantage that it can also be applied to showers with a significant hadronic component. Alternatively, shower age could be defined phenomenologically such that $s = 0$ corresponds to the depth of the first interaction. Since there is no practical way of observing the depth of the first interaction in air shower measurements this variant is not considered in our analysis.

To determine which description yields highest degree of universality, electron energy distributions of a sample of 180 showers of various primary energies and initiated by different primaries were compared. Statistical deviations from the average distribution were obtained at fixed relative evolution stages t and at each individual shower's corresponding value of X and s according to (3.1) and (3.2).

As an example of this comparison we show in Fig. 3.1 the statistical deviation from the mean energy distribution at each level. Plots are drawn as a function of t and their corresponding values in X and s. For descriptions in t and s, universality is highest near the shower maximum, because at that point all showers are at the same evolutionary stage by definition. This does not apply to the description in slant depth, where the shower maxima are not lined up. In this case, the relatively fast evolution for younger showers is reflected in falling deviations with depth. When the deviation is plotted for other physical quantities such as momentum angle or lateral distance, all curves behave in a similar manner as in Fig. 3.1.

Showers described in terms of X are less universal than those described in s or t, and slant depth is therefore rejected as parameter of choice. Between the two remaining descriptions, the difference is much smaller. Universality is slightly better for descriptions in evolution stage t for $t > -8$, though the difference is insignificant. For very young showers s is a better description, but this stage is not of interest observationally because the number of particles is so small. Comparing longitudinal shower size profiles, if showers are compared at the same evolution stage t, better universality is found than when shower age s is used (Müller, 2008). Therefore, we describe electron and positron distributions in terms of relative evolution stage t in this work.

The total number of particles in the air shower crossing a plane at level t perpendicular to the primary's trajectory is $N(t)$. We define

$$N(t;\mu) \equiv \frac{\partial N(t)}{\partial \mu} \quad \text{and} \quad n(t;\mu) \equiv \frac{1}{N(t)} \frac{\partial N(t)}{\partial \mu} \tag{3.3}$$

as, respectively, the total and the normalised differential number of particles with respect to some variable μ. Likewise, distributions as a function of two variables μ and ν are defined as

$$N(t;\mu,\nu) \equiv \frac{\partial^2 N(t)}{\partial \mu\, \partial \nu} \quad \text{and} \quad n(t;\mu,\nu) \equiv \frac{1}{N(t;\mu)} \frac{\partial^2 N(t)}{\partial \mu\, \partial \nu}, \tag{3.4}$$

with dimension $[\mu\nu]^{-1}$ and $[\nu]^{-1}$, respectively. Note that the definition of $n(t;\mu,\nu)$ implies that the distribution is normalised by integrating only over the last variable:

$$\int_{\nu_{\min}}^{\nu_{\max}} n(t;\mu,\nu)\, \mathrm{d}\nu = 1, \tag{3.5}$$

making the normalisation independent of μ. In this expression, $\nu_{\min}$ and $\nu_{\max}$ are the minimum and maximum values up to which the histograms are calculated.

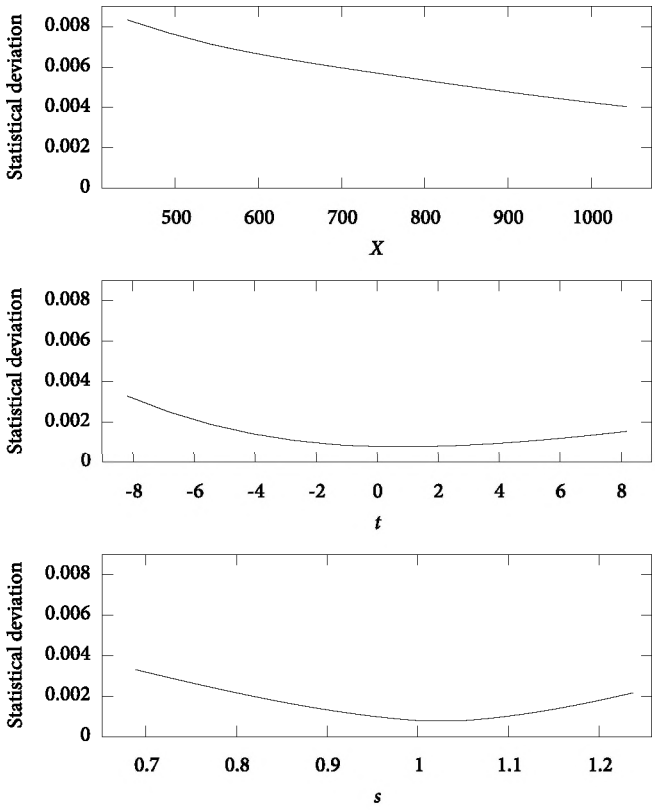

FIG. 3.1 · Average statistical deviation from the average energy distribution for 180 air showers of different energy and primary species, averaged in slant depth (top), relative evolution stage (middle), and age (bottom). On average, the longitudinal range is the same in each plot.

The distributions $n(t;\mu,\nu)$ presented in the following sections may be used to obtain realistic energy-dependent particle densities for an air shower, if the values of $X_{\max}$ and $N_{\max}$ are given. One needs only to calculate the total number of particles $N(t)$ at the desired shower evolution stage. An estimate of $N(t)$ can be obtained directly from shower profile measurements or through one of the many parameterizations available (Greisen, 1960; Gaisser & Hillas, 1978; Abu-Zayyad et al., 2001; Pryke, 2001).

3.4 · ENERGY SPECTRUM

From cascade theory, the energy spectrum of electrons and positrons as a function of shower age takes an analytical form as derived by Rossi & Greisen (1941); a thorough previous study of this parameterization was done by Nerling et al. (2006). Loosely translating this description in terms of t, we replace the equation by

$$n(t;\ln\epsilon) = \frac{A_0\epsilon^{\gamma_1}}{(\epsilon+\epsilon_1)^{\gamma_1}(\epsilon+\epsilon_2)^{\gamma_2}}, \tag{3.6}$$

where ϵ is the energy of a given secondary particle in the shower, and $\epsilon_{1,2}$ depend on t. We have performed a fit to this function for electrons, positrons and their sum, indirectly providing a description of the negative charge excess of extensive air showers as a function of evolution stage and secondary energy. In these fits the exponent γ_1 was fixed at $\gamma_1 = 2$ for positrons and $\gamma_1 = 1$ for both electrons and the total number of particles. The parameters for all three cases are explained in Appendix 3.A.

When applied to CORSIKA showers initiated by different species at different energies, the energy distribution (3.6) is reconstructed accurately. This is shown in Fig. 3.2, where the simulated energy distributions are compared to their parameterizations for evolution stages $t = -6, 0, 6$. For shower stages $-6 < t < 9$, in the energy region 1 MeV $< \epsilon <$ 1 GeV, which is most relevant for observation of geosynchrotron or Cherenkov radiation, deviations are generally smaller than 10 % and never exceed 25 % for all three parameterizations. For very young showers (Fig. 3.2, top panel), increasing deviations are mainly caused by variations in primary energy, not by primary species type. Therefore, it highlights a diminished accuracy to universally describe showers at $t < -6$ rather than hadronic model-dependence.

Using (3.6), a similar level of universality of the energy distribution of electrons and positrons is reached as previously obtained with a description in s (Nerling et al., 2006). This basic observation is an important one, as it allows us to study other physical quantities in dependence of the electron energy in the remainder of this work.

3.5 · ANGULAR SPECTRUM

The angular distribution of particles is an important factor for observations with Cherenkov and radio telescopes. For successful radio detection an antenna needs to be placed close to the shower impact position, because geosynchrotron radiation is beamed in

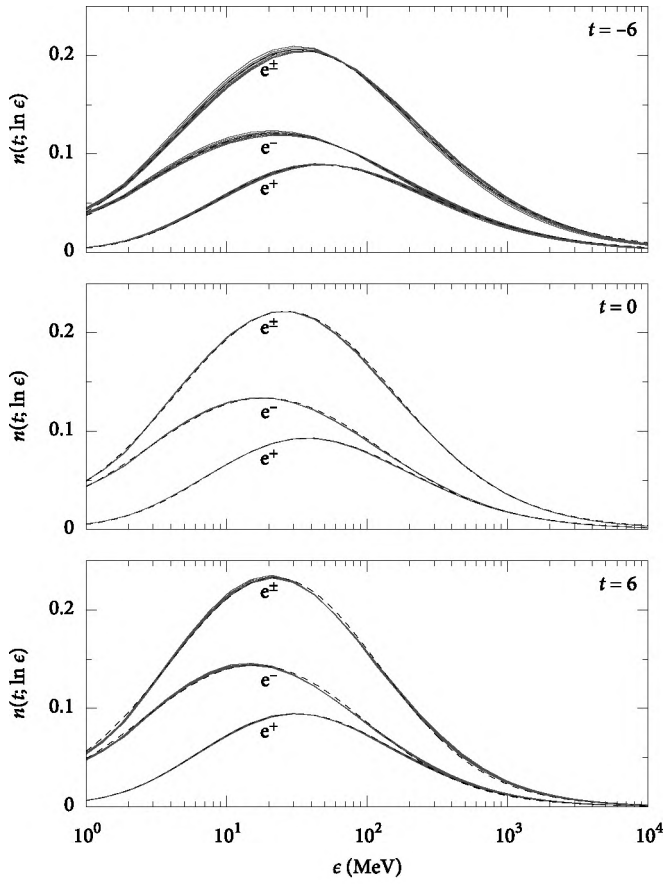

FIG. 3.2 · Average energy distribution for different evolution stages $t = -6, 0, 6$ for electrons (marked e^-), positrons (e^+), and their sum ($e^\pm$). Background curves represent simulated distributions for different primaries (p, Fe, and γ) and energies (10^{17}, 10^{18} and 10^{19} eV). The corresponding parameterized distributions from (3.6) are plotted on top (dashed).

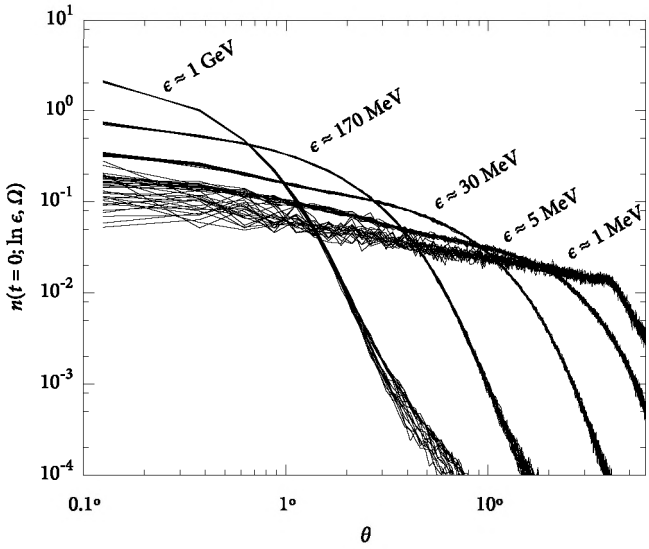

FIG. 3.3 · Electron distributions $n(t = 0; \ln \epsilon, \Omega)$ at different electron energies as a function of momentum angle to the shower axis for 20 individual showers initiated by 10^{18} eV protons. 0° is along the primary's trajectory, 90° is perpendicular to the shower axis.

a very narrow cone in the direction of propagation (Huege & Falcke, 2003). As far as the particle distributions are concerned, the size of the patch that is illuminated on the ground then depends on the lateral distribution of the particles (cf. Sect. 3.7) and the angle with respect to the shower axis at which they propagate. Likewise, for Cherenkov observations the angle at which photons are emitted is a convolution of the density-dependent Cherenkov angle, which is of the order of $\sim 2°$, and the angular distribution of the particles that emit them.

Fig. 3.3 shows the angular distribution of particles as simulated in 20 individual vertical proton showers at 10^{18} eV as a function of θ. To compensate for the increase in solid angle with rising θ, the distribution of vertical momentum angles plotted here is defined in terms of Ω as

$$n(t; \ln \epsilon, \Omega) = \frac{n(t; \ln \epsilon, \theta)}{\sin \theta}. \tag{3.7}$$

Since the majority of all electrons and positrons stays close to the shower axis, we focus on this part of the distribution. We will ignore the more horizontal part further away from the axis that can be seen at the right end of the curve for 1 GeV in Fig. 3.3. When θ is plotted on a logarithmic scale, it becomes clear that there is a plateau close to the shower axis at all energies and a sharp drop at a certain angle that depends on secondary energy.

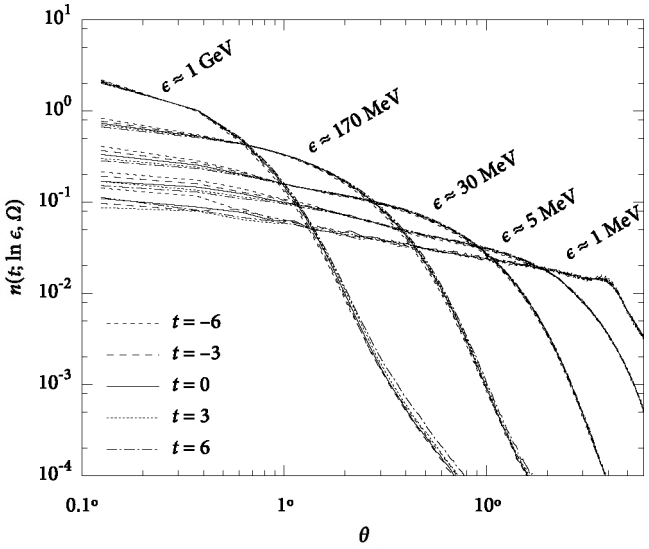

FIG. 3.4 · Normalised average distributions $n(t; \ln \epsilon, \Omega)$ for different shower stages, averaged over 20 proton-initiated showers at 10^{18} eV.

Fig. 3.4 extends the angular distributions to different shower stages. The differences in the distributions are clearly smaller than the differences between individual showers, as noted earlier (Nerling et al., 2006; Giller et al., 2005a,b). The differential electron distribution with regard to the direction of the particle's momentum is therefore independent of shower stage. In addition, no perceptible dependence on incidence zenith angle or primary energy was found. When looking at different primary species, universality seems somewhat less convincing: spectra for heavier primary species tend to be wider at higher electron energies. The effect is too small, however, to be of consequence in our analysis.

The universality with respect to t allows us to parameterize this distribution as a function of two physical quantities only: momentum angle and energy. We propose the form

$$n(t; \ln \epsilon, \Omega) = C_0 \left[\left(e^{b_1} \theta^{\alpha_1} \right)^{-1/\sigma} + \left(e^{b_2} \theta^{\alpha_2} \right)^{-1/\sigma} \right]^{-\sigma}, \tag{3.8}$$

to describe the distribution. Values for α_i and b_i, which envelop the dependence on ϵ, are chosen such that the first term describes the flatter portion of the angular distribution parallel to the shower axis and the second represents the steep drop. The value of σ determines the smoothness of the transition from the flat region to the steep region. Best fit values for σ, b_i, and α_i are given in Appendix 3.A. The dependence of these parameters

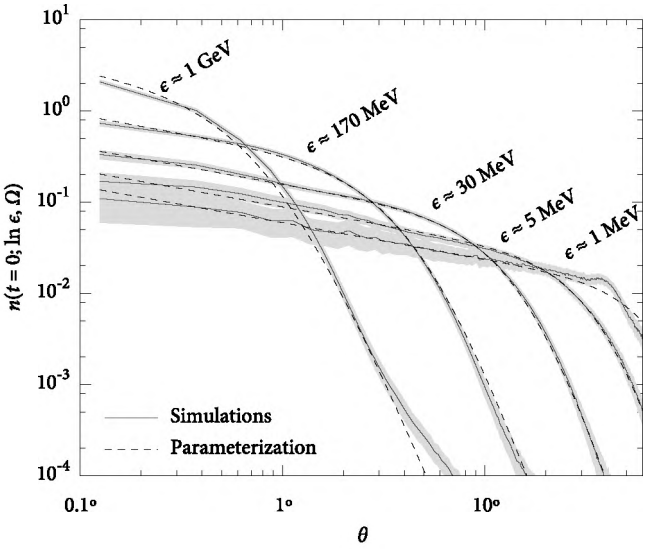

FIG. 3.5 · Normalised average electron distributions $n(t = 0; \ln \epsilon, \Omega)$ (solid) for 20 proton showers at 10^{18} eV with 3σ statistical error margins (filled area). For each energy, corresponding parameterizations according to (3.8) are also drawn (dashed).

on the secondary energy ϵ was determined purely empirically. For several energies, the parameterized forms are plotted along with their associated simulated distributions in Fig. 3.5, showing good correspondence between the two. The parameterization provides a good description of the simulated distribution for the energy region 1 MeV $< \epsilon <$ 10 GeV and $\theta < 60°$.

We now define the cutoff angle θ_c as one half of the angle at which $e^{b_1} \theta^{\alpha_1} = e^{b_2} \theta^{\alpha_2}$:

$$\theta_c(\epsilon) = \frac{1}{2} \exp\left[-\frac{b_1 - b_2}{\alpha_1 - \alpha_2} \right]. \tag{3.9}$$

For high energies, where the momentum angle is smaller than 90° for the majority of particles, θ_c is a measure for the root mean square value θ_{RMS} of the particle momentum angles. This is outlined in Fig. 3.6, in which θ_c is plotted as a function of energy. Theoretical root mean square scattering angles according to Rossi & Greisen (1941) in high and low secondary energy limits are also drawn, as well as empirical models as parameterized in Hillas (1982) and Giller et al. (2005a). At high energies, the theoretical average scattering angle is expected $\propto \epsilon^{-1}$, while at low energies it is $\propto \epsilon^{-1/2}$. This behaviour is reproduced properly for the cutoff angle. For low secondary energies ($\epsilon \lesssim 3$ MeV), the definition of a cutoff or root mean square angle becomes inapplicable as the angular

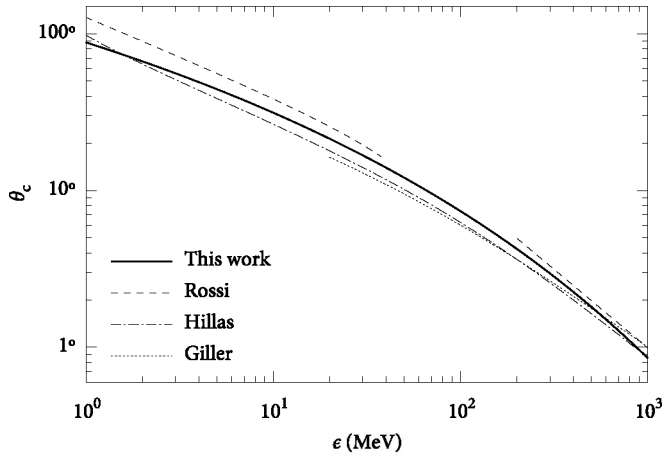

FIG. 3.6 · Cutoff angle θ_c according to (3.9) for the angular distribution as a function of secondary energy (solid line). Also shown are theoretical predictions for θ_{RMS} from Rossi & Greisen (1941) (dashed) as well as empirical relations from Hillas (1982) (dash-dotted) and Giller et al. (2005a) (dotted).

distribution widens, covering all angles. For $\epsilon > 2$ MeV, no appreciable difference was found between the angular distributions of positrons on the one hand and electrons on the other.

Because our histograms do not have any sensitivity in the azimuthal direction by design, no dependence on the geomagnetic field could be determined. Previous work has shown that the effect on the angular distribution is probably small, but not negligible (Hillas, 1982; Elbert et al., 1983). Because the accuracy of simulations has rather improved since these studies were carried out, it would be worthwhile to investigate the effect of the geomagnetic field in greater detail.

3.6 · OUTWARD MOMENTUM DISTRIBUTION

Let us define ϕ as the angle of a particle momentum vector projected in the plane perpendicular to the shower axis with respect to the outward direction, such that $\phi = 0°$ for a particle moving away from the shower axis, and $\phi = 180°$ for a particle moving towards it. We will refer to this angle as the horizontal momentum angle. The effect of fluctuations in the horizontal angular distribution is generally much less important than those in the vertical angular spectrum. In fact, the distribution of the particle's ϕ angle does not have any influence on the observed signal when the distance from the observer to the shower is much larger than the average distance from the shower particles to the shower axis, as is the case in air fluorescence observations. This is because the cylindrical

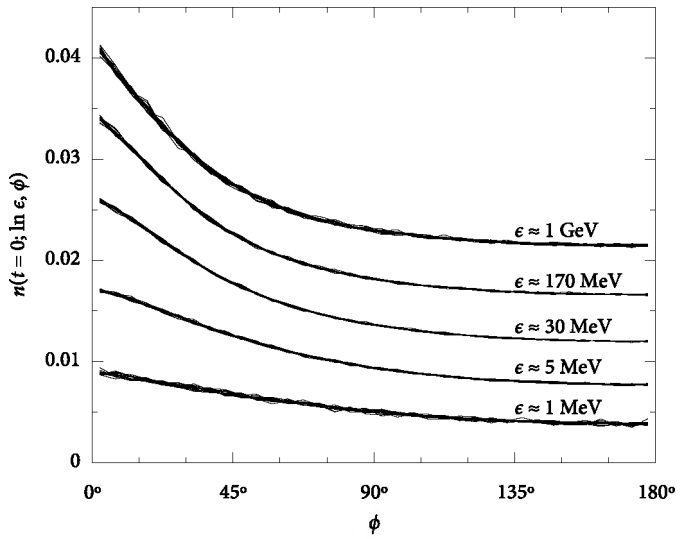

FIG. 3.7 · Normalised simulated horizontal angular electron distributions for 20 individual showers initiated by 10^{18} eV protons at different energies. Consecutive curve sets are shifted up by 0.005 to distinguish them better; curves for 1 MeV are at the actual level.

symmetries of the momentum angles and the shower geometry cancel out independently of the shape of the distribution. Geosynchrotron radiation, however, will only produce a significant signal reasonably close to the shower axis, because the shower front is thicker in length further away (cf. Sect. 3.8), breaking down coherence. Therefore, the horizontal momentum angle spectrum has to be taken into account for radio measurements.

Simulated distributions $n(t;\ln\epsilon,\phi)$ at $t = 0$ are plotted in Fig. 3.7 for the reference set. We observe that high-energy particles tend to move outward more than lower-energy particles. This can be explained by considering the collisions in which high-energy electrons and positrons are created, as they primarily occur close to the shower axis. Hence reaction products are transported away from the shower core due to their transverse momenta. Electrons and positrons with lower energies, on the other hand, are also created further away from the shower core.

No significant dependencies on incident zenith angle, primary energy, and primary species were found, so the horizontal momentum angular spectra are universal. Additionally, the shape of the distribution does not change significantly for $\epsilon > 2$ MeV when only electrons or only positrons are considered. There is some dependence in terms of t, however: the distribution appears to soften with evolution stage. This effect can be

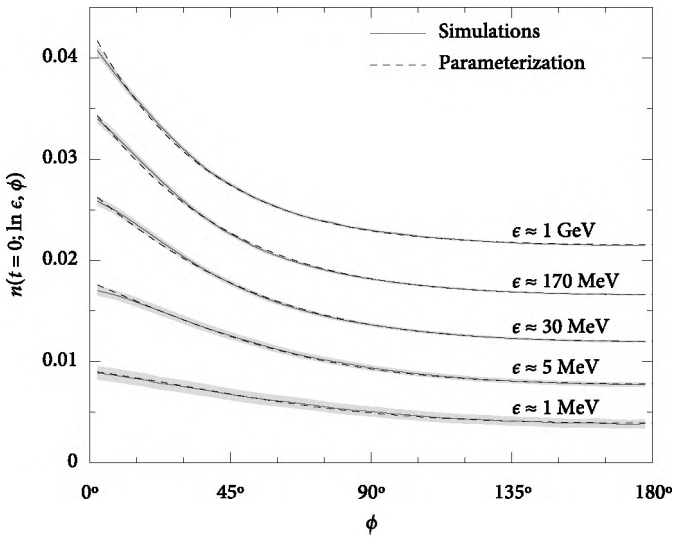

FIG. 3.8 · Normalised average electron distributions $n(t = 0; \ln \epsilon, \phi)$ (solid) for 20 proton showers at 10^{18} eV with 3σ statistical error margins (filled area). For each energy, corresponding parameterizations according to (3.10) are also drawn (dashed).

explained from the expanding spatial structure of the shower with age.

The distribution of $n(t; \phi)$ is very nearly exponential for electrons and positrons with energies over 10 GeV, while it has a slight bulge around the outward direction at lower energies. To describe the distribution, we use the parameterization

$$n(t; \ln \epsilon, \phi) = C_1[1 + \exp(\lambda_0 - \lambda_1 \phi - \lambda_2 \phi^2)], \tag{3.10}$$

a form which accurately reproduces the distribution. The resulting parameter values $\lambda_0(t, \epsilon)$, $\lambda_1(\epsilon)$, and $\lambda_2(\epsilon)$ are explained in Appendix 3.A. The reference set, drawn together with its corresponding parameterization in Fig. 3.8, shows a high level of agreement. For other shower parameters and stages, there is a similar degree of consistency.

3.7 · LATERAL DISTRIBUTION

The lateral spread of particles in an air shower is of direct relevance since it is the primary means of obtaining information about the shower in ground-based scintillator experiments measuring particle densities at different lateral distances. By integrating the measured distribution or using the particle density at a given distance, an estimate for the primary energy can be made. Exact knowledge of the lateral distribution shape is therefore crucial to accurately determine the shape of the cosmic-ray energy spectrum.

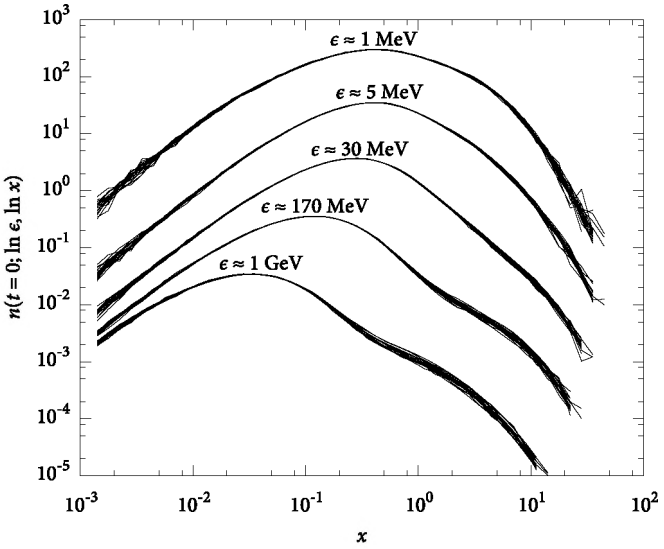

FIG. 3.9 · Electron distributions $n(t=0;\ln\epsilon,\ln x)$ for different electron energies as a function of distance to the shower axis for 20 individual showers initiated by 10^{18} eV protons. The curve set for 1 MeV is at the actual level; consecutive sets are shifted up by a factor of 10.

When looking at the lateral distribution of electron and positrons in terms of the lateral distance r from the shower axis, a very poor level of universality is encountered. This is mainly due to differences in atmospheric density at the showers' individual values of $X_{\max}$. We can compensate for these differences by expressing the lateral distance in terms of the Molière unit r_{M}, defining (Dova et al., 2003)

$$x \equiv \frac{r}{r_{\mathrm{M}}} \simeq \frac{r\rho_{\mathrm{A}}(h)}{9.6\,\mathrm{g/cm^2}}, \tag{3.11}$$

where $\rho_{\mathrm{A}}(h)$ is the atmospheric density as a function of height h. For different values of ϵ, the normalised lateral particle distribution at $t=0$ is shown in Fig. 3.9 as a function of distance for 20 individual proton showers. In this figure, all curves line up as the compensation for density is applied. Note that the physical density $N(t;r)$, expressed in particles per unit area, is proportional to $N(t;\ln x)/x^2$:

$$N(t;\ln x) = \frac{\partial N(t)}{\partial \ln x} = 2\pi x^2 r_{\mathrm{M}}^2 \frac{\mathrm{d}N(t)}{2\pi r\,\mathrm{d}r}. \tag{3.12}$$

As expected, particles with higher energies tend to remain closer to the shower axis.

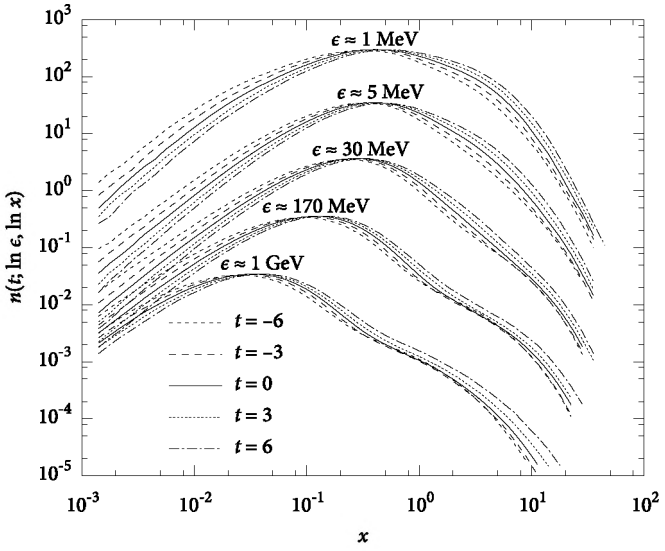

FIG. 3.10 · Average distributions $n(t; \ln \epsilon, \ln x)$ for different shower stages, averaged over 20 proton-initiated showers at 10^{18} eV, clearly showing dependence on t. Again, consecutive sets are shifted up by a factor of 10.

This agrees with the observation that the angle of their momentum to the shower axis is smaller.

There is no statistically relevant dependence of the lateral distribution on zenith angle of incidence, nor does it change when electrons or positrons are considered separately. There is, however, a significant effect with shower stage as shown in Fig. 3.10: older showers tend to be wider at the same secondary energy. Therefore, unlike in the case of angular distributions, in any parameterization of the lateral distribution a dependence on t must be incorporated. There is also a minor effect of the energy of the primary on the distribution, but this is only appreciable for secondary energies of $\epsilon > 1$ GeV.

From Figs. 3.9, 3.10, and 3.11 it is observed that each curve is a combination of two separate contributions. The left peak, the shape of which does not depend significantly on primary energy or species, is produced through the main electromagnetic formation channel of cascading steps of bremsstrahlung and pair creation. The second bulge shows a high level of dependence on primary species, as shown in Fig. 3.11. It tends to be less prominent for photon primaries, as for these species there is no significant contribution from the pion production channel. For hadronic primaries it is more significant, especially at higher secondary energies of $\epsilon > 100$ MeV. The magnitude of the variation between different species does not change with t, but its lateral position

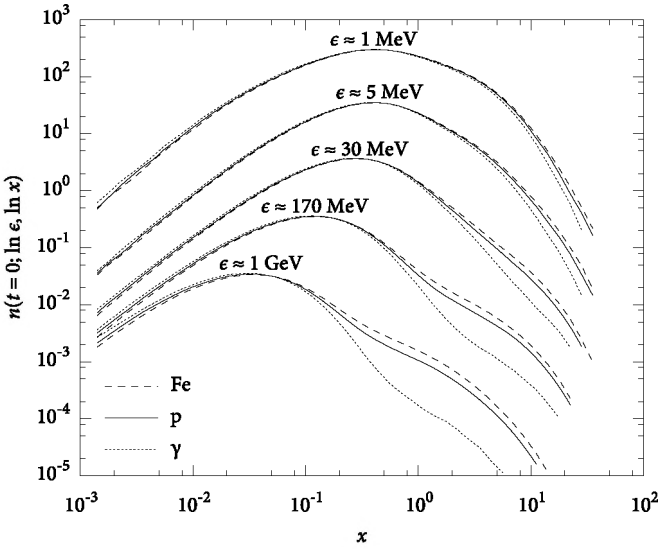

FIG. 3.11 · Average distributions $n(t = 0; \ln \epsilon, \ln x)$ for different primaries, averaged over 20 showers at 10^{18} eV. Again, consecutive sets are shifted up by a factor of 10. Note the dependence on species of the bulge on the right.

does slightly. The variations in strength of the second bulge for different primaries can be traced back to the contribution initiated by the decay channel $\pi^{\pm} \rightarrow \mu^{\pm} + \nu_{\mu}$. This is shown in Fig. 3.12, comparing a set of unaltered 10^{17} eV photon-initiated showers, which have no significant pion content, to a set of proton showers at the same energy in which the $\pi^{\pm}$ creation channel was disabled. Differences between their lateral distributions are smaller than statistical deviations.

This observation raises the question whether one could use this difference in lateral distribution to differentiate between primaries on an individual shower basis by their lateral distribution, independently of measurements of primary energy or depth of shower maximum. This would be a difficult task. First of all, appreciable divergence in density only occurs at high energies and at some distance, implying that the total electron density in the differential region would be very small. Additionally, the effect does not appear at the same distance for different electron energies. This makes the feature less pronounced when an integrated energy spectrum is measured.

Traditionally, the integral lateral electron density distribution is described by an analytical calculation of the lateral distribution in electromagnetic cascades, the Nishimura-Kamata-Greisen (NKG) function (Kamata & Nishimura, 1958; Greisen, 1965). The integral lateral distribution for our simulated set of showers $n(t; \ln x) \propto x^2 \rho_{\mathrm{NKG}}$ is

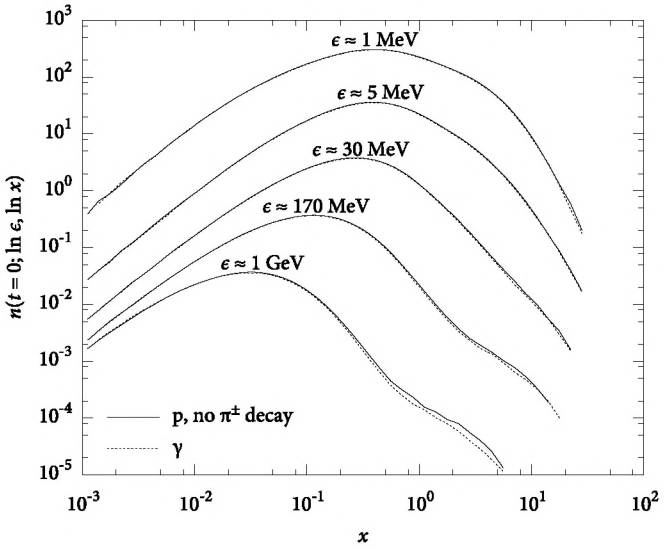

FIG. 3.12 · Comparison of average distributions $n(t = 0; \ln \epsilon, \ln x)$ at 10^{17} eV for 20 proton showers in which $\pi^{\pm}$ decay was disabled to 20 standard photon showers. Again, consecutive sets are shifted up by a factor of 10.

reproduced well by a parameterization of this form, provided that we allow the parameters to be varied somewhat. Let us define

$$n(t; \ln x) = C_2 x^{\zeta_0} (x_1 + x)^{\zeta_1}. \tag{3.13}$$

as parameterization. In the original definition, described in terms of shower age s, we have $\zeta_0 = s$, $\zeta_1 = s - 4.5$, and $x_1 = 1$. Our simulated lateral spectra closely follow the values $\zeta_0 = 0.0238t + 1.069$, $\zeta_1 = 0.0238t - 2.918$, and $x_1 = 0.430$ to an excellent level for $10^{-3} < x < 10$.

To reproduce the main bulge in the energy-dependent lateral electron distributions, we propose a slightly different function. The second bulge will be ignored here since it is much lower than the primary bulge, and its relative height depends heavily on primary species as mentioned earlier. The proposed parameterization is the same as (3.13):

$$n(t; \ln \epsilon, \ln x) = C_2' x^{\zeta_0'} (x_1' + x)^{\zeta_1'}, \tag{3.14}$$

mimicking the behaviour of the NKG function, but now also varying the parameters with ϵ. Appendix 3.A explains the values of x_i' and ζ_i'. As an example of the fit, Fig. 3.13 compares the parameterization to the average distribution for proton showers at their

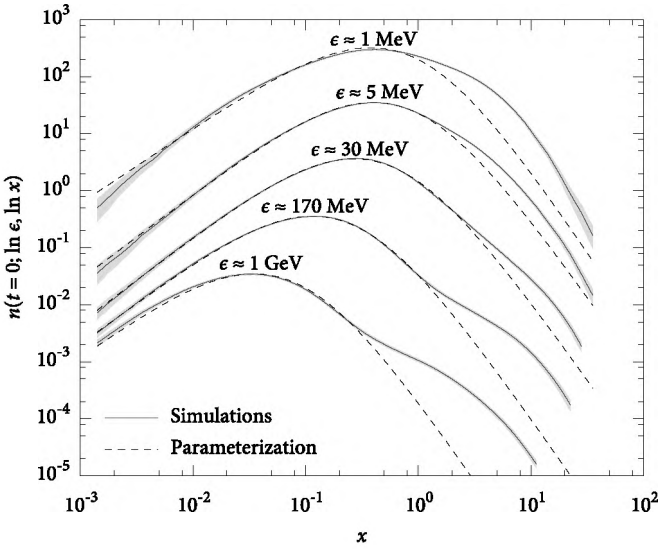

FIG. 3.13 · Normalised average electron distributions $n(t = 0; \ln \epsilon, \ln x)$ (solid) for 20 proton showers at 10^{18} eV with 3σ statistical error margins (filled area). For each energy, corresponding parameterizations according to (3.14) are also drawn (dashed). Consecutive sets are again shifted up by a factor of 10.

maximum. The proposed parameters adequately reproduce the main bulge of the lateral distribution in the energy range of 1 MeV $< \epsilon <$ 1 GeV for distances $x > 2 \cdot 10^{-3}$ and evolution stages $-6 < t < 9$.

Neglecting the second bulge results in a slightly overestimated overall value for the normalisation. The disregarded tail only constitutes a minor fraction of the total number of particles, however, especially at high energies. This fact becomes even more evident if one considers that the actual distribution is obtained by dividing by x^2.

The position of the break x_c, the distance of the highest peak in the distribution, is plotted in Fig. 3.14 for various shower stages for 20 averaged showers. The theoretical break distance from the original Nishimura-Kamata-Greisen distribution at the shower maximum, which is an integral distribution over all $e^{\pm}$ energies, is also plotted as a horizontal line. At lower energies, the two are in good agreement as expected.

3.8 · SHAPE OF THE SHOWER FRONT

For radio geosynchrotron measurements the arrival time of charged particles is a vital quantity, because it determines the thickness of the layer of particles that form the air shower. This thickness in turn defines the maximum frequency up to which the resulting

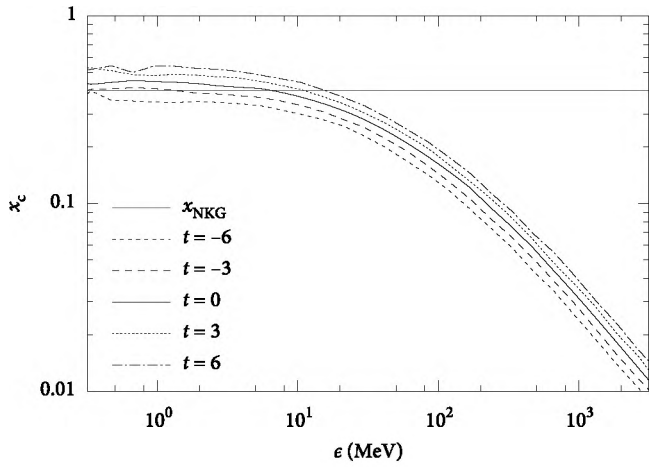

FIG. 3.14 · Cutoff distance x_c as a function of secondary energy at different shower stages. The energy-independent overall break distance obtained from the NKG function is also plotted (horizontal line).

radio signal is coherent (Huege & Falcke, 2003; Scholten et al., 2008), which influences the strength of the radio signal on the ground.

Let us define the delay time Δt of a particle as the time lag with respect to an imaginary particle continuing on the cosmic-ray primary's trajectory with the speed of light in vacuum from the first interaction point. In the distribution of these time lags we must again compensate for differences in Molière unit to obtain a universal description by introducing the variable

$$\tau \equiv \frac{c\Delta t}{r_M}, \tag{3.15}$$

where c is the speed of light in vacuum. At sea level, $\tau = 1$ corresponds to a time delay of 0.26 μs. For 20 proton shower simulations at 10^{19} eV, the shower front shape at the shower maximum is displayed in Fig. 3.15 at different distances from the shower core. The distribution shown is $n(t; \ln x, \tau)$, and each curve is scaled to a similar level for easier comparison of the distributions. Though the low number of particles leads to larger fluctuations of the distributions at high distances, the behaviour clearly does not change significantly for $x > 3$.

No significant dependence of the shower front shape on incidence angle was found for $x < 15$, nor is there any change with primary energy. There are fluctuations with evolution stage, however: the time lag decreases by a constant fraction which depends on the shower stage. As the shower evolves, the entire distribution shifts to the left. This effect, shown in Fig. 3.16, can be explained from the increasing spatial structure of the

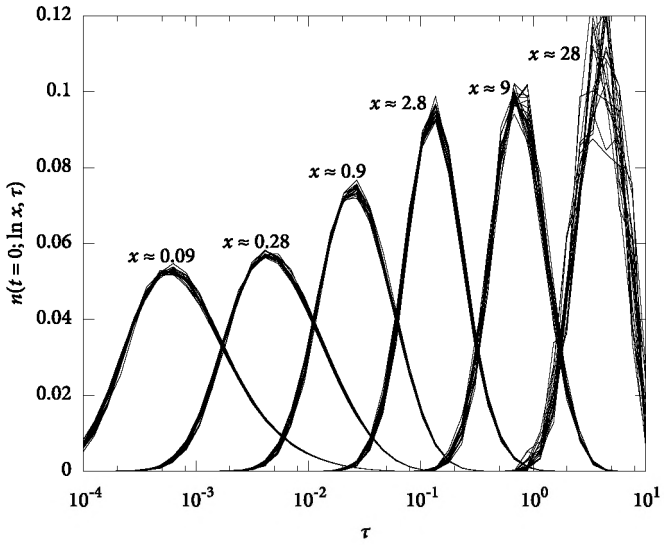

FIG. 3.15 · Electron distributions $n(t = 0; \ln x, \tau)$ as a function of particle time lag for 20 individual showers initiated by 10^{19} eV protons.

shower with age, not unlike the case of an expanding spherical shell. We shall see further on that the analogy is not entirely legitimate, but the shift does allow one to estimate $X_{\max}$ from the arrival times of the particles. We also found a non-negligible dependence of the delay time on primary species, which is comparable in nature to the effect of evolution stage, as shown in Fig. 3.17. The dependence of the distribution on both species and evolution stage can be removed almost entirely for distances of $0.03 < x < 15$ by applying a simple exponential shift in τ. Additionally, the distributions shown are integrated over energy. Therefore, the shape of the distribution changes when electrons or positrons are considered separately, since their energy distribution is different as well.

The particle distribution at a certain distance from the shower core as a function of arrival time is usually parameterized as a gamma probability density function (Woidneck & Bohm, 1975; Agnetta et al., 1997), given by

$$n(t; \ln x, \tau) \propto \exp[a_0 \ln \tau - a_1 \tau]. \tag{3.16}$$

We have found that such a parameterization does not follow our simulated distributions very well. Its slope is too gentle at short delay times and too steep at long time lags. Here, we use the better representation

$$n(t; \ln x, \tau) = C_3 \exp[a_0 \ln \tau' - a_1 \ln^2 \tau'], \tag{3.17}$$

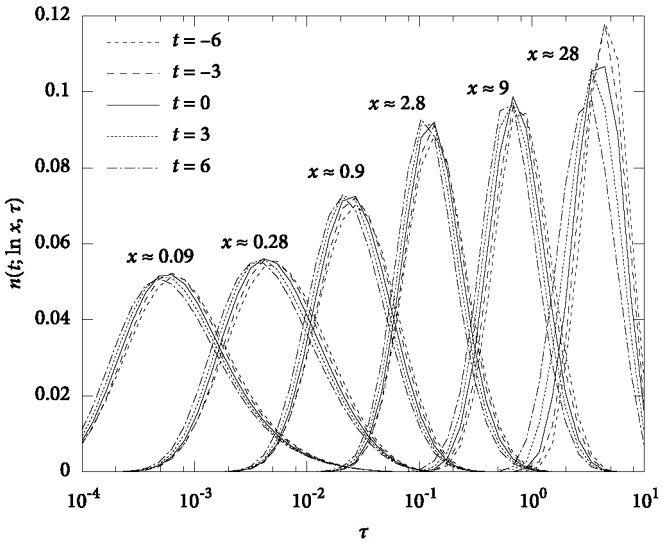

FIG. 3.16 · Average distributions $n(t; \ln x, \tau)$ for different evolution stages, averaged over 20 proton-initiated showers at 10^{19} eV.

which allows for a more gradual slope on the right side of the curve. The modified time lag τ' takes into account the exponential shift mentioned earlier, and is defined as

$$\tau' \equiv \tau e^{-\beta_t t - \beta_s}, \tag{3.18}$$

where β_t and β_s are corrections for shower evolution stage and primary species, respectively. The values of the parameters $a_0(x)$, $a_1(x)$, β_t, and β_s are explained in Appendix 3.A. The parameter β_t can be seen as a scale width for the expansion of the shower front as it develops. Note that the integral lateral distribution as parameterized in (3.13) is needed to obtain actual particle numbers via

$$N(t; \ln x, \tau) = N(t) n(t; \ln x) n(t; \ln x, \tau), \tag{3.19}$$

using the identities in (3.4).

We may exploit the necessity of the parameter β_s in our description of the shower front shape to determine the primary species if the value of X_{max} is known. To distinguish proton from photon showers in this manner, the required resolution in shower stage is $\delta t < \beta_s/\beta_t \simeq 0.52$, assuming perfect timing and distance information. This corresponds to an error in X_{max} of 19 g/cm^2. To separate proton from iron showers, the maximum error is reduced to 11 g/cm^2. Unfortunately, these figures are similar to or

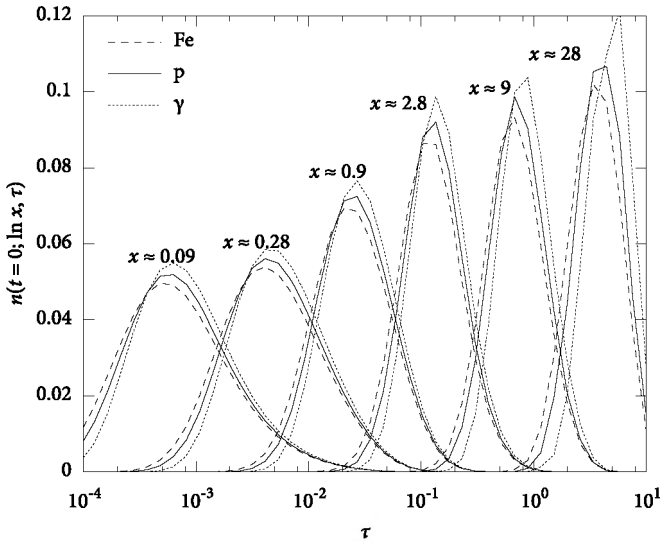

FIG. 3.17 · Average distributions $n(t = 0; \ln x, \tau)$ for different primary species, averaged over 20 proton-initiated showers at 10^{19} eV.

smaller than statistical fluctuations in individual showers or systematic uncertainties in the atmospheric density due to weather influences (Keilhauer et al., 2004; Wilczyńska et al., 2006). This makes it very difficult to take advantage of this intrinsic difference.

An example of the fit of (3.17) at $t = 0$ is shown in Fig. 3.18. For distances $x \gtrsim 0.8$, the fit describes the simulations very accurately. Equivalence is partially lost at small distances, because the shape of the distribution becomes more complicated closer to the shower core. Even there, however, the resulting shape is reasonably accurate down to $x \simeq 0.04$. Also plotted are best-fit gamma probability density functions according to (3.16) for each distance, which are of lower quality than the parameterization used here, especially close to the core.

For a certain distance from the shower core, we define the time lag τ_c as the time lag where the particle density is at its maximum, corresponding to the peaks of the curves shown earlier in this section. Its value at the shower maximum is shown in Fig. 3.19 as a function of x for the reference simulation set. The two straight lines represent fits of the form $\tau_c = Ax^k$ to the part before (dashed) and after the break (dotted) as shown in the plot. The time lag of the maximum particle density can be parameterized as

$$\tau_c = \begin{cases} (0.044 - 0.00170t)x^{1.79-0.0056t} & x < x_0; \\ (0.028 - 0.00049t)x^{1.46-0.0007t} & x > x_0, \end{cases} \tag{3.20}$$

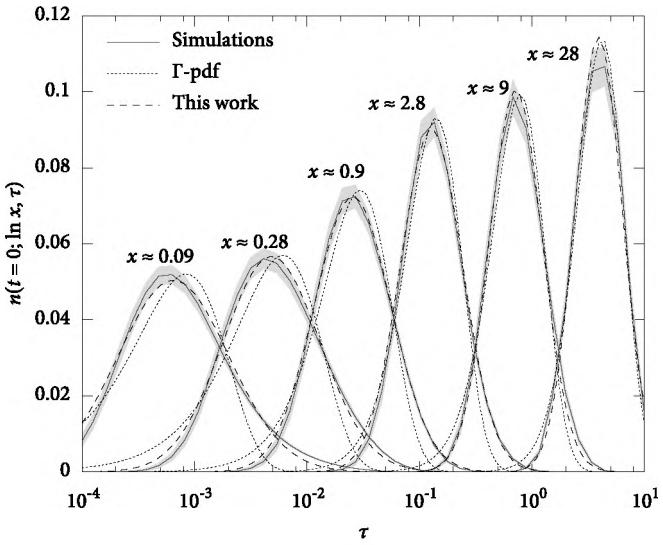

FIG. 3.18 · Average electron distributions $n(t = 0; \ln x, \tau)$ (solid) for the reference set with 3σ statistical error margins (filled area). For each distance, corresponding parameterizations according to (3.17) are drawn as well (dashed). Best-fit Γ-pdf are also plotted (dotted).

where the value for x_0 follows from continuity. One could employ this function to estimate the value of $X_{\max}$, though the accuracy attainable in this way is probably much lower than using fluorescence measurements.

In experiments, the shower front is sometimes approximated as a spherical shell (Dawson & Pryke, 1997). How do the simulated distributions compare to such a hypothetical shape? Close to the shower core, where $r \ll R$ (with $R \simeq 50$ the supposed curvature radius in Molière units) we expect $k = 2$ and $R = A^{-1}$. Going out, the slope should then decrease slowly as x approaches the presumed curvature radius.

This spherical shape does not correspond to the situation in our simulations. In the innermost region the exponent gives consistently smaller values of $k \simeq 1.79$. Further out, there is an abrupt transition around $x \simeq 0.3$, and the final exponent is $k \simeq 1.45$.

3.9 · CONCLUSION

In this work, we have presented a framework for the accurate description of electron-positron distributions in extensive air showers. To characterize the longitudinal evolution of the air shower, the concept of slant depth relative to the shower maximum is used.

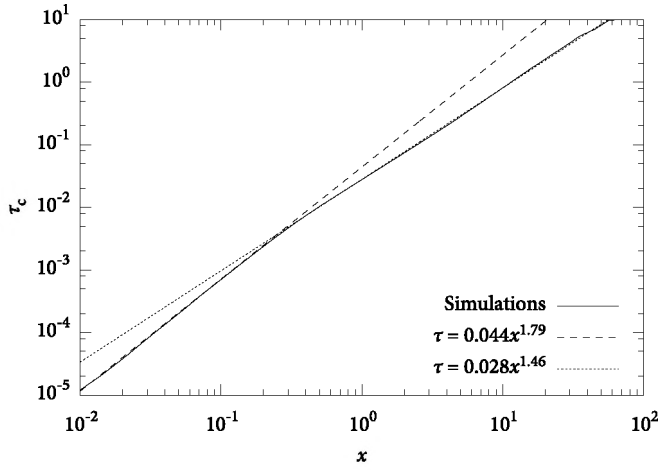

FIG. 3.19 · Maximum density τ_c as a function of lateral distance x at the shower maximum. Also shown are curves for $x < x_0$ (dashed) and $x > x_0$ (dotted) according to the parameterization in (3.20).

Using the CORSIKA code, we have built a library of simulations of air showers. Analysis of this library shows that, to a large extent, all extensive air showers show universal behaviour, making the distributions in them dependent on only two parameters: the atmospheric depth X_{max} where the number of particles in the air shower peaks and the total number of particles N_{max} present in the shower at this depth. The entire structure of the shower follows directly from these two values.

We have found some exceptions to the universality hypothesis in the spatial distribution of particles. Theoretically, these non-universal features can be employed to distinguish primaries on a shower-to-shower basis. In real experiments, however, this would be a difficult task because the effect either amounts to only a few percent, or its behaviour can be mistaken for variations in shower stage.

To support the simulation of secondary radiation effects from extensive air showers, we have provided two-dimensional parameterizations to describe the electron-positron content in terms of stage vs. energy and stage vs. lateral distance. We have also supplied three-dimensional representations of the electron content in terms of stage vs. energy vs. vertical momentum angle, stage vs. energy vs. horizontal momentum angle, stage vs. energy vs. lateral distance close to the shower core, and stage vs. lateral distance vs. arrival time.

Though these parameterizations provide accurate descriptions of electron-positron distributions in air showers, the authors would like to mention that there are

TAB. 3.19 · Parameter values for the energy spectrum in (3.6) for the species of electrons, positrons, and the sum of electrons and positrons.

	A_0	ϵ_1	ϵ_2	γ_1	γ_2
Electrons	$0.485A_1 \exp(0.183t - 8.17t^2 \cdot 10^{-4})$	$3.22 - 0.0068t$	$106 - 1.00t$	1	$1 + 0.0372t$
Positrons	$0.516A_1 \exp(0.201t - 5.42t^2 \cdot 10^{-4})$	$4.36 - 0.0663t$	$143 - 0.15t$	2	$1 + 0.0374t$
Total	$A_1 \exp(0.191t - 6.91t^2 \cdot 10^{-4})$	$5.64 - 0.0663t$	$123 - 0.70t$	1	$1 + 0.0374t$

no theoretical grounds for most of the functional representations suggested in this work. Their choice is justified only by the functions' abilities to accurately reproduce the simulated distributions as fit functions. Additionally, the parameterizations provided are based on simulations with a single interaction model only. Though no significant changes are expected in the general behaviour, the parameters listed will likely change when a different model is employed.

When used together with a longitudinal description for the total number of particles, accurate characterizations of any large air shower in terms of the relevant quantities can be calculated. These may be used for realistic electron-positron distributions without the need for extensive simulations and could be useful in calculations of fluorescence, radio or air Cherenkov signals from very-high-energy cosmic-ray air showers.

ACKNOWLEDGEMENTS

The authors wish to express their gratitude to Markus Risse whose help was indispensable in setting up the simulations, and to an anonymous referee for useful suggestions for improving the manuscript. This work is part of the research programme of the 'Stichting voor Fundamenteel Onderzoek der Materie (FOM)', which is financially supported by the 'Nederlandse Organisatie voor Wetenschappelijk Onderzoek (NWO)'.

3.A · FIT PARAMETERS

This appendix explains in detail the various parameters used in the functional parameterizations throughout this paper. All of these were obtained by performing minimalisation sequences using a nonlinear least-squares Marquardt-Levenberg algorithm.

Energy spectrum The parameters in the energy spectrum distribution function as put forward in (3.6) were chosen to match those advocated in Nerling et al. (2006). A good description is obtained with the parameters listed in Table 3.1. The constants in ϵ_1 and ϵ_2 are in MeV; the constant A_0 is provided here for all three cases to obtain charge excess values; the overall parameter A_1 in the table, which is the same for the three distributions, follows directly from normalisation constraints.

Vertical angular spectrum The distribution of the particles' momentum angle away from the shower axis can be parameterized accurately as

$$n(t;\ln\epsilon,\Omega) = C_0\left[\left(e^{b_1}\theta^{\alpha_1}\right)^{-1/\sigma} + \left(e^{b_2}\theta^{\alpha_2}\right)^{-1/\sigma}\right]^{-\sigma}, \tag{3.8}$$

For secondary energies 1 MeV $< \epsilon <$ 10 GeV and angles up to 60°, the curves are described well for $n(t;\ln\epsilon,\Omega) > 10^{-4}$ by setting the parameters in the equations above, using nine free parameters, to

$$\begin{aligned} b_1 &= -3.73 + 0.92\epsilon^{0.210}; \\ b_2 &= 32.9 - 4.84\ln\epsilon; \\ \alpha_1 &= -0.399; \\ \alpha_2 &= -8.36 + 0.440\ln\epsilon. \end{aligned} \tag{3.21}$$

The constant σ is a parameter describing the smoothness of the transition of the distribution function from the first term near the shower axis to the second term further away and was set to $\sigma = 3$. The overall factor C_0 follows from the normalisation condition.

Horizontal angular spectrum The horizontal distribution of momentum is given by

$$n(t;\ln\epsilon,\phi) = C_1[1 + \exp(\lambda_0 - \lambda_1\phi - \lambda_2\phi^2)], \tag{3.10}$$

where optimal agreement is reached in the intervals 1 MeV $< \epsilon <$ 10 GeV and $-6 < t < 9$ by setting

$$\begin{aligned} \lambda_0 &= 0.329 - 0.0174t + 0.669\ln\epsilon - 0.0474\ln^2\epsilon; \\ \lambda_1 &= 8.10\cdot10^{-3} + 2.79\cdot10^{-3}\ln\epsilon; \\ \lambda_2 &= 1.10\cdot10^{-4} - 1.14\cdot10^{-5}\ln\epsilon, \end{aligned} \tag{3.22}$$

with all energies in MeV. There were eight free parameters in total in the fit. The value of C_1 follows directly from the normalisation in (3.5).

Lateral spectrum The NKG-like function to describe the primary peak in the lateral electron distribution is defined as

$$n(t;\ln\epsilon,\ln x) = C_2' x^{\zeta_0'}(x_1' + x)^{\zeta_1'}. \tag{3.14}$$

The fit was performed in the interval 1 MeV $< \epsilon <$ 10 GeV, with the additional condition that $x < 5x_c$ in order to discard the second, species-dependent peak. Optimal correlation

is obtained by using the parameters

$$\begin{aligned}
x_1' &= 0.859 - 0.0461 \ln^2 \epsilon + 0.00428 \ln^3 \epsilon; \\
\zeta_t &= 0.0263t; \\
\zeta_0' &= \zeta_t + 1.34 \\
&\quad + 0.160 \ln \epsilon - 0.0404 \ln^2 \epsilon + 0.00275 \ln^3 \epsilon; \\
\zeta_1' &= \zeta_t - 4.33,
\end{aligned} \tag{3.23}$$

with nine free parameters in total. The value of ϵ is always expressed in MeV. Again, the value of C_2' follows directly from normalisation constraints and will not be discussed here.

Shape of the shower front The shape of the shower front is parameterized as

$$n(t; \ln x, \tau) = C_3 \exp[a_0 \log \tau' - a_1 \log^2 \tau'], \tag{3.17}$$

based on the gamma probability distribution, with

$$\tau' \equiv \tau e^{-\beta_t t - \beta_s}. \tag{3.18}$$

The following parameters give optimal results:

$$\begin{aligned}
a_0 &= -5.99 + 0.638 \log^2 x + 0.230 \log^3 x \\
&\quad - 0.0168 \log^4 x - 0.00416 \log^5 x; \\
a_1 &= 0.853 + 0.333 \log x + 0.0410 \log^2 x \\
&\quad - 0.00724 \log^3 x.
\end{aligned} \tag{3.24}$$

The value for β_t is fixed at $\beta_t = 0.20$, while β_s depends on the primary species:

$$\begin{aligned}
\beta_s &= -0.062 && \text{for iron nuclei;} \\
\beta_s &\equiv 0 && \text{for protons;} \\
\beta_s &= 0.103 && \text{for photons.}
\end{aligned} \tag{3.25}$$

These parameters are valid for distances of $0.4 < x < 10^2$ and $10^{-4} < \tau' < 10$.

4 · *Parameterization of radio geosynchrotron pulses from extensive air showers*

S. Lafebre, T. Huege, H. Falcke, J. Hörandel, J. Kuijpers
This chapter is to be submitted to Astroparticle Physics

Through their interaction with the Earth's magnetic field, extensive air shower particles emit synchrotron radiation at radio frequencies. By analyzing a set of detailed simulations we provide a parameterization of the absolute value of the electric field strength produced by this effect. We start from the principle of universality, allowing us to describe the pulse in terms of the depth of the shower maximum, the number of particles in the shower at this depth, and the angle between the shower axis and the Earth's magnetic field. The description presented here accurately reproduces the dependencies of the quantities involved. It may be used to accelerate simulations for experiments measuring extensive air showers through their radio signature.

4.1 · INTRODUCTION

After the initial discovery of radio emission from extensive air showers in the 1960s and 1970s, the detection of cosmic rays by means of secondary electromagnetic radiation has received renewed interest in recent years, both from a theoretical point of view (Huege & Falcke, 2003; Scholten et al., 2006) and experimentally (Falcke et al., 2005; Ardouin et al., 2005). Today, it is believed that the geomagnetic synchrotron effect is mainly responsible for the electromagnetic pulse at radio wavelengths (Falcke & Gorham, 2003).

To estimate the pulse height and shape produced by this effect, an advanced simulation code called *REAS* has been under development for some years (Huege & Falcke, 2005b; Huege et al., 2007). An earlier version of this code was used to produce a parameterization for the absolute filtered electric field strength (Huege & Falcke, 2005b), but a recent extension to the code allowing one to use accurate shower particle distributions from CORSIKA calls for a re-evaluation of these results.

This analysis is carried out to some extent in this work using version 2.58 of REAS, but instead of parameterizing the maximum field strength only, we aim to provide here a full description of the raw, unfiltered electric field produced by the air shower particles as a function of time.

4.2 · METHOD

The geosynchrotron pulse emitted by an extensive air shower is the result of the interaction of the electrons and positrons in the shower with the geomagnetic field. Therefore, we expect that the only quantities influencing the shape and size of the pulse are the distribution of particles in the air shower, the direction and strength of the magnetic field, and the position of the observer. It was shown in chapter 3 of this thesis that the distribution of electrons and positrons in any large air shower can be characterized up to the level of statistical fluctuations by two parameters only: the depth of maximum of the air shower and the number of particles in the air shower at this depth. Explicit dependencies on primary particle species, primary particle energy, and angle of incidence are negligible or not present at all.

These considerations allow us to infer that the observer-independent quantities determining the radio pulse due to geosynchrotron radiation are limited to four

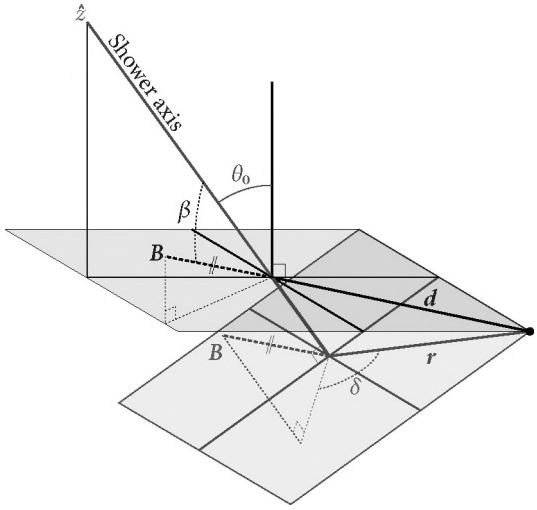

FIG. 4.1 · Explanation of the various angles and distances for a detector marked by the black dot on the right. The horizontal plane represents the ground, and the shower's reference frame is drawn as the slanted plane, rotated by the zenith angle θ_0. The distances $\boldsymbol{d} = (d_x, d_y)$ and $\boldsymbol{r}$ are also shown, as well as the angles β and δ with respect to the magnetic field $\boldsymbol{B}$ (dotted).

parameters only. The first is the depth of the shower maximum $X_{\max}$, represented here by the distance R of the observer to the shower maximum. Using a length scale instead of a column density is more appropriate for radio signals, since they are not attenuated in the atmosphere, unlike particles. The other parameters are the total path length of electrons and positrons $\int N_e(X)\,\mathrm{d}X$ in the shower, the strength of the magnetic field $|\boldsymbol{B}|$, and the angle β between the magnetic field and the angle of incidence of the air shower. The shape of the received raw radio pulse is described in this work as a function of these parameters.

Two more parameters are introduced to account for the position (d_x, d_y) of a detector relative to the impact position of the shower axis. Transformed to the shower's reference frame, the distance takes the form

$$r = \sqrt{d_x^2 + d_y^2 \cos^2\theta_0}, \tag{4.1}$$

where d_y is the projected distance on the ground in the direction of propagation of the shower, and θ_0 is the zenith angle of incidence of the cosmic-ray particle. The angle δ, calculated from

$$\cos\delta = \frac{\hat{r}\cdot\left[\hat{z}\times(\boldsymbol{B}\times\hat{z})\right]}{\hat{z}\times(\boldsymbol{B}\times\hat{z})} \tag{4.2}$$

is the azimuth angle in the shower plane between the observer and the magnetic field direction, where $-\hat{z}$ is the direction of propagation of the air shower. Fig. 4.1 shows the relevant distances and angles in the ground and shower reference frames.

As input for REAS, we used electron-positron distributions from a library of CORSIKA showers, presented in chapter 2. In total, 1400 geosynchrotron simulations were run, with energies of 10^{16}–$10^{20.5}$ eV, initiated from zenith angles of $\cos\theta_0 = 1, 0.9, \ldots, 0.5$, and from azimuth angles of 0°, 45°, …, 180°. For each shower, radio pulses were calculated for 160 positions on the ground: 10 distances between 40 and 750 m at 16 azimuthal angles. The magnetic field strength was taken constant at a value of 49 μT and an elevation angle of 68°. These values correspond to the situation in the Northern Netherlands, where the LOFAR array is being constructed (Falcke et al., 2006). The observer height was fixed at 100 m above sea level, making the results valid in the range of 0–200 m given typical variations in air pressure.

Radio pulses resulting from geosynchrotron radiation show a high degree of linear polarisation. In this work, the parameterizations discussed only deal with the absolute value of the raw, unfiltered electric field, ignoring this polarisation.

4.3 · OVERALL PULSE SHAPE

The time-dependent field strengths obtained by REAS are generally highly asymmetric, with short rise times and long decay times. When plotted on a double-logarithmic scale, however, both the rising and falling edges can be approximated well by a series of straight lines, provided that a correct value for the start time t_0 of the pulse is chosen. Three distinct regions can be identified: a short rising phase, a slower falling phase and a slightly steeper falling phase toward the very tail of the pulse. For observers far away from the shower impact location, the latter two regions merge into an uninterrupted decay. To describe this shape, we propose the following functional form:

$$|\boldsymbol{E}(t)| = \left[\sum_{i=1}^{3} E_i^{-1/\sigma}\,(t - t_0)^{-\gamma_i/\sigma}\right]^{-\sigma}. \tag{4.3}$$

In this expression, each term in the summation describes one of the straight regions of the pulse, together forming an envelope around the pulse. Applying the exponents in σ ensures a smooth transition from each part of the envelope to the other, the actual shape always remaining inside the envelope. The value of σ was fixed at $\sigma = 2$. One should bear in mind that there is no physical or theoretical basis for this parameterization. Its application is justified, however, by its excellent capability of describing the pulse shape for a wide range of parameters, as we shall see.

As an example of the structure of the electric field and its proposed parameterization, Fig. 4.2 shows the field $|\boldsymbol{E}(t)|$ received by an observer at a distance 39 m north of the shower impact location. The pulse shown was computed from a simulated vertical air shower initiated by a proton of $10^{19.5}$ eV. The points in the background are the field strength values as simulated with REAS, the solid line on top is a fit of (4.3) for suitable

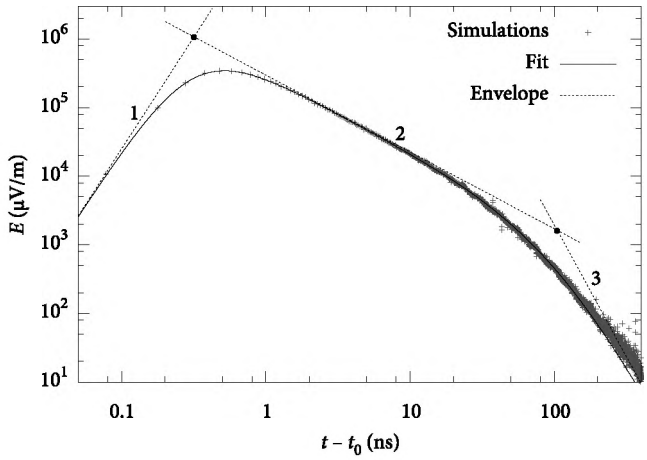

FIG. 4.2 · Example of the fit of (4.3) to an unfiltered geosynchrotron electric field pulse produced by a 10^{18} eV proton-induced vertical air shower. The dotted lines marked 1, 2 and 3 represent the different terms in the summation. Note that both the horizontal and vertical axis are logarithmic.

choices of t_0, E_i, and γ_i to these simulations. The drawn line follows the simulation very accurately. The dotted lines represent the three terms $E_i(t - t_0)^{\gamma_i}$ in the summation for $i = 1$, 2 and 3. There is a slight systematic error of the fitted solid line compared to the simulations at the tail of the pulse for $t - t_0 > 200$ ns, but this error amounts to only a tiny part of the total power of the pulse.

Every single simulated pulse can be described using (4.3) to within an error margin of only a few percent when a fit of the seven parameters E_i, γ_i and t_0 is performed independently. To arrive at an accurate external description of the pulse, however, they should be fixed in terms of the quantities $X_{\max}$, $N_{\max}$, $|\boldsymbol{B}|$, β, and $\boldsymbol{r}$.

To this end, the coordinates of the intersection points of the lines describing the envelope, indicated by black dots in Fig. 4.2, can be defined in terms of the values of E_i and γ_i. The time coordinates of these two points are given by

$$t_{1,2} - t_0 = \left[\frac{E_2}{E_1}\right]^{1/(\gamma_1-\gamma_2)} \qquad \text{and} \qquad t_{2,3} - t_0 = \left[\frac{E_3}{E_2}\right]^{1/(\gamma_2-\gamma_3)}, \tag{4.4}$$

and the field strengths at these points can be found from

$$E_{1,2} = \left[\frac{E_2^{\gamma_1}}{E_1^{\gamma_2}}\right]^{1/(\gamma_1-\gamma_2)} \qquad \text{and} \qquad E_{2,3} = \left[\frac{E_3^{\gamma_2}}{E_2^{\gamma_3}}\right]^{1/(\gamma_2-\gamma_3)}. \tag{4.5}$$

In our parameterization, we will fix E_i and γ_i by empirically finding expressions for the coordinates in (4.4). To obtain these expressions, first each pulse was fitted independently to (4.3). Following this, mathematical descriptions for the parameters t_0, $t_{1,2}$, $t_{2,3}$, $E_{1,2}$, and $E_{2,3}$ were obtained from analysis of the values of the fit parameters γ_i and E_i in terms of $X_{\max}$, $N_{\max}$, $|\boldsymbol{B}|$, β, and $\boldsymbol{r}$. The results of this process are explained in the next sections. As mentioned earlier, the value for the smoothing factor was always held constant at $\sigma = 2$, since this value was found to produce acceptable results. Numerical values in the remainder of this work are such that all field strengths have the dimension μV/m, lengths are in m, and time is always in ns.

4.4 · TIME PARAMETERS

Analysis of the fitted values for t_0, $t_{1,2}$ and $t_{1,3}$ shows that their dependencies on r and R can be removed almost completely by making use of a function with the proportionality

$$\propto r^{\alpha_r}(R + R_0)^{\alpha_R}, \tag{4.6}$$

where r is the perpendicular distance from the observer to the shower axis in the shower's reference frame as defined in (4.1). The distance $R + R_0$ represents the distance from the observer to an imaginary source position from which the air shower originates. This total distance is subdivided into R_0, representing the distance from the point of origin to the shower maximum, and R, which is the distance from the shower maximum to the observer. The value of R_0, which does not greatly influence the overall quality of the parameterization, is fixed at 6 km.

Let us start with the parameter t_0, which represents the delay in the arrival time of the pulse with respect to a plane wave front propagating from the first interaction point of the primary particle with the speed of light in vacuum. This quantity was found to obey the functional form

$$t_0 = 7.5 \cdot 10^{-5} r^{2.00}(R + R_0)^{-0.65} \quad \text{(in ns)}. \tag{4.7}$$

This equation closely resembles the parameterization (5.4) suggested in chapter 5. This is not very surprising, as the values they characterize are closely related: the latter describes the time delay of the maximum field strength, and (4.7) is concerned with the time delay of the start of the pulse. By taking their difference, therefore, an expression for the rise time of the pulse may be obtained.

The time coordinates of the intersections were found to obey the following parameterization:

$$\begin{aligned} t_{1,2} - t_0 &= 10^{-0.144} r^{1.91}(R + R_0)^{-1.20} \\ \text{and} \qquad t_{2,3} - t_0 &= 10^{5.60} r^{0.912}(R + R_0)^{-1.24} + 55.2 \quad \text{(both in ns)}. \end{aligned} \tag{4.8}$$

For the time parameters t_0, $t_{1,2}$ and $t_{2,3}$, no appreciable dependence on the magnetic field angle was found.

4.5 · FIELD STRENGTH PARAMETERS

Since the geosynchrotron signal emitted by air showers is largely coherent, the overall pulse height is expected to be proportional to the total number of electrons and positrons in the air shower. Assuming that the number of particles at the shower maximum $N_{\max}$ is a good estimator for the path length integral for electrons and positrons, and assuming that there is a linear correlation between the two, dependence of the pulse shape on $\int N(X)\,\mathrm{d}X$ is limited to an overall scale factor $|\boldsymbol{E}| \propto N_{\max}$. This behaviour was found to be obeyed to an acceptable level, i.e. within the limit of shower-to-shower fluctuations.

Not surprisingly, the field strengths $E_{1,2}$ and $E_{2,3}$ are highly dependent on the angle with respect to the magnetic field. Their description is therefore somewhat more complicated. Acceptable results are obtained by setting the electric field strengths corresponding to $t_{1,2}$ and $t_{2,3}$, respectively, to match

$$\begin{aligned}
\log E_{1,2} - \log N = {} & (\ 4.18 + 13.5\cos 2\delta) \\
& + (\ -10.1 + 1.47\cos 2\delta)\log r \\
& + (\ 2.78 + -5.46\cos 2\delta)\log(R + R_0) \\
& + (\ -0.483 + 0.564\cos 2\delta)\log^2(R + R_0) \\
& + (\ 1.35 + -0.264\cos 2\delta)\log(R + R_0)\log r \\
& + 0.379\log(1 - \cos\beta),
\end{aligned} \tag{4.9}$$

and

$$\begin{aligned}
\log E_{2,3} - \log N = {} & (\ -3.59 + 0.208\cos 2\delta) \\
& - 0.0336\log r \\
& - 0.430\log(R + R_0) \\
& + 0.379\log(1 - \cos\beta).
\end{aligned}$$

Note the typical dependence on $1 - \cos\beta$ from (4.9), which produces better fits than a dependence on $\sin\beta$. This behaviour was noticed earlier in experimental setups (Falcke et al., 2005; Horneffer, 2006), though only the east-west polarisation was measured there. For very small angles β smaller than a few degrees, this proportionality breaks down, since there is some variation in the vertical momentum angles of the electrons and positrons in an air shower, blurring the effective value of the magnetic angle.

Another dependence that was reported experimentally by the LOPES array is a correlation of the field strength with the cosine of the zenith angle θ_0. This dependence does not show up in our parameterization, as it is hidden in the definition of R: inclined showers tend to have their shower maximum further away from the observer.

Using the four equalities in (4.8) and (4.9), values for γ_2 and E_2 are established, and only two degrees of freedom remain in the overall parameterization. These are determined by setting

$$\gamma_1 = 3 \qquad \text{and} \qquad \gamma_3 = -3.84. \tag{4.10}$$

With these definitions, the entire pulse shape is determined.

In total, 27 free parameters were used to fit the pulse shape. This is a significant amount, but one should bear in mind that an accurate description of a single pulse requires no less than seven parameters, and it is not unreasonable to expect four times that number for a fit in five dimensions.

4.6 · PULSE SHAPE EXAMPLES

In this section, we compare pulse shapes produced by REAS to their parameterizations as put forward in this work. The behaviour with respect to various quantities is shown. In Figs. 4.3–4.7, the simulated pulse shape is represented by points, and the reconstructed parameterized pulse shape is shown as a solid line.

All plots in this section were selected on their input properties only, and no selection was made on the quality of the fit. Also note that the primary particle species does not enter the selection criteria: within statistical limits, we expect no intrinsic difference between showers initiated by photons, protons or iron nuclei other than a systematic shift of $X_{\max}$. This factor has already been accounted for in our parameterization, however.

Let us start with the dependence on $N_{\max}$. Fig. 4.3 shows the simulated pulse shape $E/N_{\max}$ at 40 m from the shower core at $\delta = 0°$ for six vertical showers with a shower maximum at around 755 g/cm^2 or $R \simeq 2.6$ km. Note that the electric field strength is divided by $N_{\max}$ in the examples in this section. Therefore, the six parameterizations shown in Fig. 4.3 a re identical, corresponding to the right hand side terms in (4.9). Though both primary energy and number of particles in the shower extend over more than four orders of magnitude in these plots, no noticeable change in the pulse shape can be observed. This is a direct consequence of the principle of universality in air showers, which states that the shape of electron and positron distributions in any air shower depends only on $X_{\max}$, while its size is proportional only to $N_{\max}$.

Some examples of the dependence of the pulse shape on $X_{\max}$ are shown in Fig. 4.4. Each of the six plots represents the pulse shape at $r \simeq 120$ m from the core, with $\delta = 0°$. In order to keep the angle β constant, only vertical showers were included ($\beta \simeq 22°$). The parameterizations accurately trace the simulated pulses, except for the bottom right case. This discrepancy can be justified by considering that the distance from the shower maximum to the observer (at $X \simeq 1024$ g/cm^2) is -380 m for this shower: a negative value. Since the main part of a shower's geosynchrotron radiation is emitted downward, this implies that a significant portion of the produced signal is simply not detected, explaining the low field strength. To a lesser extent, this effect can also be seen in the bottom left plot.

Next, we consider the dependence on the distance to the shower core impact position r; see Fig. 4.5. The overall behaviour is reproduced well by the parameterization, but a slight overestimation of the field strength can be observed at large distances. This effect is seen in other showers as well, and amounts to an overestimation of about 15 %

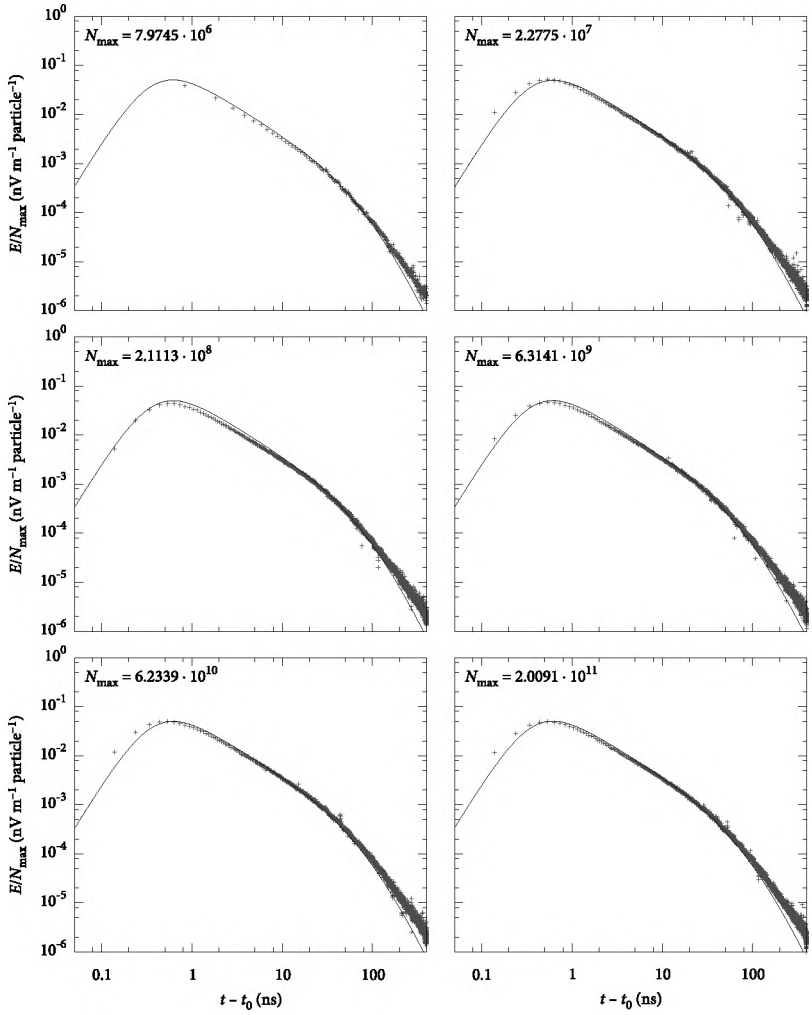

FIG. 4.3 · Dependence of the pulse shape on the number of particles at the shower maximum N_{max} for various vertical showers with $X_{max} \simeq 755\,g/cm^2$, $r \simeq 40\,m$, and $\delta = 0°$.

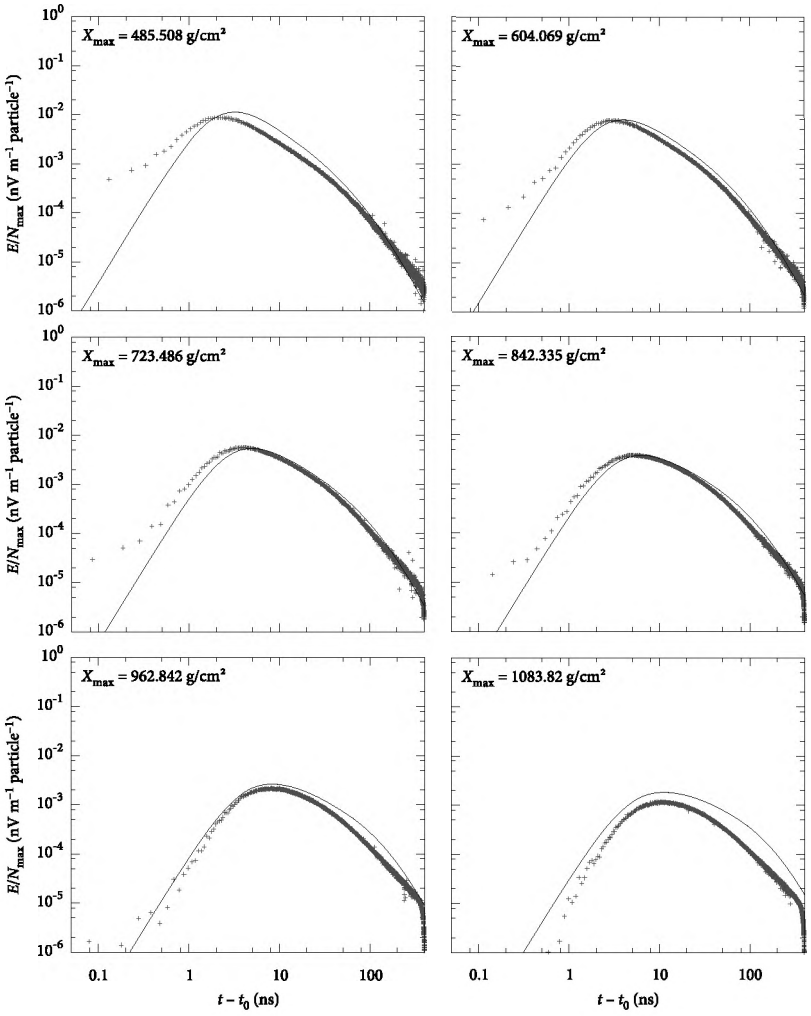

FIG. 4.4 · Dependence of the pulse shape on the distance R to the shower maximum for different values of $X_{\max}$ for vertical showers with $r \simeq 118$ m, $\delta = 0°$, at various energies. Note the discrepancy for the plot at $X_{\max} = 1083.82$ g/cm^2.

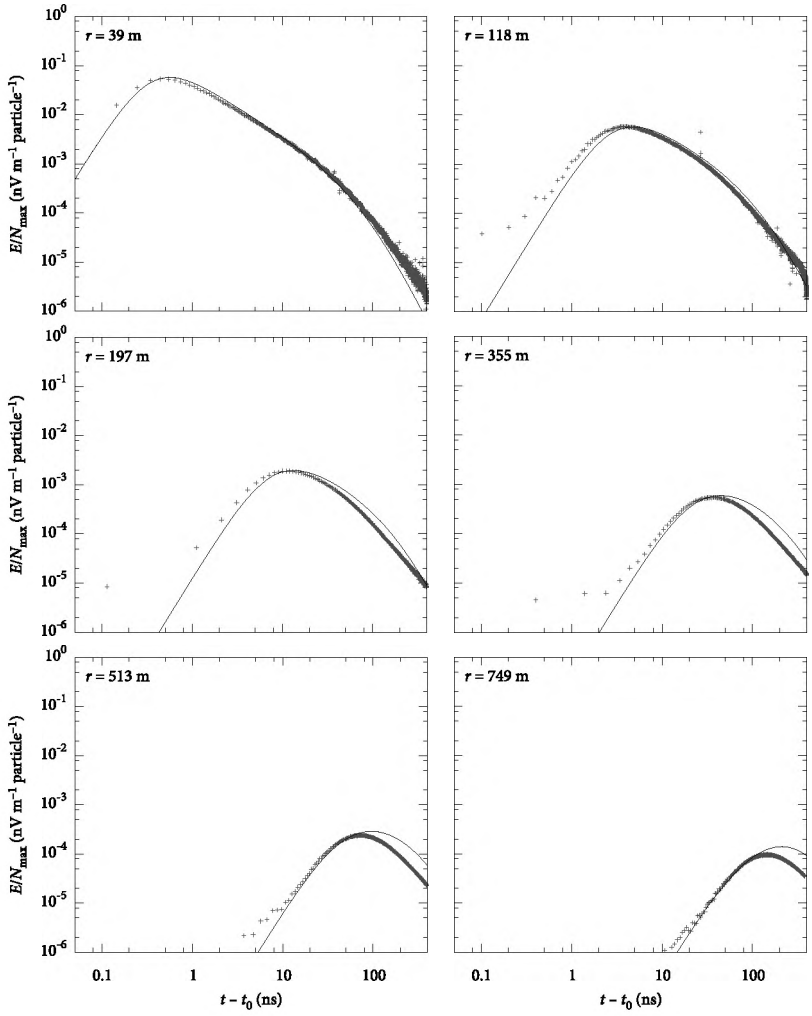

FIG. 4.5 · Dependence of the pulse shape on the distance in the shower reference frame to the shower core r. For the plots shown here, produced from a single vertical shower, $X_{\max} \simeq 708\,\mathrm{g/cm^2}$, $N_{\max} \simeq 6.4 \cdot 10^9$, and $\delta = 0°$.

at $r = 500$ m, increasing to an error of nearly 40 % at $r = 750$ m. This is because only the initial 400 ns of signal was computed for each pulse, cutting off the tail for very far showers.

From Fig. 4.6 we see that the behaviour of the pulse shape with δ cannot be neglected: the field strength decreases significantly when the observer is at right angles to the magnetic field. This effect was noticed earlier by Huege et al. (2007). In fact, the field strength as a function of δ is much more complicated than the description proposed in this work, producing a pattern that is symmetric under rotation over 180°, but not mirror symmetric. To account for this, the terms $(a_0 + a_1 \cos 2\delta)$ in (4.9) would have to be replaced by a more complicated function. For the shower shown in the figure, the magnetic field angle lies in the $(\hat{y}, \hat{z})$ plane, hence no such effect is visible.

Apart from an asymmetry in electric field strength, there is also a small yet noticeable asymmetry in the values of t_0 around the $\hat{x}$ axis which is not taken into account in our parameterization. This asymmetry has been observed as well in the simulations in chapter 5, dealing exclusively with pulse timing, where it was incorporated as a term in $\cos \delta$. We have chosen to neglect its effect here, since it is quite small compared to other systematic errors in the parameterization.

Finally, we examine the dependence on the angle β between $\boldsymbol{B}$ and $-\hat{z}$. Fig. 4.7 shows the pulses produced by showers at different zenith angles, with geomagnetic angles $3.8° < \beta < 75°$. The distance to the shower maximum was $R \simeq 5.9$ km in all cases. The produced field strength per particle varies significantly with the geomagnetic angle: it stretches over two orders of magnitude for this range of β. Overall, the behaviour is reproduced well by our description. At very small angles, however, the field strength is overestimated, while there is an underestimation of similar magnitude for very large angles.

All in all, our parameterization provides satisfactory descriptions of the pulse shapes in most cases. Errors are smaller than 30 % for $r < 650$ m, $5° < \beta < 60°$, and $0.5 \text{ km} < R < 15 \text{ km}$. It may be used to quickly obtain expected signals in performance studies of arrays of radio antennas such as the LOFAR telescope (Falcke et al., 2006) or the initiative to extend the Piere Auger array with radio antennas (Van den Berg & et al., 2007).

4.7 · DISCUSSION

There are some limitations to the parameterization (4.3) of the computed pulse shapes described here. First and foremost, the magnetic field was kept at a constant field strength in all simulations, so the dependence on this quantity has not been determined. Since $|\boldsymbol{B}|$ does not vary by more than a factor of 2 over the Earth's surface, significant corrections other than multiplying by $|\boldsymbol{B}|/49\ \mu\text{T}$ are not to be expected, however.

Additionally, the parameterization put forward in this work does not describe the polarisation of the received signal, since (4.3) describes the absolute field strength rather than the vector. To obtain full vector information, the polarisation of the signal

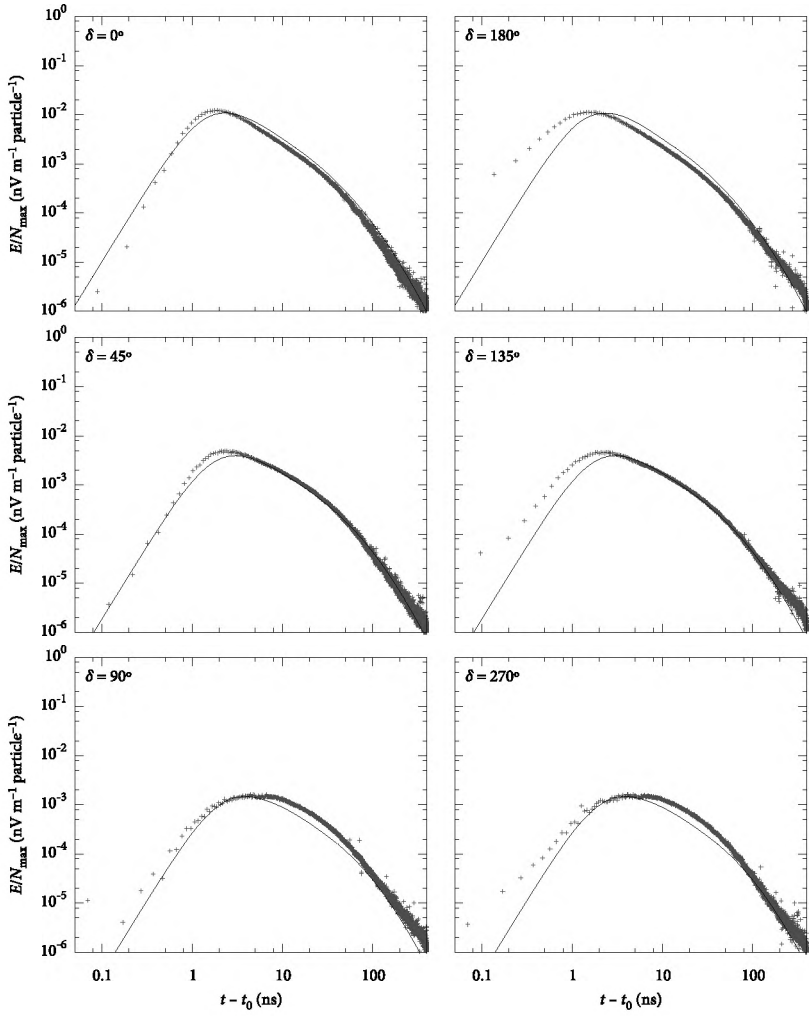

FIG. 4.6 · Dependence of the pulse shape on the angle δ. For the plots shown here, produced from a single shower with $\beta \simeq 15°$, $X_{max} \simeq 782\,g/cm^2$, $N_{max} \simeq 2.1 \cdot 10^9$, and $|d| \simeq 118\,m$.

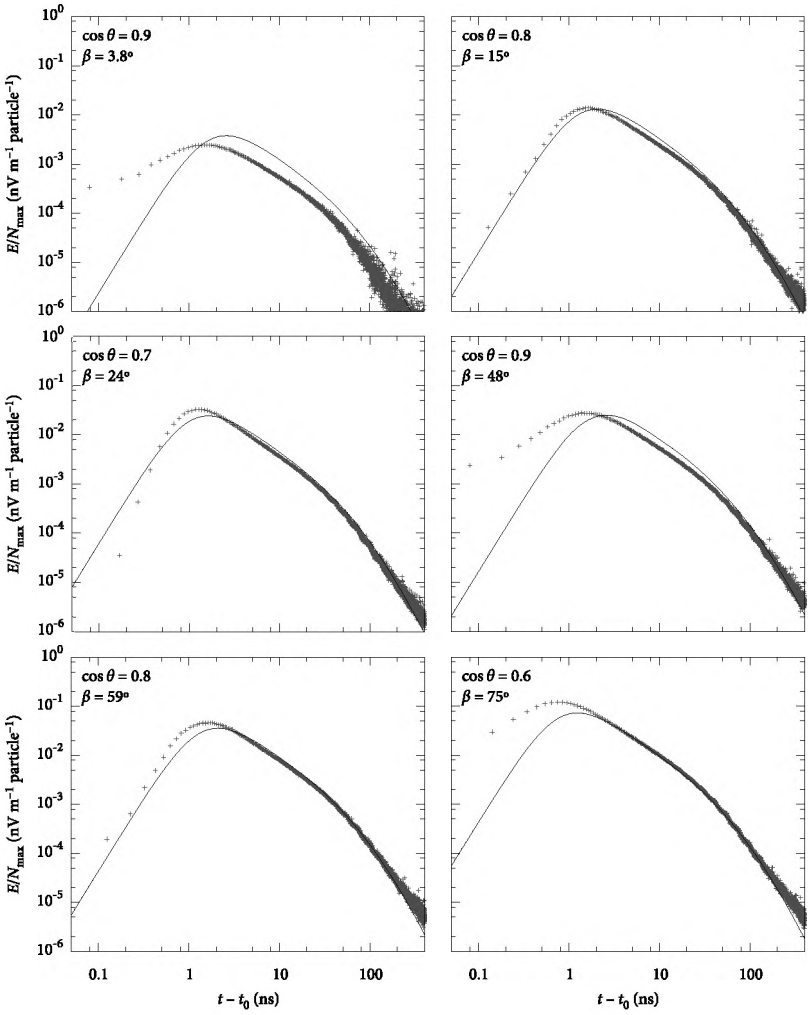

FIG. 4.7 · Dependence of the pulse shape on the geomagnetic angle β for different showers with $R \simeq 5.9$ km with $r \simeq 118$ m and $\delta = 0°$, at various energies and angles of incidence.

should be incorporated. One should also keep in mind that only the field strength due to geosynchrotron radiation is included in the REAS code, neglecting other effects such as creation/annihilation radiation, Cherenkov radiation, and transition radiation.

Pulse reconstruction is unsatisfactory in some areas, primarily occurring at very small geomagnetic angles ($\beta < 5°$), at long distances ($r > 600$ m), and at high zenith angles ($\theta_0 > 55°$). If these limits are respected, the parameterization presented here produces very reliable estimates for the expected pulse shapes with errors of less than 20 %.

Ideally, one could use the description of the pulse shape to obtain the energy in the radio pulse directly by integrating over the Poynting vector $\boldsymbol{S}$, which is proportional to the square of the electric field. A serious disadvantage of the proposed parameterization is that its time integral has no analytical representation. One can, however, set an upper limit to the energy in the pulse by making use of the envelope of the pulse. Alternatively, a numerical integration of the pulse shape obtained can be performed.

4.8 · CONCLUSION

From a set of detailed simulations of the geosynchrotron radiation emitted by extensive air showers, we have obtained a parameterization for the absolute field strength resulting at arbitrary locations. We have described the pulse in terms of the depth of the shower maximum, the number of particles in the shower at this depth, the angle between the shower axis and the Earth's magnetic field, and the position of the observer relative to the shower axis. The description reproduces the dependencies of the quantities involved with reasonable accuracy, to within 20 % in most cases. The parameterization presented may be used to quickly derive geosynchrotron emission estimates for experiments measuring extensive air showers through their radio signature.

5 · *Determining air shower characteristics through radio emission arrival times*

S. Lafebre, T. Huege, H. Falcke, J. Hörandel, J. Kuijpers
This chapter is to be submitted to Astroparticle Physics

Using simulations of geosynchrotron radiation from extensive air showers, we present a relation between the shape of the geosynchrotron radiation front and the distance of the observer to the maximum of the air shower. By analyzing the relative arrival times of radio pulses at several radio antennas in an air shower array, this relation may be employed to estimate the depth of maximum of an extensive air shower if its impact position is known, allowing an estimate for the primary particle's species. Vice versa, the relation provides an estimate for the impact position of the shower's core if an external estimate of the depth of maximum is available. In realistic circumstances, the method delivers reconstruction accuracies comparable to those attained in air fluorescence measurements when the distance to the shower core does not exceed 7 km for primary particles requires that the arrival direction is known with high precision.

5.1 · INTRODUCTION

One of the most important open questions in astroparticle physics is the nature of cosmic-ray particles at the highest energies. At energies exceeding 10^{15} eV, at present, the only practical way to investigate cosmic-ray particles is to register extensive air showers induced by cosmic rays in the atmosphere. In such experiments it is only possible to make statements on the composition of primary cosmic rays based on statistical evaluations. Abundances of primary particle types of an ensemble of air showers are frequently derived by looking at the depth of the shower maximum, i.e. the depth at which the number of particles in a shower reaches its maximum.

In recent years, there has been a surge of interest in the detection of extensive air showers by means of the electromagnetic pulse of geosynchrotron emission emitted by the shower particles (Huege & Falcke, 2003; Falcke et al., 2005). This observational technique allows one to look all the way up to the shower maximum, and it has the advantage over detecting the particles themselves at ground level that there is no attenuation of the signal. Previously, it was shown (Huege et al., 2008) that the position of the maximum of inclined showers can be derived from the lateral slope of the electric field strength at ground level.

In this work, we use simulations of air showers and their geosynchrotron radiation to of estimate the value of the depth of maximum and the impact position of the shower core. The method developed exploits delays in the arrival time of the signal at different positions on the ground.

5.2 · METHOD

Detailed distributions of electrons and positrons at different atmospheric depths were obtained from an air shower library (Lafebre et al., 2007) produced with CORSIKA simulations (Heck et al., 1998) and the COAST library (Ulrich, 2007). The library contains air showers initiated by photons, protons, and iron nuclei of energies in the range 10^{16} to $10^{20.5}$ eV, incident from zenith angles up to 60°.

A subset of ~ 700 simulations from this library, chosen at random, was used to calculate the radio signal emitted by these airs showers. The REAS code version 2.58 (Huege & Falcke, 2005a; Huege et al., 2007) was used to obtain the radio pulses

associated with each air shower simulation at an altitude of 100 m above sea level. Antennas were placed on a radial grid at distances of 35 m to 1500 m with intervals of 80–300 m, with one antenna every 45°.

The magnetic field in all simulations, both CORSIKA and REAS, was taken to match values in northwestern Europe at a field strength of 49 μT and a declination of 68°. The height of the detector array was fixed at 100 m above sea level, corresponding to an atmospheric depth of $X \simeq 1024\ \mathrm{g/cm^2}$.

5.3 · PARAMETERIZATION

For showers hitting the detector at an angle, one has to compensate for projection effects. Let θ_0 and ϕ_0 be the zenith and azimuth angle at which the primary enters the atmosphere. For a radio antenna a distance d on the ground away from the shower core in the direction δ with respect to the incidence angle ϕ_0, the perpendicular distance r to the shower core is

$$r = d\sqrt{1 - \cos^2\delta \sin^2\theta_0}. \tag{5.1}$$

The delay τ, converted to length units by multiplying with the speed of light in vacuum, is defined as the lag of the peak strength of the radio signal with respect to the arrival time at the shower impact location. It can be written as

$$\tau = t + d\cos\delta\sin\theta_0, \tag{5.2}$$

where $t(r, \delta)$ is the delay caused by the non-planar shape of the shower front expressed in length units. In the analysis in the remainder of this work, these geometrical compensations have been included.

In the case of a spherical shower particle front, the expected shape of its emitted radio signal is a spherical wavefront as well. The delay t can then be written in terms of the distance to the center of the sphere R and the distance from the shower core r as

$$t = \sqrt{R^2 + r^2} - R \approx \frac{r^2}{2R}, \tag{5.3}$$

where the approximation holds for $r \ll R$. It was shown previously, however, that the assumption of a spherical shower particle front is unrealistic for large air showers (Lafebre et al., 2008a). Therefore, the shape of t as a function of r is expected to be different, too.

The delay of a radio pulse t is defined as the lag between a hypothetical plane wave and the actual maximum of the received signal. Fig. 5.1 shows a contour plot of the distribution on the ground of this lag for a typical vertical proton shower at $E = 10^{18.5}$ eV, with $X_{\mathrm{max}} \simeq 780\ \mathrm{g/cm^2}$. The geomagnetic field points north in this figure. Notice the deviation from circularity of the front, which is strongest near the shower core in the east and west directions. This asymmetry results only from radiation processes and is not a consequence of asymmetries in the particle front of the shower, because the distributions used to create the radio shape are cylindrically symmetric by design (Lafebre et al., 2007).

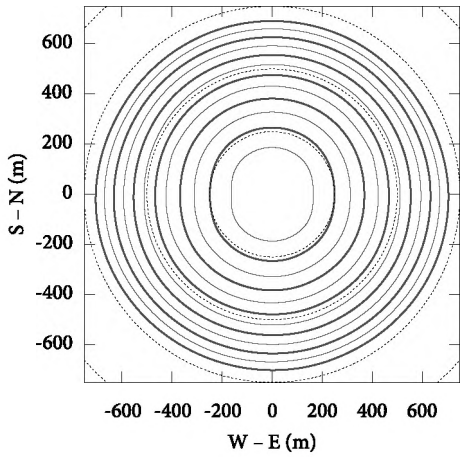

FIG. 5.1 · Radio signal delay for a typical vertical $10^{18.5}$ eV proton shower ($X_{\max} \simeq 780$ g/cm^2). Solid curves represent signal delays τ at intervals of 5 m (thick lines every 10 m). For reference, perfect circles at different distances are also drawn (dotted).

Analysis of a set of ~ 700 showers from photons, protons, and iron nuclei at various energies and incidence angles as described in section 5.2 reveals that, to first order approximation, these delays can be described by the parameterization

$$t = R_1^{1-\alpha-1/\beta} r^{\alpha} (R + R_0)^{1/\beta}, \tag{5.4}$$

where R represents the distance of the impact location to the shower maximum, which can be translated unambiguously to a value of $X_{\max}$. The distance $R + R_0$ represents the distance from the observer to an imaginary source position from which the air shower originates. This total distance is subdivided into R_0, representing the distance from the point of origin to the shower maximum, and R, which is the distance from the shower maximum to the observer. The value of R_0, which does not greatly influence the overall quality of the parameterization, is fixed at 6 km. R_1 is a scale parameter, the exponent of which was chosen to match the dimension of t (distance).

The parameters in the above relation do not depend significantly on either primary energy or zenith angle other than through the respective influences on the depth of the shower maximum. This is not very surprising, because the particle distributions responsible for the radiation do not exhibit any dependence on these parameters either (Nerling et al., 2006; Lafebre et al., 2008a). Though the values for R_0, α, and β depend on the orientation of the shower with respect to the magnetic field, this dependence is much smaller than the average statistical variation between showers. Therefore,

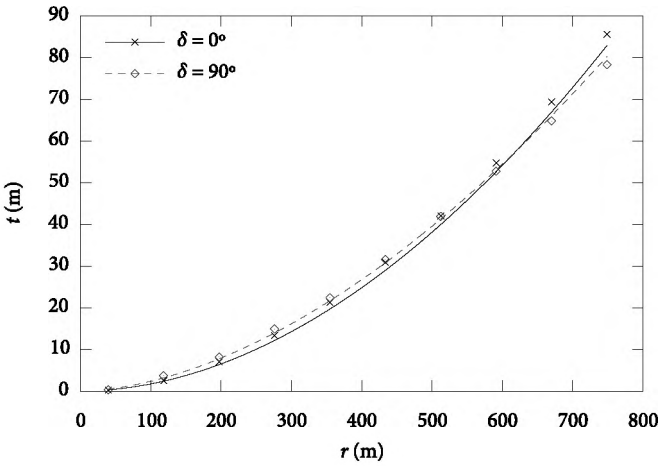

FIG. 5.2 · Example of the parameterization presented in (5.4) and (5.5) for the signal lag for a vertical proton shower at an energy of 10^{20} eV and $X_{\max} \simeq 895\,\mathrm{g/cm^2}$. The simulated lag at $\delta = 0°$ and $\delta = 90°$ is indicated by crosses and diamonds, and their respective corresponding parameterizations are drawn as solid and dashed lines.

we will restrict the variations in the parameters to a dependence on the angle δ only. A fit to the simulated pulse lags in the region $40\,\mathrm{m} < d < 750\,\mathrm{m}$ yields the following overall best-fit parameters:

$$\begin{aligned} R_1 &= 3.87 + 1.56\cos(2\delta) + 0.56\cos\delta \quad \text{(in km)}, \\ \alpha &= 1.83 + 0.077\cos(2\delta) + 0.018\cos\delta, \\ \beta &= -0.76 + 0.062\cos(2\delta) + 0.028\cos\delta. \end{aligned} \tag{5.5}$$

The $\cos(2\delta)$ terms in these equations reflect the asymmetries in the east-west versus north-south direction. Note that $\alpha < 2$ for all δ, confirming the non-spherical shape of the wave front. An example of the parameterization is shown in Fig. 5.2, in which the simulated lags and their corresponding parameterizations are drawn for a vertical proton shower at 10^{20} eV and $X_{\max} \simeq 895\,\mathrm{g/cm^2}$ as a function of distance from the shower impact location. Two sets are shown, for $\delta = 0°$ and $\delta = 90°$, respectively.

The accuracy of our parameterization may be assessed from Fig. 5.3. This plot shows how the distance to the shower maximum R as reconstructed from the parameterization in (5.4) and (5.5) compares to the actual distance as a function of the delay. Note that the figure shows reconstructions of single antennas rather than complete showers: this means that the histogram in this figure is composed of 80 antennas × 700 showers = $5.6 \cdot 10^4$ individual reconstructions. It is no surprise that antennas with

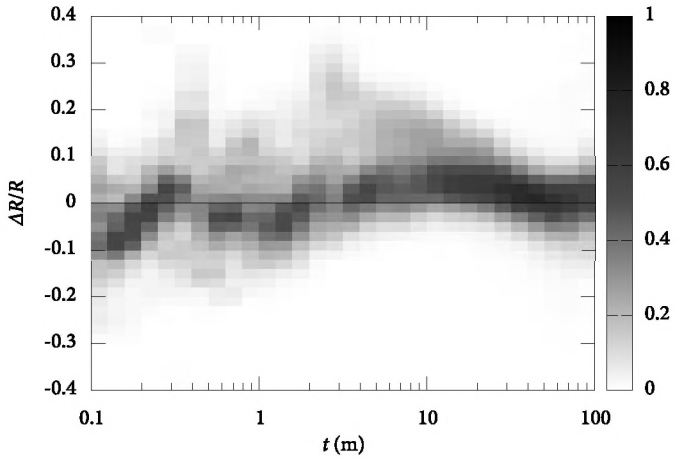

FIG. 5.3 · Relative error in the reconstruction of R as a function of the delay t. Darker areas mark higher numbers of reconstructions. The total amount of colouring is constant for every slice in t; the intensity is in arbitrary units.

longer delays of $t > 10$ m produce more accurate reconstructions, since the relative error is smaller there. Even at arrival lags of less than 1 m, however, the standard deviation is less than 10 % of the actual value.

In a typical array of radio antennas, one can determine the delays τ very accurately: using modern equipment, resolutions down to a few ns can be achieved. We can use the delay values to employ the parameterization in (5.4) in two ways: if the position of the shower core is known accurately by scintillator measurements, we can use it to estimate the distance to the shower maximum. If, on the other hand, an estimate for the depth of maximum is available, the position of the shower core can be reconstructed. We will discuss these approaches in detail in the following two sections.

5.4 · DETERMINING DEPTH OF SHOWER MAXIMUM

By rearranging (5.4), we may write

$$R = R_1^{1-\beta+\alpha\beta} \left(\frac{t}{r^\alpha} \right)^\beta - R_0 \tag{5.6}$$

to reconstruct the distance to the shower maximum. Using this parameterization, the reconstructed distance to the shower maximum is plotted versus the simulated value in the left panel of Fig. 5.4. Each dot in this plot represents the reconstructed value of R for one shower event, obtained by taking a weighted average of the reconstructions from the delays in individual antennas. If the antennas are placed on a regular grid, a

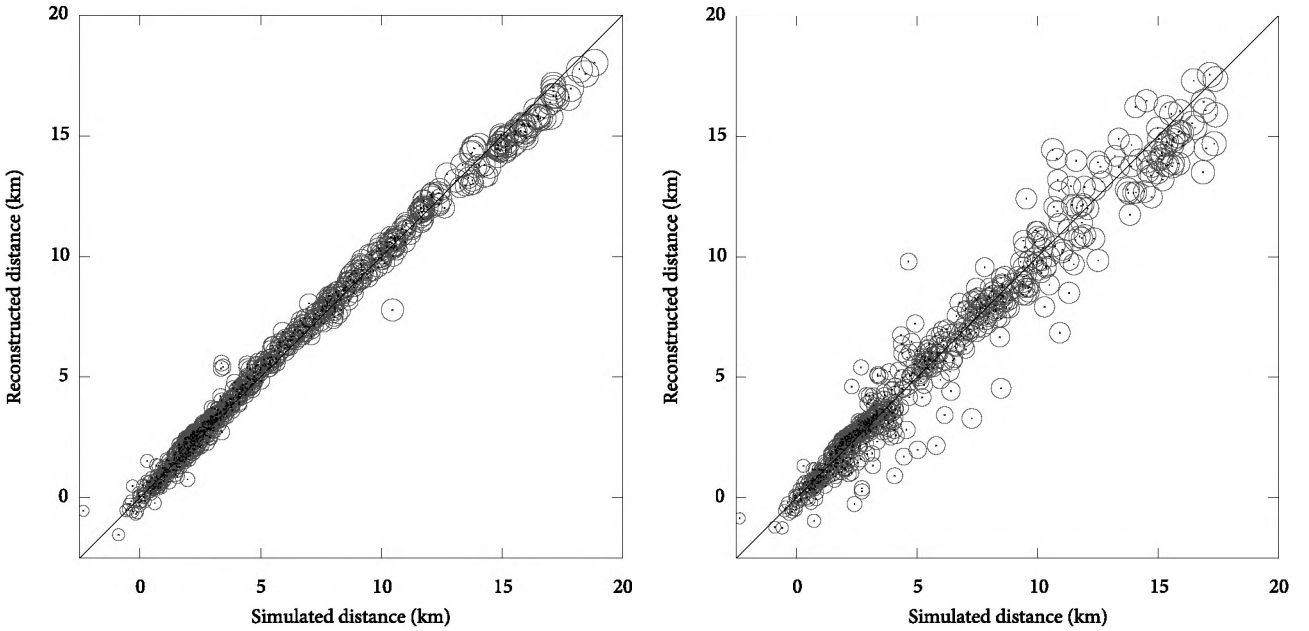

FIG. 5.4 · Scatter plot for ~ 700 showers of various species and energies $E > 10^{17}$ eV of simulated values for R versus the values as reconstructed by the method outlined in the text. Circles around each reconstruction represent error margins of 20 g/cm^2. The left panel shows the theoretical limit in reconstruction accuracy, while in the right plot realistic Gaussian errors were introduced around the observables in (5.6).

weight $\propto r^2$ seems justified to match each time delay to its expected relative error, since $\alpha \simeq 2$. Our simulated array is denser near the shower core, which was compensated for by multiplying by an extra factor of r, arriving at a total weight for each antenna $\propto r^3$.

Around each mark in Fig. 5.4 a circle is drawn, the radius of which is the distance corresponding to an atmospheric depth of 20 g/cm^2 at the position of the simulated air shower maximum. This value represents a typical minimum error margin for reconstructed $X_{\max}$ values using air fluorescence techniques (Dawson & et al., 2007). The algorithm correctly reconstructs the distance to the shower maximum as simulated, with a standard deviation of 216 m. Note that both simulated and reconstructed events extend to negative distances: showers in this region have a maximum that lies below the observation level of the radio antennas. By design of he algorithm, correct reconstruction of these events is possible only if the downward distance is smaller than R_0.

So far, we have considered perfect circumstances, assuming exact knowledge of the impact angle and position of the shower axis as well as the delay of the radio pulses. A more realistic picture emerges by introducing some error sources in the reconstruction. For a dense array of radio antennas, such as the LOPES (Falcke et al., 2005) or LOFAR (Falcke et al., 2006) telescopes, the accuracy in the arrival direction is of the order of 1.0° (Nigl et al., 2008). A feasible time resolution for determining the maximum pulse height is about 10 ns. The accuracy in determining the position of the shower core has not been investigated thoroughly yet using radio detection. Therefore, we adopt a typical value from the analysis of the KASCADE experiment data of 1 m (Antoni et al., 2004; Glasstetter et al., 2005). It is assumed that reconstruction with a dense radio array such as LOFAR, which places antennas at distances of the order of 10 m, will be on a par with this precision level. All of the above errors are assumed to follow Gaussian distributions. Additionally, we ensure that the signal is sufficiently strong by demanding a field strength over 180 μV/m, which corresponds to a signal-to-noise ratio of 10 in a rural area (Huege et al., 2008).

The right panel of Fig. 5.4 shows the situation when these error estimates are included. The correlation is reduced significantly, which is mainly the result of the uncertainty in the arrival direction of the shower. For very inclined showers in particular this can change the expected delay times dramatically. When the accuracy of the shower impact location is reduced, this mostly affects showers for which the maximum lies at a large distance from the observer. When the error is increased to 5 m, for example, hardly any predictions can be made for distances > 10 km.

The fraction of $X_{\max}$ values reconstructed correctly to within an error margin of 500 m (corresponding to an average error in $X_{\max}$ of approximately 50 g/cm^2) is plotted in Fig. 5.5 as a function of energy. In this plot, a homogeneous detector sensitivity up to zenith angles $\theta < 60°$ is assumed. Three background noise scenarios are shown: one for an ideal noise level (requiring a field strength $|\boldsymbol{E}| > 65$ μV/m for successful determination of t), one for a rural environment ($|\boldsymbol{E}| > 180$ μV/m), and one corresponding to an urban area ($|\boldsymbol{E}| > 450$ μV/m) (Huege et al., 2008).

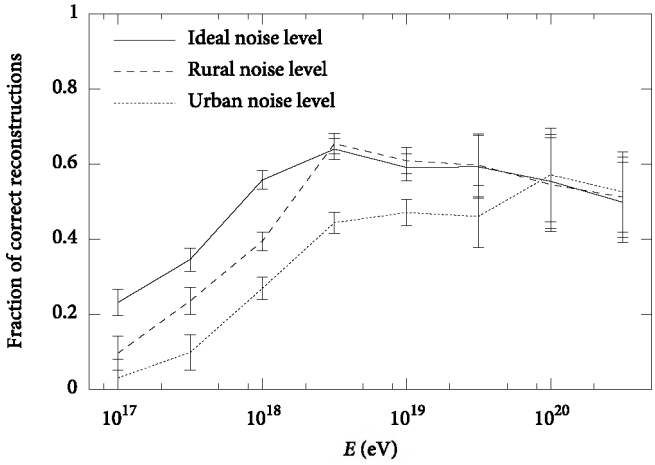

FIG. 5.5 · Fraction of correctly reconstructed distances to the depth of maximum (error of less than 500 m) as a function of primary energy. Different scenarios are shown for ideal, rural, and urban noise levels. Error bars are based on the number of simulations for each energy.

From this figure, we observe that the amount of successfully reconstructed values for $X_{\max}$ decreases rapidly at low energies. This is because low-energy showers do not occur very deep in the atmosphere on average, raising the distance to the shower maximum. This results in a radiation front with less curvature, necessitating delay measurements further away from the impact location to obtain the same level of reconstruction accuracy. The produced field strength, however, is proportional to the primary energy, decreasing the patch size that is sufficiently illuminated. The combined effect is that it is hard to make correct estimations for the depth of maximum of low energy showers, unless an array at high altitude is employed. The fraction of correct reconstructions becomes flat at very high energies of $E > 10^{19}$ eV. For these energies, the distance up to which a signal can be seen even for urban noise levels is much longer than the maximum distance d of 1500 m up to which the simulated radio signal was calculated. This prevents proper reconstruction when the shower maximum is close to the observer. Since values for $X_{\max}$ increase on average with energy, a slight decrease can even be observed above this energy.

If the maximum available distance to the shower core is very small, as would be the case for an array such as LOPES, the fraction of good reconstructions is reduced dramatically. This makes sense, as the shower front shape can no longer be probed accurately. In particular, if the radius of the array decreases to less than ~ 500 m, the amount of useful reconstructions is negligible.

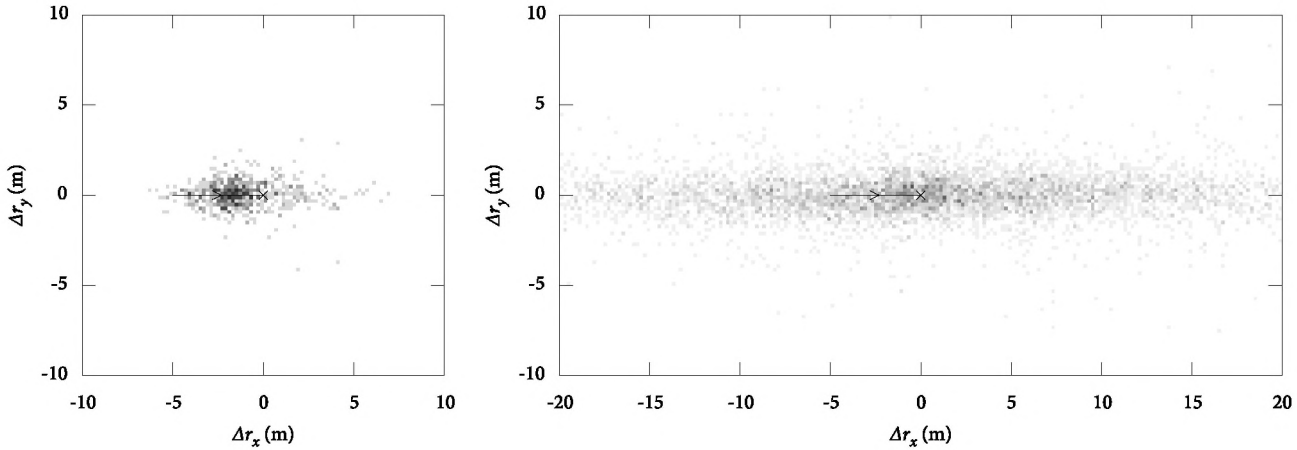

FIG. 5.6 · Density plot for ~ 700 showers of various species and energies $E > 10^{17}$ eV of simulated values for the impact location of the shower as reconstructed by the method outlined in the text. The actual position of the core is marked with a cross. Also shown is the arrival direction for slanted air showers (solid line). The left panel shows the theoretical limit in reconstruction accuracy. On the right realistic observational errors were introduced in (5.7). The colour intensity scales linearly with the number of reconstructions at that point.

5.5 · DETERMINING SHOWER CORE POSITION

If an estimate for $X_{\max}$ (and therefore for R) is available, we can employ (5.4) in an alternative way to estimate values for the distance r of the observer to the shower axis, by writing

$$r = R_1^{1+1/\alpha\beta-1/\alpha} \frac{t^{1/\alpha}}{(R+R_0)^{1/\alpha\beta}}. \tag{5.7}$$

In an actual experimental setting, the dependencies of α, β, and R_1 on δ need to be taken into account, for example through an iterative fitting procedure for r and δ. For the sake of simplicity, we will only reconstruct the distance to each antenna here, and we will assume the general direction of the core impact position to be known. This decision is motivated by the fact that the effect on the value of r caused by variations in δ is generally small.

In the theoretical limit, the distribution of reconstructed shower core positions using this method is shown in the left panel of Fig. 5.6. The colouring in this plot shows the amount of reconstructions at a certain position relative to the actual core impact location. The true position is at the origin, indicated by a cross. The arrival direction of inclined showers is always from the left, as indicated by the arrow. Note that the elongated structure of the reconstruction distribution is not a projection effect from inclined showers: we have already compensated for this by the transformation to the shower plane through (5.1). Instead, the feature is a systematic error intrinsic to the reconstruction algorithm. For a shower incident from the south, for example, the parameterized form is not symmetric in the north-south direction, but it is in the east-west direction. This effect is also responsible for the slight offset of nearly −2 m in the $\hat{x}$ direction.

Theoretically, the systematic offset could be reduced and possibly even removed entirely by refining the parameterization in (5.4) and (5.5). There is little gain in this exercise, however, when a more realistic reconstruction estimate is made. This is clarified in the right panel of Fig. 5.6, where again some error sources were introduced. The error in the arrival direction is again 1.0°, and a Gaussian uncertainty of 20 g/cm^2 in the value of the shower maximum is assumed, corresponding to a typical error in R of 200–250 m. Clearly, the offset mentioned earlier is entirely swamped by the deviations induced by the uncertainties. The substantial difference in reconstruction accuracy between the $\hat{x}$ and $\hat{y}$ direction results directly from the uncertainty imposed on θ_0: even a small deviation of the zenith angle will make a noticeable difference in the obtained value for t from (5.2).

Similar to the determination of $X_{\max}$, the average error increases drastically when the radius of the array is smaller than 500 m. The error does not increase significantly, however, when the minimum distance is set to 300 m. This is slightly counterintuitive, but it is again related to the accurate probing of the shower front shape. Of course, the requirement remains that the arrival delay at the impact location is known to 10 ns or so.

5.6 · DISCUSSION

The analysis in this work on the relative delays of geosynchrotron emission from extensive air showers was performed on the raw, unfiltered pulse shape. In real experiments, however, the antennas used are bandwidth-limited, which will be reflected in the shape of the measured pulse. The effect on the arrival time of the pulse is negligible for close antennas ($r < 300$ m), but for remote antennas it will become important, as the pulse is much broader in these regions. In particular, this may be troublesome for antennas which clip frequencies below ~ 40 MHz.

Another effect that has not been investigated is that of the observer's altitude: in our simulations, this height was fixed at 100 m above sea level. We do not anticipate a significant change of the parameterization or its parameters, however. This can be inferred from the fact that the description is valid independent of zenith angle. Changing this angle is comparable to varying the observer's altitude.

Though a deviation from a planar wave is indeed observed in LOPES measurements (Falcke et al., 2005), at only 200 m the array is too small to benefit from the theoretical knowledge of the shape of the radio pulse front. There are currently two other experiments under construction, however, that could make use of the technique outlined in this work. One of these is the initiative in which radio antennas inside the Pierre Auger observatory (Abraham et al., 2004) will be erected (Van den Berg & et al., 2007). Such an array could use the method in Sect. 5.5 to increase the accuracy of the estimated core impact position, since its reconstruction error for the surface detectors is in excess of 100 m. A precise estimate for $X_{\max}$ would have to be provided by the fluorescence detectors. The planned spacing of radio antennas is > 500 m, which would allow an accuracy in the reconstruction of around 30 m if the core lies within the radio array.

Another possible experiment is the LOFAR telescope (Falcke et al., 2006), which consists of a dense core of approximately 2 km in diameter, with groups of 48 radio antennas every few hundred meters. Its size and spacing make this setup ideally suited to determine $X_{\max}$ using the method outlined in Sect. 5.4. At present, no hybrid detection method is available for LOFAR, however, so the shower core position has to be determined too by radio methods, making the estimates and their errors dependent on one another.

5.7 · CONCLUSION

Through detailed simulations of air showers and their geosynchrotron radio emission, we have derived an empirical relation between the relative delay of the radio pulse emitted by the air shower front and the atmospheric depth of the shower maximum. By analysis of the radio pulse arrival delays in radio antennas in an array of low-frequency radio antennas, this relation can be used to estimate the depth-of-maximum if the impact position is known or vice versa.

We have confirmed that both methods work in principle, with no information other than radio signal delays used in the reconstruction. When the algorithm is tested

under realistic conditions, however, the accuracy of the method is reduced. In the case of determining the shower maximum, reconstruction down to a useful confidence level is possible only for shower maxima up to ~ 7 km away, and only if the shower core impact position is known down to a few meters. When the parameterization is used to derive this position, the critical quantity is the accuracy in the zenith angle of the shower, which needs to be significantly less than a degree to reconstruct the shower impact location to an accuracy of 10 m at high inclinations up to 60°.

ACKNOWLEDGEMENTS

This work is part of the research programme of the 'Stichting voor Fundamenteel Onderzoek der Materie (FOM)', which is financially supported by the 'Nederlandse Organisatie voor Wetenschappelijk Onderzoek (NWO)'.

6 · *A very-high-energy cosmic-ray trigger for the LOFAR telescope*

The LOFAR array, an unconventional new radio telescope under construction in the northern part of the Netherlands, may provide an important addition to the study of cosmic particles through the radio signal of extensive air showers. Since there is no external means of triggering the radio antennas in LOFAR, we present here the requirements for a radio-only trigger of the array based on the characteristics of radio pulses from air showers. We also provide a basic implementation of the set of algorithms that together form this trigger based on the hardware design for LOFAR that is currently envisaged. This work is intended to be usable as the basis on which the LOFAR engineering team can implement the trigger on the actual hardware.

6.1 · INTRODUCTION

A new radio telescope is being constructed in the Northern part of the Netherlands (Falcke et al., 2006). When completed, this telescope called LOFAR or *Low Frequency Array* will be the most sensitive and most versatile radio telescope in existence. Its strength lies in its unconventional design, using simple omnidirectional dipole antennas rather than large dishes to collect radio waves. Combining the signals of all antennas is done using software rather than hardware, making the entire telescope incredibly flexible compared to conventional radio dishes, as no moving parts are involved in the design of the telescope. Currently, LOFAR development is in its final test phase: the first antennas are in the field, and first serious scientific observations are expected to take place early 2009.

One of the key scientific goals of the the LOFAR project is to detect radio pulses produced by cosmic-ray particles. The detection of these signals can be divided observationally and technically in three cases, which are designated *high-energy mode*, *very-high-energy mode*, and *ultra-high-energy mode*. This work is concerned with the very-high-energy mode, which aims to detect atmospheric extensive air showers induced by cosmic particles above a certain energy. The lower limit of this energy is set by the requirement that the produced radio signal is strong enough to be detected by single LOFAR dipoles, without the need for beam-forming or sophisticated spectral cleaning preceding a trigger.

Air shower measurements are different from most other LOFAR observations: they cannot be observed through long, continuous integrated measurements. Instead, they occur in short, random events. These events can be obtained by using an external trigger such as an array of particle detectors, as is the case in the LOPES experiment (Falcke et al., 2005; Horneffer, 2006). Alternatively, there is the possibility of designing a trigger sensitive to radio pulses of air showers. This approach has the advantage that the LOFAR array can be used as-is, with no additional hardware needed. Considerations for such a trigger are described here.

Ideally, the algorithm triggers on all atmospheric air showers within a certain parameter range and does not trigger on other phenomena. This parameter range can be limited in terms of primary particle energy, arrival direction, and core impact location

on the ground. If no parameter range can be found in which there is full trigger efficiency, this limits the possibility of performing certain scientific analyses such as integral flux measurements, as the final event rate may depend on unknown parameters. Falsely triggered events are less problematic because they can be rejected afterwards, but they do increase the load on data transmission and storage systems.

6.2 · OVERVIEW

Radio pulses from extensive air showers are distinctly different from other cosmic radio signals. Some of the properties that set them apart are:

- **Random occurrence** — Cosmic particles arrive from random directions on the sky and at random times. This means that any trigger should aim to watch as much of the sky for as large a fraction of time as possible.
- **Very short time scales** — Extensive air showers are very short-lived. Consequently, the emitted radio pulse generally lasts less than 50 ns. In an experimental environment, including the LOFAR telescope, the shape of the recorded pulse is given by the impulse response of the electronics rather than the width of the raw pulse.
- **Limited area** — An air shower illuminates a patch on the ground through geosynchrotron radiation that is similar in size to its particle footprint, typically in the order of a few hundred meters at a primary energy of 10^{18} eV (see Fig. 6.4 on page 100).
- **Curved pulse front** — Since extensive air showers are produced in our own atmosphere, typically at distances of < 20 km, the radio pulse front shape is curved. The usual assumption of a plane wave front as would apply to a source at infinite distance is no longer valid. Though a spherical shell is a good first-order approximation, the actual shape is more complicated (cf. Lafebre et al., 2008c).
- **Polarised signal** — Geosynchrotron theory (Huege & Falcke, 2003) predicts that radio pulses have strong linear polarisation.

Except for their random occurrence, these pulse properties may be incorporated in the decision process to distinguish an actual air shower from other phenomena.

The LOFAR telescope consists of high-band and low-band antennas, with respective intrinsic frequency filters of 10–80 MHz and 110–230 MHz. The low-band antennas, which are of most interest in cosmic-ray air shower research, are placed in stations of 48 antennas. Each low-band antenna station has a diameter of ~ 100 m. These stations will be scattered all over the north of the Netherlands, except for a group of close stations in the center, which is called the *compact core*. Fig. 6.1 shows an overview of the proposed placement of stations in this core.

An air shower's radio footprint size is larger than the size of a station, but it is typically smaller than the distance between stations, except in the center of telescope. This means that usually only one remote station is illuminated by a single shower. Thus,

FIG. 6.1 · Overview of the station locations in LOFAR's compact core. Each station of 48 low-band antennas is indicated by a solid circle. Current funding allows construction of about half of these stations. (Drawing courtesy of Astron.)

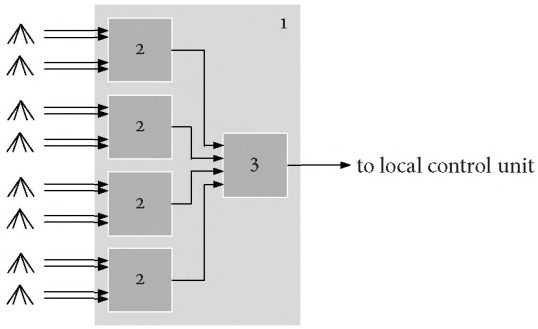

FIG. 6.2 · Schematic view of the transient buffer board (1). Eight antennas, with two dipoles each, are connected to four memory trigger controllers (2). Their output is monitored by a transient buffer board controller (3).

every station should have its own, independent trigger. In the compact core, several stations may see the same event. For big events and smaller events in the core region LOFAR's central processor should forward triggers to other stations as well.

Taking into account these considerations, the LOFAR hardware design suggests to split the trigger into three levels as follows, in order to minimise processing and network load:

- **Monitoring single dipole data streams** — Each dipole's data stream is filtered and monitored for the occurrence of short pulses. Detected triggers are forwarded to the station's central computer.
- **Combining single antenna triggers** — Centralised in each station, the single antenna triggers are subjected to some checks. If they compose a valid trigger pattern, a station trigger is generated. This results in freezing and dumping the memory buffers of all antennas. This trigger is also forwarded to LOFAR's central processor.
- **Analyzing and combining station triggers** — At the central computing facility, all events are analyzed. Depending on the event size, a decision may be made to forward the trigger to other core and remote stations.

At each level, the trigger is implemented in software or firmware at some point in the LOFAR system. The levels themselves are again separated into different steps. In the following sections, we describe in some detail the possible and desirable tasks to be carried out in the triggering process.

6.3 · MONITORING SINGLE DIPOLE DATA STREAMS

The LOFAR design groups antennas into stations of 48 antennas. In every station, sets of eight antennas (with two polarization channels each) are connected to one dedicated piece of hardware called *transient buffer board*, a schematic view of which is shown in Fig. 6.2.

The first level of the trigger will be implemented on these boards. Each transient buffer board consists of memory banks to keep up to a second of raw time data in memory at all times. It also has limited computational power in the form of field-programmable gate arrays, which allow one to load different software onto the board even after it is employed. Each transient buffer board contains four *memory trigger controllers*, connected to four dipoles each. Most of the algorithm outlined in this section will run on these controllers. The computational power of the memory trigger controllers is rather limited, but it is possible to sacrifice up to three monitored channels per controller, extending the possible complexity of the algorithm by a factor of four.

To reduce effective noise in the triggering process, all data streams should be filtered. Broadly speaking, the signals interfering with correct recognition of geosynchrotron pulses can be categorized into two groups: short pulses and narrow-band transmissions.

Usually, unintentional man-made transmissions, such as signals from electronics or spark plugs, produce radio pulses that are relatively short in time and therefore broad in frequency. These sparks are always low in power, and consequently they are only detectable close to the source. Despite the designation 'short', most of these pulses are still much longer than radio pulses form extensive air showers. Pulsed interference may result in false single antenna triggers, increasing the rate of false coincidences. This effect can be mitigated in different ways. First of all, the trigger algorithm could take the pulse shape into account, ignoring pulses longer than 100 ns or so. Secondly, coincidence checks should only pass if the radiation source does not lie inside the array. On a higher level, the shape and structure of the footprint could also be analyzed. We will elaborate on the second method in Sect. 6.4.

An entirely different class of interference comprises most intentional man-made transmissions such as radio and TV station broadcasts. In contrast to sources of sparks, these are continuous on air shower time scales. In general, this interference is also narrow in bandwidth. The effect of this type of interference is an overall increase of the effective noise level, preventing detection of weak pulses. The most thorough way of filtering narrow-band interference is to transform the data to frequency domain by a Fourier transformation. One would then remove the interference, easily identifiable in frequency space as narrow spikes, and transform back to time domain.

Unfortunately, the amount of computing resources needed to perform these steps are beyond the capacity of the field programmable gate arrays used on the LOFAR hardware, if the analysis is to be done in real time. As a workaround, one could make use of time-domain based filtering of the data. In these filters the value of an output sample depends on the previous values of raw and filtered samples in the following manner:

$$x'_i = \sum_{j=0}^{n_P} b_j x_{i-j} - \sum_{j=1}^{n_Q} a_j x'_{i-j}, \tag{6.1}$$

where x'_i represent the filtered output samples, x_i are the unfiltered input samples, and n_P

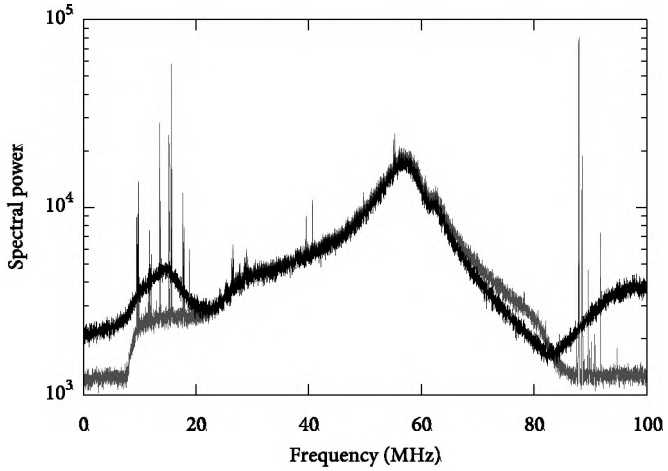

FIG. 6.3 · Effect of a time-domain based band-rejection filter on the background power spectrum at the LOFAR location. Two filters of 2 MHz width were applied, at 15 MHz and 88 MHz. The lighter background spectrum is the original spectrum, the dark spectrum on top is the filtered residual.

and n_Q are the feedforward and feedback filter orders, respectively. A filter with $a_j = 0$ is called a *finite impulse response filter*; if it has both $a_j \neq 0$ and $b_j \neq 0$, it is called an *infinite impulse response filter*. These names derive from the theoretical possibility of an infinite impulse response filter to return an infinite answer to a short impulse, while a finite filter cannot.

The effect of an impulse response filter depends on the parameters $\boldsymbol{b} = (b_0, b_1, \ldots)$ and $\boldsymbol{a} = (a_1, a_2, \ldots)$. An example of a time-domain band-rejection filter is

$$\begin{aligned} \boldsymbol{b} &= (1, -2\cos 2\pi\nu, 1), \\ \boldsymbol{a} &= (1+\alpha, -2\cos 2\pi\nu, 1-\alpha), \quad \text{where } \alpha = \frac{\Delta\nu}{\nu}\pi \sin 2\pi\nu. \end{aligned} \tag{6.2}$$

The frequency ν is the noise peak to be filtered out, and $\Delta\nu$ is the width of the filter. In the equations given here, both are expressed in samples^{-1}, corresponding to 200 MHz in the case of LOFAR. The central frequency and suppression width of the filter depend on the strongest interference sources in the area such as radio or TV transmitters. As these conditions may vary both with time and location, the filter values should be adjustable in the field to suit local needs.

Inserting several notch filters at the frequencies of the strongest interference sources will lower the effective noise level in the data, increasing the sensitivity of the triggering algorithm. This is illustrated in Fig. 6.3. This plot shows the power

spectrum of the background noise level at the location of the LOFAR compact core. Overlaid is the same spectrum when two notch filters are applied near the highest narrow-band interference peaks, at 15 MHz and 88 MHz, respectively, with a bandwidth of 2 MHz. Part of the power of the original peak flows into the surrounding frequency bins. Note that the power is displayed in logarithmic units: the power of the interference peaks is reduced by about an order of magnitude. As mentioned earlier, a filter in frequency space would be able to remove the narrow peak without affecting other frequencies.

Once filtered, the data stream should be monitored by the memory trigger controllers for signals indicating a cosmic-ray air shower. In most cases, this signal will be recognisable as a short, sharp pulse of ~ 20 ns wide. Because this duration is of the order of the sampling frequency of the antennas, the pulse shape will resemble the impulse response function of the analog electronics rather than the natural shape of a radio synchrotron pulse. In order to detect these pulses, the filtered data stream should be analyzed according to the algorithm

$$x_i^2 > \mu_i^2 + k^2 \sigma_i^2, \tag{6.3}$$

where x_i is sample i of the received signal, and μ_i is the time average of the absolute signal running over a time interval containing n samples. The other term contains the standard deviation σ_i over the same block and a threshold factor k. We may simplify this equation at the cost of some precision by using the absolute value $|x_i|$ instead of x_i^2. Since correct determination of the standard deviation requires the calculation-intensive square root operator, the inequality can be made less calculation-intensive by implementing

$$(|x_i| - \mu_i)^2 > k^2 \sigma_i^2. \tag{6.4}$$

If the interference is Gaussian, μ_i^2 will be proportional to σ_i^2. This means we may replace the equation above with the much simpler form

$$|x_i| > k\mu_i, \tag{6.5}$$

without loss of accuracy. The values of n and k should be adjustable after deployment of the array as our insight of efficiency rates progresses. A useful range for n is around 50 to 200 samples, and an ideal value for k is expected to lie in the range of 5 to 8.

Because μ_i is used in identifying interesting events rather than in the actual analysis, its value does not have to be exact. This opens the door to using faster algorithms at the cost of precision. A simplified implementation recalculates μ_i only once per block of n samples instead of every sample. Further performance improvements can be made by requiring that n is a power of 2, allowing one to replace the divisions with bit-shift operations (e.g. $\gg m$ to perform a division by $n = 2^m$) but discarding the fractional part of the quotient.

Alternatively, an approximation of the running average could be used to save memory, by defining

$$n\mu_i = (n-1)\mu_{i-1} + |x_i'|, \tag{6.6}$$

where μ_{i-1} is the average and standard deviation calculated for the previous sample. Advantages of this algorithm are that the running average will be smoother and that it does not require all n samples to be directly accessible from memory. This permits the use of much larger values for n, allowing one to use the same algorithm to look for a much slower increase of the total power, for example to trigger on lightning. This algorithm is more calculation-intensive, on the other hand, consuming more of the limited amount available.

When a certain number of samples satisfies (6.5), a trigger message is dispatched to the local control unit. If there are some samples below the threshold, followed by one or more samples above it, all of these samples should be considered one event. This is taken care of by a counter, which is incremented by 4 (with a maximum of 15) each time a sample lies above the threshold, and it is decremented by 1 for each sample below the threshold. As soon as the counter reaches a certain threshold value, an antenna trigger signal is generated. If the number of samples below the threshold reaches a certain value (< 16), the trigger status is reset, after which a new trigger can be generated. Ideally, there is no dead-time after the generation of a trigger, since this will change the efficiency of the array, affecting the scientific analysis as a whole.

A trigger message from the transient buffer board to the local control unit contains which dipole generated it; the time when the trigger occurred, e.g. the sample number of the first sample above the threshold; the width of the pulse, e.g. the number of samples between the first and last sample within the trigger window; the height of the highest sample within the trigger window; the sum of the pulse heights within the trigger window; and the value of the mean before the trigger occurred.

6.4 · COMBINING SINGLE ANTENNA TRIGGERS

All transient buffer boards connect to the station's *local control unit*, a complete PC with more computational power available. Triggers from all antennas will be merged here, and based on the combined proporties a decision will be made whether or not to store the raw data from the antennas.

As a first step, the local control unit should check the widths of the incoming pulses to discriminate between the ultra-short radio pulses from air showers and longer man-made sparks. The maximum width should be of the order of 100 ns.

Subsequently, allowed pulses are combined to check for coincidences. The local control unit should sort triggers from all transient buffer boards by time. When a minimum number of antenna triggers occur within a certain time window, a coincidence is said to be found. The width of the time window is determined by the extent of the station: it should be slightly more than the light travel time across the entire station to

allow for errors in the determining the time stamps. A useful range for the minimum number of antennas to form a coincidence depends on the size and layout of the station as well as the total number of antennas in it. Its value will have to be defined at a later stage, when the trigger can be tested in the field.

After a coincidence trigger is found, there are several possibile ways of continuing the analysis. In the simplest scenario, the trigger is accepted as-is. More intelligent scenarios include incorporating information about the source of the pulse in some way. This is done through analysis of the arrival time delays in the different antennas.

Three levels of direction finding are identified here. The first and simplest option is to fit a plane wave to the incoming signal. One implementation of this test derives a direction analytically for each set of three antennas. These values are then averaged, weighting them according to the distance between the antennas used in the reconstruction. Other implementations employ a minimalisation algorithm such as a least-squares method, which can be performed either analytically or iteratively, whichever is more accurate or computationally less intensive.

A more complicated scheme would include fitting to a spherical shell, and requiring that a source position can be determined before a station level trigger is issued. Alternatively, a realistic shower front shape such as derived in Lafebre et al. (2008c) could be fitted, which would at the same time produce an estimate for the depth of the shower maximum, though this level of reconstruction is probably better left to be performed in off-line analysis. These reconstruction algorithms can again be implemented using a least-squares algorithm, or an analytical solution can be found using four instead of three antennas, since there is an extra degree of freedom to be taken into account.

Preferably, any of the calculations mentioned above should be carried out with antennas that are as far away from each other as possible, since this increases the direction and position reconstruction accuracy. The reconstruction performance of fitting a spherical or realistic shower front shape should be evaluated after a period of observation time, since the reconstruction will not be very accurate if the maximum distance between the antennas is less than a few hundred meters or so (Lafebre et al., 2008c). Given the fairly limited baselines of 100 m in a LOFAR remote station, fitting a simple plane wave is probably to be preferred there. In the compact core, however, a more complicated method could be applied in reconstruction of single-dipole events at the central processor as explained in the next section.

If the antenna trigger times do not conform to a signal from a certain direction, or if the signal originates from a point on the horizon or close to the station, the trigger should be rejected. Additionally, the decision could include an analysis of the spatial profile of the pulse strength. The illuminated patch on the ground should be elliptical in shape. A simple check could examine whether there are antennas well above the detection threshold close to working antennas that did not trigger on the event. This

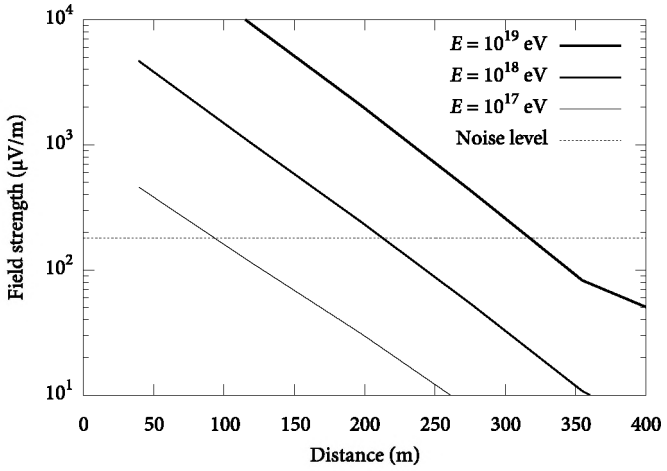

FIG. 6.4 · Expected maximum field strength produced by vertical proton showers of various energies E (see legend) in the east-west direction through a rectangular filter at 30–80 MHz. The dotted line represents the level of a power signal-to-noise ratio of 10 given the background noise in a rural area.

would be a sign of a localised event very close to one of the antennas.

A more complicated scheme would incorporate the slope of the pulse height. Inside the elliptical footprint the field strength decreases steeply with distance from the shower axis. Emission from air showers decreases exponentially ($\propto e^{-ar}$) in field strength with distance r from the shower impact position. This is illustrated in Fig. 6.4. This plot shows the expected total electric field strength for a proton shower incident from the zenith as it would be seen by an antenna directly to the east or west from the shower impact position when run through a rectangular filter of 30–80 MHz. Also shown is the expected threshold for a signal-to-noise ratio of 10, assuming a rural environment such as the position of the LOFAR compact core. This threshold corresponds to a value of 180 μV/m.

The signal strength of nearby, human-made sparks occurring within the array, on the other hand, is proportional to r^{-2}. By analyzing the dependence of the signal strength with distance, one could distinguish between the case of an air shower-induced signal and an artificial pulse. If the footprint either does not match the shape expected from an air shower, or if it does match the shape expected from interference, the trigger should be rejected. At this point, it remains unclear whether the quality of trigger messages as derived from the raw time data is sufficient for this kind of analysis.

Further rejection may be possible by analyzing the polarisation of the signal. Geosynchrotron emission from air showers is expected to be exhibit strong linear polari-

sation, producing a signal in only one direction. Because the A-shaped dipoles in LOFAR's low band antennas induce cross-talk between the different pure polarisation channels for inclined showers, analysis of this kind can only be performed for near-vertical showers. Special care should be given to events during stormy and to a lesser extent also snowy weather, because the pulses may be strongly amplified in these cases (Buitink et al., 2007).

A factor limiting the complexity of the trigger algorithm is that the transient buffer boards have to be notified to transfer their data while it is still in the buffer. Therefore, the time between the raw signal arriving from the dipoles and the data request arriving from the local control unit has to be less than the buffer size, which is 1 s in the current board design. Additionally, the trigger algorithm should not interfere with regular functioning of the local control unit, as beam-forming and analysis tasks from other observations are being carried out at the same time as well.

After the decision for a trigger is made, the local control unit sends a short trigger message to the central processor, allowing possible follow-up data requests to other stations. This message should contain at least which station it came from; the time the event occurred, e.g. the trigger time of the first antenna or that of the antenna closest to the impact location; a value indicating the size of the air shower, e.g. the number of triggered antennas or preferably a value derived from all single antenna pulse heights such as the maximum or sum of the pulse heights. If a successful determination of the arrival direction of the air shower could be made, this should also be included.

After it has sent this trigger message to the central processor, the local control unit signals all transient buffer boards, including the boards that did not produce a trigger and those not set to participate in the triggering process at all. On the transient buffer board, this signal causes further data acquisition to freeze and the relevant portion of the raw time series in every buffer to be sent back to the central processor. Note that the data to be transferred is the raw data, not the data to which the narrow-band filters as explained in the previous section was applied. The amount of data to be transferred should be of the order of a millisecond per antenna, corresponding to $\sim 2^{17}$ data samples at 200 MHz sampling. If the amount of data is significantly larger, more time is lost transferring the data, increasing dead time in the transient buffer boards. If the amount is considerably smaller, the frequency resolution of the Fourier transform performed in off-line data analysis decreases. It may also complicate correlating data from different stations if the overlapping time window is insufficiently long.

Each dipole's raw data from the transient buffer boards is sent to the LOFAR central processor. A small header with some statistical information concerning the event accompanies the raw data, consisting of the same information that was sent before the raw data was transferred to the local control unit. All in all, the total amount of data to be transferred to the central processor amounts to approximately 25 MB per station only. Since data taking is neither continuous nor extensive, these transfers may be performed without disturbing data acquisition for other, astronomical observations running at the same time.

For stations in the compact core, a useful extension would be to send additional messages to the central processor when a coincidence has been detected that was not large enough to produce a trigger, but could still produce a trigger when combined with other core stations. In this case, trigger messages from all dipoles should be transferred instead of the station trigger message only.

6.5 · ANALYZING AND COMBINING STATION TRIGGERS

LOFAR's central processor has two main functions in the search for very-high-energy cosmic rays. Firstly, it should forward a trigger when an air shower pulse is expected to be found in one or more stations in LOFAR's compact core but not all stations have detected it. Secondly, the central processor should trigger additional stations when an unusual or special event has been recognised, extending the amount of information available to reconstruct and analyze the occurrence.

The first task only applies to stations in the compact core. From Figs. 6.1 and 6.4, it is observed that for large showers the average distance between stations is less than the typical footprint size of the air shower. Therefore, it is worthwhile to obtain signals from surrounding stations. This task could be implemented in two ways. The first approach applies if the core stations' local control units are set up to forward individual dipole triggers to the central processor, for example when a coincidence was detected that was not large enough for a full station level trigger. In this case, messages can be combined in a similar way to the algorithm used on each station's local control unit, but including data values from all stations involved. In the second approach, neighbouring stations to a core station that produced a trigger are asked to transfer each dipole's data.

The second function concerns all LOFAR stations. For the in-depth analysis of special events, additional data from more or even all stations may be desirable. Currently, special events include two cases: extremely strong events and coincidences between events. The first kind occurs when several neighbouring stations report a trigger at the same time or when a station reports a cosmic-ray event with very strong pulses. The second case is when two or more stations that are more than a few hundred meters apart report an internal trigger within a short time window and possibly from the same direction or source position. Such events may be induced by cosmic particles breaking up before entering Earth's atmosphere (see Lafebre et al., 2008b).

Since the cosmic-ray project constitutes only part of LOFAR science, the possible extent of analysis at the central processor highly depends on the requirements of other observations running in parallel. Parameters such as the number of antennas to be triggered on or signal strength threshold values may be tuned to more sensitive values during dedicated cosmic-ray observations, resulting in more triggers and, consequently, a higher data transfer load. In parallel mode, running next to other observations, these algorithms could be adapted to be less sensitive or even switched off completely. At any

rate, exact parameters for the central processor's algorithms will have to be decided on at a later stage, when the performance of the lower-level triggers can be evaluated and taken into account.

6.6 · EVENT RATES

The LOFAR design is optimised for traditional astronomical research in which the radiation from a distant source is measured directly rather than for applications in astroparticle physics. This is reflected in the antenna layout: it favours variation in baselines rather than maximising detection surface. While this kind of setup does allow one to make detailed studies of the shape of the shower front (see Chapter 5), it seriously diminishes cosmic-ray detection rates at very high energies over 10^{17} eV. Let us make an estimate for the yearly amount of events we expect to see with the LOFAR telescope as it is currently planned.

Assuming a total of 40 stations and full sensitivity up to zenith angles of 80° (Petrovic et al., 2007), the total aperture for very-high-energy cosmic-ray research with LOFAR is

$$A = 40 \cdot 0.05^2 \pi \cdot (1 - \cos 80°) \approx 0.26\,\mathrm{km}^2\,\mathrm{sr}, \tag{6.7}$$

To estimate the expected rate of events, let us assume an integral cosmic-ray spectrum of

$$\Phi(E) = \left(\frac{10^{18}\,\mathrm{eV}}{E}\right)^2 \cdot 47\,\mathrm{km}^{-2}\,\mathrm{yr}^{-1}\,\mathrm{sr}^{-1}. \tag{6.8}$$

With an optimistic cutoff of $E_0 = 10^{17}$ eV taken from Falcke et al. (2005), we expect to see an event rate of

$$R = A\Phi(10^{17}\,\mathrm{eV}) = 1.2 \cdot 10^3\,\mathrm{yr}^{-1}. \tag{6.9}$$

This corresponds to roughly 30 real events per station per year. This figure emphasizes at the same time the insignificance of the amount of data to be transferred through LOFAR and the need for a sophisticated trigger to discard unwanted events.

6.7 · CONCLUSION

We have described the requirements to successfully employ the LOFAR array, a new radio telescope under construction, as an observatory for cosmic-ray air showers in the energy range 10^{17}–10^{19} eV. We have supplied basic implementations of the desired trigger algorithms to perform independent radio measurements, divided in three steps: the monitoring of single dipoles, combining these per LOFAR station, and processing at LOFAR's central processor. This work can be used as a guide for the LOFAR engineering team for the implementation of the trigger on the actual hardware.

Due to delays in employing prototypes of the transient buffer board, the effectiveness of the method described could not be tested in the field, unfortunately. In fine-tuning the algorithm, one will have to rely on the possibility to test and, if necessary, replace the trigger software at a later stage.

7 · *Prospects for direct cosmic-ray mass measurements through the Gerasimova-Zatsepin effect*

S. Lafebre, H. Falcke, J. Hörandel, J. Kuijpers

This chapter is an expanded version of Lafebre et al. (2008b)

The Solar radiation field may break ultra-high-energy cosmic nuclei apart, after which both remnants will be deflected in the interplanetary magnetic field in different ways. This process is known as the *Gerasimova-Zatsepin effect* after its discoverers. We investigate the possibility of using the detection of the separated air showers produced by a pair of remnant particles as a way to identify the species of the original cosmic-ray primary directly. Event rates for current and proposed detectors are estimated, and requirements are defined for ideal detectors of this phenomenon. Detailed computational models of the disintegration and deflection processes for a wide range of cosmic-ray primaries in the energy range of 10^{16} to 10^{20} eV were combined with sophisticated detector models to calculate realistic detection rates. The fraction of Gerasimova-Zatsepin events is found to be approximately 10^{-5} of the cosmic-ray flux, implying an intrinsic event rate of around 0.07 $\mathrm{km^{-2}\ sr^{-1}\ yr^{-1}}$ in the defined energy range. Event rates in any real experiment, whether existing or under construction, will probably not exceed $10^{-2}\ \mathrm{yr^{-1}}$.

7.1 · INTRODUCTION

The mass composition of very-high-energy cosmic rays provides useful information on their acceleration mechanisms, because it is related to the compositions of their sources. When doing indirect measurements, as is the only realistic way to go about detecting high-energy cosmic rays, determining the composition of primary cosmic rays is not easy. Usually, it is only possible to make statistical, model-dependent estimates of the primary particle types of an ensemble of showers. Primary compositions are then derived from the abundances of different species components in the air showers considered (see e.g. Antoni et al., 2002). This difficulty arises from the fact that an air shower is an inherently unpredictable event: incoming primaries with identical parameters may produce different air showers and two similar air showers may be the result of different primaries.

An alternative mass determination makes use of the *Gerasimova-Zatsepin* effect. In this scenario, one relies on the fact that the heavier ultra-high-energy cosmic-ray particles, compound particles such as iron nuclei, have a chance of undergoing photodisintegration in the Lorentz boosted Solar radiation field before arriving at Earth, splitting the nucleus into two parts. Due to the charge difference of these two fragments, the deflection in the interplanetary magnetic field will be different, resulting in two separate air showers with some spatial separation, but arriving essentially at the same time and from the same direction. Given the discreteness of the masses of the remnants and the linear proportionality between a remnant's mass and its energy (assuming single-nucleon emission), the mass number A of the original disintegrated particle can simply be determined by estimating the energies of the primaries of the two showers:

$$A = \frac{E_1 + E_2}{E_1}, \tag{7.1}$$

where E_1 is the energy of the less energetic shower (Epele et al., 1999). To our knowledge, no experimental detection of a Gerasimova-Zatsepin event has ever been reported.

The phenomenon was originally investigated by Zatsepin (1951) and Gerasimova & Zatsepin (1960). They made an error in calculating the separation of the two showers, however: they based their calculations on the distribution of momentum over the two remnants after their splitting, resulting in a shower separation in the order of

centimeters, far too little to be detected as two separate showers. Further detailed studies incorporating the effects of deflection were made only decades later by Medina-Tanco & Watson (1999) and Epele et al. (1999). This work extends their research to a wider variety of cosmic-ray species. Additionally, a sophisticated detector model is used to calculate realistic rates for Gerasimova-Zatsepin observations.

Three independent processes can be identified in the Gerasimova-Zatsepin scenario: (1) the disintegration of the compound cosmic-ray primary; (2) the deflection of the remnants; and (3) the detection of the remnants. We will discuss these processes separately below.

7.2 · DISINTEGRATION

The chances for a nucleus approaching the Solar System to undergo photodisintegration have been investigated previously by Gerasimova & Zatsepin (1960), Medina-Tanco & Watson (1999) and Epele et al. (1999); we have taken the same approach in calculating this probability.

The total photodisintegration probability η_Z for a cosmic nucleus of atom number Z can be calculated by integrating along its trajectory:

$$\eta_Z = 1 - \exp\left[-\int_0^\infty \frac{d\ell}{\lambda(\ell)}\right] \simeq \int_0^\infty \frac{d\ell}{\lambda(\ell)}, \tag{7.2}$$

where the approximation holds for $\eta_Z \ll 1$. The coordinate ℓ is measured along the path of the nucleus and λ is its mean free path length at that point. This path length against photodisintegration can be written as

$$\frac{1}{\lambda(\ell)} = 2\int_0^\infty \sigma_Z(\epsilon_N)\frac{dn(\ell,\epsilon)}{d\epsilon}\cos^2\left[\frac{\alpha(\ell)}{2}\right]d\epsilon, \tag{7.3}$$

where σ_Z is the cross section for photodisintegration, α is the angle between the propagation directions of photon and particle in the heliocentric frame and $dn/d\epsilon$ is the number density of photons with energy ϵ. This density is dominated by the Solar black body spectrum with a temperature of $T_\odot = 5778$ K. The energy ϵ_N is the Lorentz boosted energy of a photon as seen from within the cosmic ray's comoving frame:

$$\epsilon_N = \epsilon\left(\gamma + \sqrt{\gamma^2 - 1}\cos\alpha\right) \simeq 2\gamma\epsilon\cos^2\frac{\alpha}{2}, \tag{7.4}$$

where γ is the cosmic ray's Lorentz factor and ϵ is the Solar photon energy as observed in the heliocentric frame (Gerasimova & Zatsepin, 1960). In order for iron photodisintegration to occur, for example, ϵ_N should be $\gtrsim 15$ MeV. Given an energy of around 1 eV for an average photon in the Solar radiation field, this corresponds to a Lorentz factor for the iron nucleus of $\gamma \gtrsim 7.5 \cdot 10^6$ for head-on collisions, or to an energy of $4 \cdot 10^{17}$ eV. The photodisintegration cross section for iron peaks at $\epsilon_N = 25$ MeV, corresponding to an iron energy of $6.5 \cdot 10^{17}$ eV (cf. Fig. 7.3).

Different photodisintegration reactions are possible, with different reaction products. By far the most likely reactions to occur, however, are those in which one proton or neutron is knocked out of the nucleus, (γ, p) and (γ, n), respectively. Throughout the remainder of this paper, we have assumed such an interaction. The photodisintegration cross section $\sigma_Z(\epsilon)$ for single nucleon emission up to $\epsilon \lesssim 30$ MeV as a function of A was taken from Karakula & Tkaczyk (1993). This parameterization, describing the giant resonance peak, is defined as

$$\sigma_{GR}(\epsilon) = \frac{1.45A(\epsilon T)^2}{\left(\epsilon^2 - \epsilon_0^2\right)^2 + (\epsilon T)^2} \text{ mb} \qquad \epsilon \lesssim 30 \text{ MeV}, \tag{7.5}$$

where $T = 8$ MeV is the bandwidth of the resonance peak and ϵ_0 denotes the peak energy, satisfying $\epsilon_0 = 42.65A^{-0.21}$ whenever $A > 4$ and $\epsilon_0 = 0.925A^{2.433}$ otherwise. A constant cross section of $A/8$ mb is taken for $\epsilon > 30$ MeV whenever $\sigma_{GR} < A/8$ mb.

7.3 · DEFLECTION

After disintegration, the charged remnants will be deflected in the interplanetary magnetic field. Since the mass/charge ratio will generally be different for the two fragments of the disintegrated nucleus, so will the amount of deflection be.

To estimate the separation distance, let us consider one of the produced charged particles i in a homogeneous magnetic field B. Its gyroradius ρ_g may be written as

$$\rho_g = \frac{\gamma_i m_i c v_{i\perp}}{Z_i e B} = \frac{E_i}{Z_i e B \sin\beta}, \tag{7.6}$$

where c is the speed of light, e is the elementary charge, m_i is the particle's mass, $v_{i\perp}$ its velocity component perpendicular to the magnetic field, and β is the angle between the field and the particle trajectory. Given the huge gamma factors involved, it is evident that this radius is much bigger than the size of the Solar System even for unfavourable values of $E \sim 10^{16}$ eV and $B \sim 10^{-3}$ T. Ignoring the factor $\sin\beta$, the deflection distance d_i of the particle can now be approximated as

$$d_i \simeq \frac{R^2}{\rho_g} = \frac{Z_i e B R^2}{E_i} = \frac{A Z_i e B R^2}{E A_i}, \tag{7.7}$$

where R is the distance travelled by the particle. Hence, the final separation δ of the two particles will be equal to

$$\delta = |d_1 - d_2| = \frac{AeBR^2}{E}\left|\frac{Z_1}{A_1} - \frac{Z_2}{A_2}\right|. \tag{7.8}$$

Unfortunately, the shape and strength of the magnetic field surrounding the Sun is quite complicated. Akasofu et al. (1980) have constructed a three-dimensional model which consists of four components: (i) the Solar dipole; (ii) a large number of small spherical dipoles located along an equatorial circle just inside the Sun; (iii) the field

of the poloidal current system generated by the Solar unipolar induction; and (iv) the field of an extensive current disc around the Sun, lying in the ecliptic plane.

1. *The dipole component.* This is the main Solar dipole. Its contribution can be expressed in cylindrical coordinates as

$$\begin{aligned} B_\rho^{\text{dip}} &= -\frac{3B_s R_\odot^3}{2}\rho z\left(z^2+\rho^2\right)^{-5/2}, \\ B_z^{\text{dip}} &= -\frac{B_s R_\odot^3}{2}\left(2z^2-\rho^2\right)\left(z^2+\rho^2\right)^{-5/2}, \end{aligned} \tag{7.9}$$

   where the factor $(B_s R_\odot^3)/2$ is the Sun's magnetic dipole moment and B_s is 20 mT.

2. *The sunspot component.* A large number of small dipoles located along an equatorial circle just inside the Sun each contribute a field with a similar formulation as the previous component, but much smaller. Its expression is therefore similar to Eq. 7.9.

3. *The dynamo component.* This component arises from a current as a result of the rotation of the Sun in its dipole field. During an even Solar sunspot cycle, this current is flowing outward in the Solar equatorial plane. It is curving away from this plane, towards the poles, along the surface of the heliosphere at around $R_{\text{h}} = 20$ AU distance from the Sun. The current is directed back into the photosphere along the Sun's polar axis. During an odd sunspot cycle, the direction of this flow is reversed.[1] For the region $R_\odot < r < R_{\text{h}}$, We can express this contribution as

$$B_\phi^{\text{dyn}} = \pm B_{\phi 0}\frac{\rho_0}{\rho}, \tag{7.10}$$

   where $B_{\phi 0}$ is the magnitude of the field at distance ρ_0 from the Sun. The sign is given by the sign of z. For $\rho_0 = 1$ AU, $B_{\phi 0} = 3.5$ nT. The contributions in the $\hat{\rho}$ and $\hat{z}$ directions are both zero.

4. *The ring-current component.* This is the contribution of an extensive, thin current sheet around the Sun, lying in the ecliptic plane. The direction of this current is westward for even cycles and eastward for odd cycles. Its formulation is quite complex, but for the region of interest to us ($R_\odot \ll r < R_{\text{h}}$), it can be approximated as (Epele et al., 1999):

$$\begin{aligned} B_\rho^{\text{ring}} &= \pm B_{\rho 0}\rho_0^2\rho\left(z^2+\rho^2\right)^{-3/2}, \\ B_z &= -\mu_{\rho 0}\mu_0|z|\left(z^2+\rho^2\right), \end{aligned} \tag{7.11}$$

   where $B_{\rho 0} = 3.5$ nT at $\rho_0 = 1$ AU and the sign of B_ρ^{ring} is given by the sign of z.

[1] Currently, the Sun is entering an even cycle.

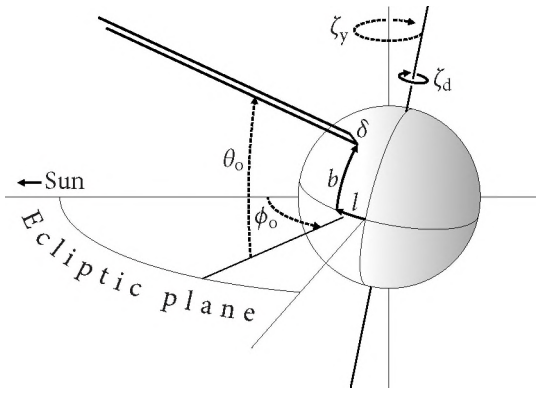

FIG. 7.1 · Schematic view of the Earth and the angles which together determine the angle of incidence in the detector frame. The angles b, l and ζ_d are fixed to to the Earth (solid arrows), while θ_o, ϕ_o and ζ_y are attached to the Solar reference frame (dashed arrows).

The influence on the deflection of cosmic particles will be dominated by the latter two components, as their contributions will be larger at greater distances. Due to the complexity of the field shape, our estimate in Eq. 7.8 does not hold. We can still use the proportionality, however:

$$\delta \propto \frac{AR^2}{E}\left|\frac{Z_1}{A_1} - \frac{Z_2}{A_2}\right|. \tag{7.12}$$

7.4 · DETECTION

Identifying a Gerasimova-Zatsepin pair as such requires both showers to be seen by a cosmic-ray detector. In order to calculate the Gerasimova-Zatsepin detection aperture for a given cosmic-ray detector, let us first define the separation resulting from different amounts of deflection of the two showers as the vector $\boldsymbol{\delta} = (\delta_\parallel, \delta_\perp)$ between the two remnants, projected on a plane perpendicular to the arrival direction in the Solar reference frame (ϕ_o, θ_o) and let $\delta_\parallel$ lie in the ecliptic plane. As stated earlier, cosmic particle gyroradii are very large compared to the size of the Solar System, allowing us to take both remnants' arrival directions equal to each other and to the original arrival direction.

For an accurate description of a detector's aperture, it is necessary to incorporate the angle at which the detector is hit by the cosmic-ray particles. The angles due to daily and yearly phase, ζ_d and ζ_y respectively, together with the latitude b and longitude l of the detector, fix the orientation of the detector as it is approached by the particles (see Fig. 7.1). The projection effects caused by these four angles give rise to an increase of the separation distance, affecting detection rates in a non-trivial way. Fig. 7.2 shows the average probability density distribution of this elongated separation $\boldsymbol{\delta}'$ in east-west and

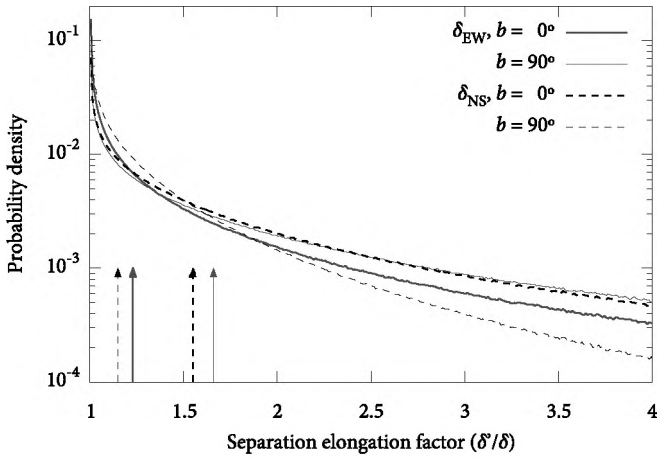

FIG. 7.2 · Probability density distribution for the elongated separation vector $\boldsymbol{\delta}' = (\delta_{EW}, \delta_{NS})$ in terms of the original separation vector $\boldsymbol{\delta}$ when compensating for projection effects due to the detector's position on Earth for a detector on the equator (thick lines) and at the pole (thin lines). The arrows represent the expectation value for each case.

north-south directions for a detector at the equator (b = 0°) and near the north pole (b = 90°), integrated over a year with cosmic particles arriving from random directions. Also drawn, as vertical arrows, are the expectation values for each case. As the elongation may easily exceed factors of 2, it is clear that projection effects cannot be neglected in our analysis.

Whether both air showers are actually detected, depends on the detector geometry as it is laid out on Earth, since the shower core location of both showers needs to be covered by the detector. Let us define a detector-specific function $\xi(\boldsymbol{\delta})$ which describes the probability of detecting the second shower event for a given separation vector $\boldsymbol{\delta}$, under the assumption that the first shower is detected. The average cross section or aperture A for a Gerasimova-Zatsepin event and a detector can now be calculated by integrating over ξ over the course of a year. We are also taking into account the detector's angular sensitivity ω as a function of the zenith angle θ as seen by the detector:

$$A(\boldsymbol{\delta}, E, \phi_o, \theta_o) = \frac{S_o}{\pi} \int_o^{2\pi} \int_o^{2\pi} \xi(\boldsymbol{\delta}')\omega(\theta, E)\, d\zeta_d\, d\zeta_y, \tag{7.13}$$

where S_o is the total area covered by the detector, and $0 \leq \omega \leq 1$. The factor $1/\pi$ serves to normalise to all sky visibility.

The absolute particle fluxes for various primary nuclei are estimated by the model presented by Hörandel (2003), which assumes

$$J_Z(E) = J_{0,Z}\left[\frac{E}{E_0}\right]^{\gamma_Z}\left[1+\left(\frac{E}{E_p Z}\right)^{\gamma_1}\right]^{-\gamma_2}. \tag{7.14}$$

$J_Z(E)$ are the contributions of a species Z in the cosmic-ray spectrum, $J_{0,Z}$ and γ_Z are constant factors for each species, $E_0 = 10^{12}$ eV, $E_p = 4.49 \cdot 10^{15}$ eV, $\gamma_1 = 1.9$ and $\gamma_2 = 1.1$. This parameterization is less accurate for very high energies as a result of a lack of statistics. Note that we will disregard the extragalactic contribution to the cosmic-ray particle flux in our analysis: this component is assumed to consist mainly of protons and helium nuclei (see Biermann, 1993). Protons will not contribute to the Gerasimova-Zatsepin flux at all, and helium cross sections are too low at the energies considered to be of consequence (see Fig. 7.3). The total hadronic cosmic-ray flux is

$$J(E) = \sum_Z J_Z(E), \tag{7.15}$$

where the summation runs over all cosmic-ray particle species, in our case $2 \leq Z \leq 92$.

Piecing all of this together, the final Gerasimova-Zatsepin event rate for a given detector for particles with energy greater than E is given by

$$\Phi_{GZ}(E) = \int_E^\infty \sum_Z J_Z(E')\left[\int \eta_Z(E', \phi_0, \theta_0) A(\boldsymbol{\delta}, E', \phi_0, \theta_0) \times f_{dc}(\phi_0, \theta_0)\cos\theta_0\, d\theta_0\, d\phi_0\right] dE', \tag{7.16}$$

where f_{dc} is the duty cycle of the detector, which is a constant factor in case of surface scintillators, but may depend on ϕ_0 and θ_0 for example for air fluorescence detectors, as they cannot observe during the day.

7.5 · RESULTS

To calculate realistic values for η_Z, a numerical model was constructed. Cosmic ray particles were injected into the Solar System from random directions on a trajectory towards Earth, and disintegrated according to Eq. 7.3. The integration in Eq. 7.2 was carried out to distances of 4 AU from the Sun: beyond this distance, the photon density is too low to have a significant effect on the disintegration probability. Calculations were carried out for primary cosmic-ray species from ^{4}He to ^{238}U ($2 \leq Z \leq 92$), with energies ranging from 10^{16} to 10^{20} eV, the region where we expect the Lorentz shifted giant resonance peak. Disintegration probabilities obtained are presented in Fig. 7.3, showing the value of η_Z for selected cosmic particle species, averaged over all directions. The average values of $\eta_Z \sim 10^{-6}$ for low mass particles and $\eta_Z \sim 10^{-5}$ to 10^{-4} at the

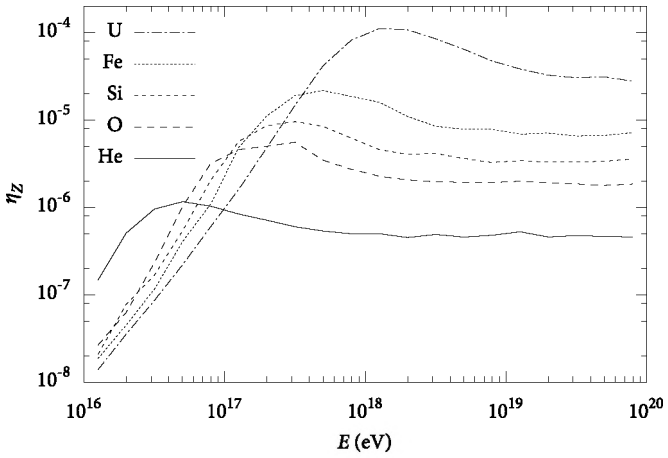

FIG. 7.3 · Average all-sky Gerasimova-Zatsepin disintegration probability η_Z as a function of energy for selected primary cosmic-ray species.

heavy end are in line with the findings of Medina-Tanco & Watson (1999) and Epele et al. (1999). The behaviour of the giant resonance peak can be identified clearly, increasing with Z both in resonance energy and magnitude. Note that the partial contribution of the heavier nuclei to the Gerasimova-Zatsepin spectrum is more significant than one might expect, due to both their high overall value of η_Z as well as a high partial flux at higher energies.

By multiplying each species' disintegration probability by its partial flux according to Eq. 7.14, the total intrinsic Gerasimova-Zatsepin flux is obtained:

$$J_{GZ}(E) = \sum_Z J_Z(E) \int \eta_Z(E, \phi_o, \theta_o) \cos\theta_o \, d\theta_o \, d\phi_o. \qquad (7.17)$$

Fig. 7.4 shows this flux as a function of energy. The solid line represents the absolute total flux by counting all disintegration events. For reference, the fraction of the integral cosmic-ray spectrum $J_o(E)$ is also drawn in the bottom panel, showing the maximum disintegration probability of $\eta_{GZ} \simeq 10^{-4}$ near $E \simeq 1.5 \cdot 10^{18}$ eV. The dashed line was obtained by disregarding any event with a separation larger than one Earth diameter. This line sets a hard upper flux limit for any Earth-based detector. Notice that events with these very high separations primarily occur in the lower energy end of the spectrum: this makes sense, as the separation of a disintegrated cosmic-ray pair is expected to be proportional to the inverse of its energy.

Not every arrival direction on the sky produces the same probability of disintegrating a particle. The left panel in Fig. 7.5 shows an all-sky map of the total Gerasi-

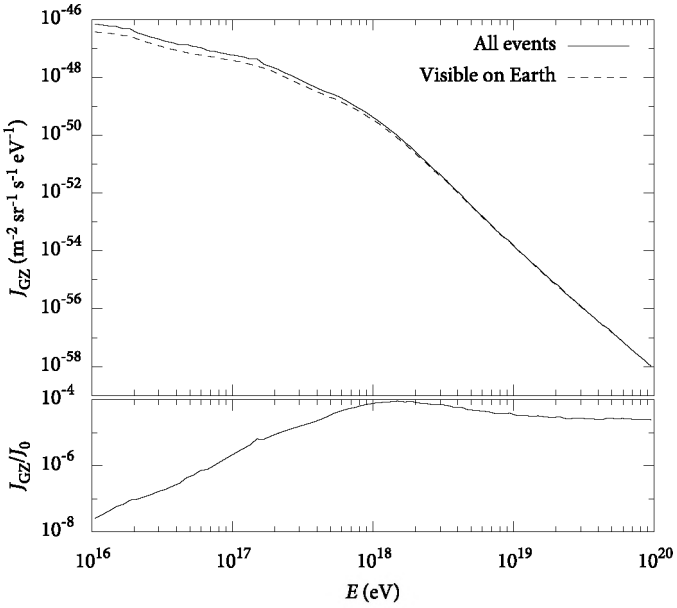

FIG. 7.4 · Absolute Gerasimova-Zatsepin energy spectrum (solid line), and upper limit for Earth-based detectors, i.e. events with $|\delta| < 2R_\oplus$ (dashed line). Also shown is the fraction of the overall galactic hadronic cosmic-ray flux J_0 in the bottom panel, showing that $10^{-8} < \eta_{GZ} < 10^{-4}$ in this energy range.

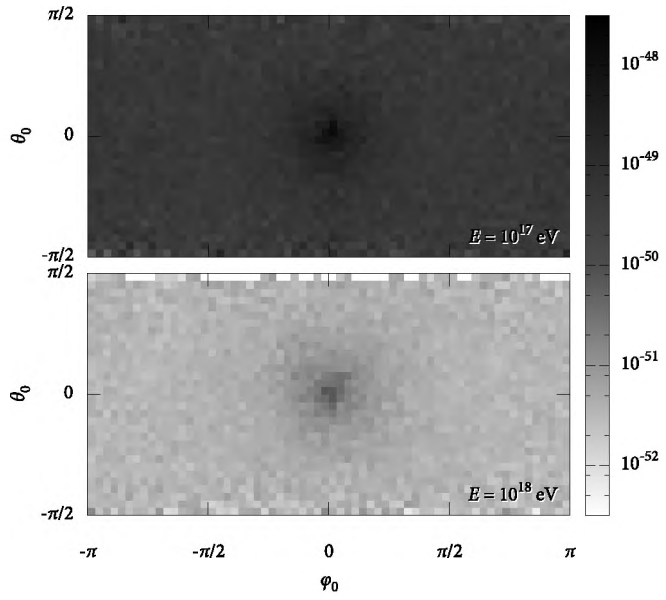

FIG. 7.5 · All-sky map relative to the Sun of the Gerasimova-Zatsepin flux. The color scale represents the total flux in events m^{-2} sr^{-1} s^{-1} eV^{-1} for energies 10^{17}–10^{18} eV (upper panel) and 10^{18}–10^{19} (lower panel). The ecliptic runs horizontal in these images ($\theta_0 = 0$), the Sun is in the centre.

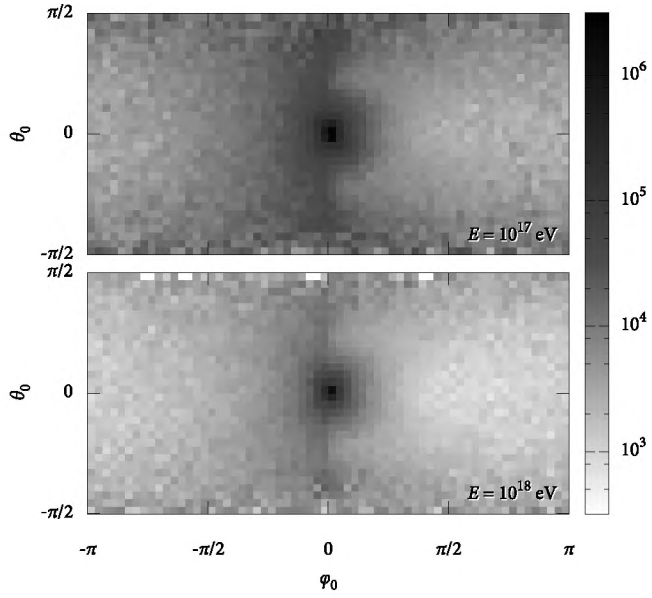

FIG. 7.6 · Similar to previous figure, now showing the average separation distance of Gerasimova-Zatsepin events. The color scale represents the mean separation distance in km.

mova-Zatsepin flux $\sum J_Z \eta_Z$ as a function of the arrival direction relative to the Sun. Two energy intervals are shown, for $E \sim 10^{17}$ eV and $E \sim 10^{18}$ eV. Clearly, the disintegration process favours arrival directions close to the Sun: this can be easily justified, as higher integrated photon densities boost the number of disintegrations in trajectories from this direction. As explained before, the overall magnitude of the disintegration flux field decreases by several orders of magnitude for each decade up in energy (compare upper and lower panel in Fig. 7.5). Its shape, however, does not depend much on primary energy.

Given the complicated structure of the magnetic field in the Solar System defined by Eqs. 7.9–7.11, an analytical approach to obtain shower separations was rejected. Instead, a numerical equivalent of the field was implemented and disintegrated particles were propagated accordingly. For the general case, when no restrictions are imposed on the final separation of the remnants, the average value of δ is shown in the right panel in Fig. 7.5. Because the parameterization of $\boldsymbol{B}$ is such that particle accelerations are identical when changing the sign of z, the behaviour of δ in terms of θ_0 is always symmetric around the ecliptic, as the figure shows. Particle trajectory deviations are clearly largest for directions near the Sun, which can be attributed to the higher magnetic field strength in this region. The region of large separations near $\phi_0 = 0$ is a result of the B_z^{dip} component of the magnetic field (Eq. 7.9). The highest event rates for any realistic cosmic particle observatory are to be expected on the night side of the sky. Separations from directions close to the Sun are just too large to be detected. This effect is so strong that it more than counteracts the increased flux from this region.

To illustrate the dependence of the separation distance on the parameters in Eq. 7.12, the distribution of δ is given in Fig. 7.7 for the same species highlighted in Fig. 7.3. All curves are normalised so that their respective logarithmic integrals equal unity; separate lines are drawn for disintegration reactions involving proton and neutron ejection. The separations shown are for a primary of $E = 10^{18}$ eV. Note that the proton and neutron curves for helium, oxygen and silicon are identical: this derives from the mass/charge ratio of exactly 2 for these species. Apart from statistical deviations, all curves are identical when separations are shifted left by a factor $A|Z_1/A_1 - Z_2/A_2|$, peaking at 40 km. Since $\delta \propto E^{-1}$, multiplying the separation value by 10^{18} eV$/E$ yields the correct separation at other energies. We may now parameterize the expectation value for the separation as

$$\langle \delta \rangle = 4A \left| \frac{Z_1}{A_1} - \frac{Z_2}{A_2} \right| \left(\frac{10^{19}\ \mathrm{eV}}{E} \right) \mathrm{km}. \tag{7.18}$$

For helium disintegration, for example, this corresponds to a distance of $\sim 10^3$ km at a primary energy of 10^{17} eV. The overall remaining shape of the separation distribution is only the result of the magnetic field shape and strength and the disintegration distance R from Earth.

Let us now estimate event rates for selected air shower experiments: the existing Pierre Auger Observatory (Abraham et al., 2004) and the LOFAR radio tele-

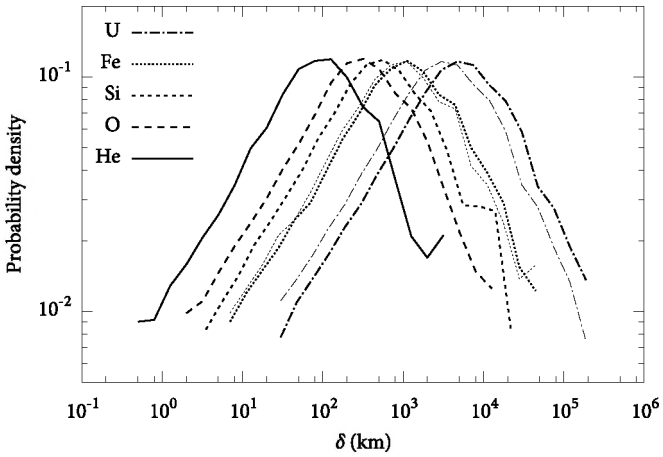

FIG. 7.7 · Distribution of separations for species of ^{4}He, ^{16}O, ^{28}Si, ^{56}Fe and ^{238}U. Thick lines are for proton emission, thin lines denote neutron emission. Shown are expected separations for a primary of $E = 10^{18}$ eV; for other energies, multiply δ by 10^{18} eV/E.

TAB. 7.8 · Detector characteristics for the Pierre Auger Observatory and the Low Frequency Array (LOFAR).

	S_o (km^2)	Location	E_{min} (eV)	f_{dc}	θ_{max}	δ_{min} (km)
Auger	3000	35.2°S, 69.3°W	10^{18}	1.0	60°	5
LOFAR	84	52.9°N, 6.9°E	10^{17}	1.0	80°	1

scope (Falcke et al., 2006), which is under construction. The detector geometries for these observatories, determining their respective $\xi(\delta)$ functions, are shown in Fig. 7.8. Auger and LOFAR are both surface detectors, sensitive to secondary shower particles (Auger) and radio signals produced in the shower (LOFAR). Pierre Auger is a dense array, covering one continuous area with detectors; LOFAR is a sparse array, consisting of many interconnected smaller stations with no detectors in between. Though LOFAR's raw surface area is much smaller, it is able to reconstruct showers with a much lower energy.

Both detectors were modelled numerically to accurately map Eqs. 7.13 and 7.16. For each detector, simulations were carried out to make predictions for the final event rates $\Phi_{GZ}(E)$ according to four scenarios, which are outlined below.

1. *Upper limit.* As a simple first step, we can set a hard upper limit by taking the

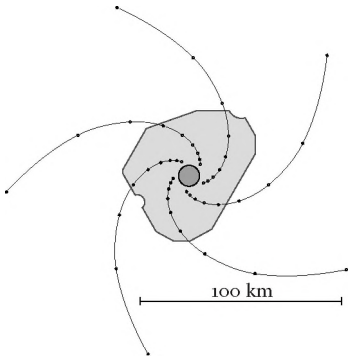

FIG. 7.8 · Detector layout of the Pierre Auger Observatory (irregular background shape), a large, dense detector; and of LOFAR (black circles), a sparse detector with less detection surface yet spread over a larger area. North is up in the figure.

observatory's total detection area S_0 as the effective cross section, implying

$$\Phi_{GZ}(E) = 2\pi S_0 \int J_{GZ}\, dE \simeq 0.45 \left(\frac{S_0}{\mathrm{km}^2} \right) \mathrm{yr}^{-1}, \tag{7.19}$$

where the approximation is made by integrating between 10^{16} and 10^{20} eV. This approach means that every event has nonzero probability of being detected, regardless of its remnants' separation.

2. *Separation constraints.* A more realistic estimate is obtained by applying the aperture function A according to Eq. 7.13. In this way, we include projection effects as a result of the detector's orientation. We also apply a lower limit $\delta_{\min}$ to the separation distance; this is the minimum separation at which the detector can disentangle two showers.
3. *Weak energy constraints.* In this scenario, the energy cut sets a lower limit $E_{\min}$ on the more energetic shower. For the less energetic shower, an energy down to a tenth of this limit is allowed. This approach is justified by the possible implementation of a triggering system in which data for the entire detector array is stored for each trigger, allowing one to check for coincidences at a later time.
4. *Strict energy constraints.* By applying a strict energy cut, demanding that both showers exceed the threshold energy, a less sophisticated trigger suffices. This scenario is probably the most reasonable assumption for current detectors, as they are not optimised for Gerasimova-Zatsepin pair detection. It is also the least promising one.

The detector characteristics used for Auger and Lofar are given in Table 7.1. Values listed for $E_{\min}$ are not taken as hard step functions. Instead, the cut-off follows a Gaussian

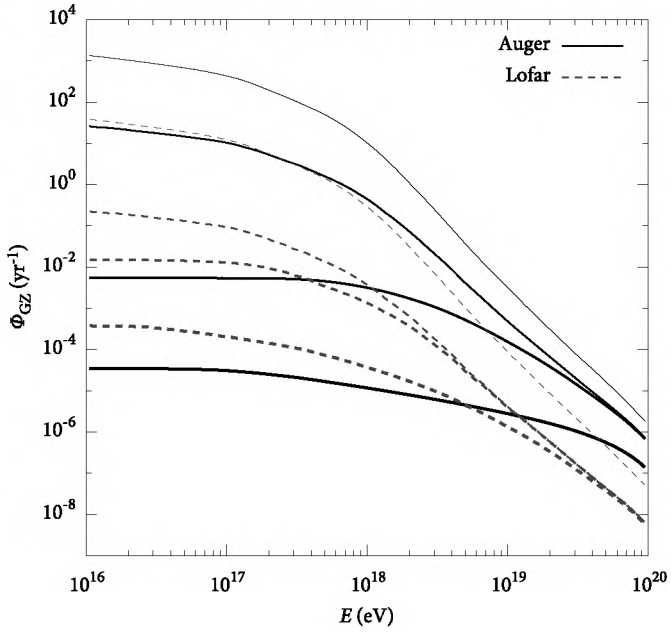

FIG. 7.9 · Expected integrated Gerasimova-Zatsepin detection rates for Pierre Auger (solid lines) and LOFAR (dashed). Four lines are drawn for each detector, representing, from top to bottom, the theoretical upper limit for a detector of the given area; applying separation cut-offs regarding detector geometry; applying loose energy cuts; and applying strict energy cuts (see text for further explanation).

error function:

$$\omega(\theta, E) = \frac{1}{2} + \frac{1}{2}\mathrm{erf}\left(a \log \frac{E}{E_{\min}}\right) \qquad \text{when } \theta < \theta_{\max}, \tag{7.20}$$

and $\omega(\theta, E) = 0$ for larger zenith angles. For Pierre Auger, a was chosen to match detector efficiency simulations from Allard et al. (2005). For LOFAR, an estimate of $a = 1.7$ was made, as no detector efficiency data is yet available.

Both detectors' $\xi(\delta)$ functions were generated numerically from the geometries in Fig. 7.8. For Pierre Auger and LOFAR, derived event rates for each scenario obtained in this way are presented in Fig. 7.9. This figure showing separate lines, from top to bottom, for scenario 1 (thin line) to 4 (thick line). The Pierre Auger Observatory is hit by a Gerasimova-Zatsepin particle more than 10^3 times per year, about 30 of which are double hits in which both particles are detectable given the detector's geometry. This rate is dominated, however, by particles with $E < 10^{18}$ eV. When the observatory's lower

energy limit is taken into account according to scenario 4, event rates plummet to levels between 10^{-5} and 10^{-4} yr^{-1} at the current trigger implementation. This figure effectively dismisses any possibility of successful Gerasimova-Zatsepin pair recording with Auger. Scenario 3 is a possibility in the case of Pierre Auger, as information for all surface detector tanks is stored when a big event is seen. Even in scenario 3, however, event rates are not expected to exceed 10^{-2} yr^{-1}.

The Low Frequency Array's detection area is about 36 times smaller than that of Auger, and consequently it has a much lower intrinsic Gerasimova-Zatsepin flux, not exceeding 0.3 yr^{-1}. LOFAR's energy limit is 10 times lower, however: this easily compensates the lack of area, as the slope of the Gerasimova-Zatsepin event rate is approximately $\propto E^{-3}$ at higher energies (see Fig. 7.9). Still, expected event rates do not exceed $5 \cdot 10^{-4}$ yr^{-1} in scenario 4. Comparing event rates from simulations of the full detector and the central core only, shows that no significant contribution to pair detection is to be expected from the relatively small outer stations. The increased rate in scenario 3, probably the maximum achievable rate for LOFAR, is still quite insignificant at $2 \cdot 10^{-2}$ yr^{-1}. As with Auger, here too the chances of the corresponding trigger algorithm being implemented are slim at best, because the LOFAR telescope will not be a dedicated cosmic-ray detector, but an experiment shared with other astronomical observations. In practice, data bandwidth limitations would probably not allow a trigger to be communicated to every antenna in the array, except for very energetic events which produce a negligible Gerasimova-Zatsepin rate.

Because the expected event rate for a cosmic-ray detector is proportional approximately to $S_0 E^{-3}$, it pays off to invest in lowering a detector's energy threshold instead of focusing on collecting area if maximising Gerasimova-Zatsepin event rates is intended. Still, any detector to receive a single detectable Gerasimova-Zatsepin event per year would have to be excessively large. At a Gaussian lower energy limit of $E_{min} = 10^{17}$ eV with full duty cycle and 60° zenith limit, for example, required aperture sizes are shown in Fig. 7.10. It is clear that much can be gained by lowering a detector's threshold down to values of $E_{min} \sim 10^{16}$ eV. The aperture needed converges to a value of $1.3 \cdot 10^3$ km^2 sr at low E_{min}, as the disintegration probability drops steeply ($\propto E^2$) at low energies. Moreover, at energies below 10^{14} eV cosmic-ray particles do not produce detectable air showers in the atmosphere. Surface detectors of the sizes and specifications discussed would be excessively and unjustifiably expensive to build, considering that only a single event would be detected per year on average.

7.6 · DISCUSSION

One technique which dramatically increases detection area at a fairly reasonable cost, is that of fluorescence detection. Detectors of this kind will not produce more favourable Gerasimova-Zatsepin detection rates, however. Their duty cycles are typically only 0.1, as they can only be used in moonless nights, increasing the area needed to obtain the same event rate by an order of magnitude over surface detectors. Moreover, the fluorescence

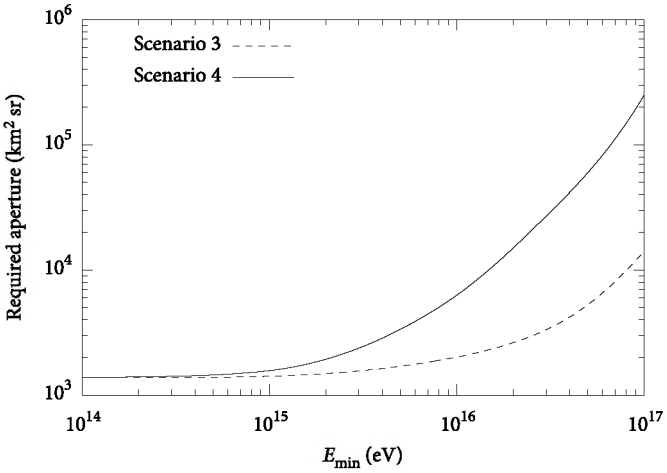

FIG. 7.10 · Required aperture for detection of a single Gerasimova-Zatsepin event per year as a function of $E_{\min}$ for a circular detector at 45° latitude, $f_{dc} = 1$, $\theta_{\min} = 60°$ and $\delta_{\min} = 1\,\text{km}$.

detection technique does not work well for low energies, where most can be gained: typically, a 10^{17} eV air shower's fluorescence signal can be seen no more than 10 km away from a fluorescence telescope. This also discards satellite missions such as EUSO as possible detectors.

For surface detectors, there might be other points to consider. Even if a cosmic-ray observatory was hit by a detectable Gerasimova-Zatsepin pair, it is very much the question whether such an event would meet quality criteria. The occurrence of two overlapping or nearly overlapping showers within a very short time window might prevent proper reconstruction, and the event would be discarded as noise.

On a side note, an interesting deviation of the pure cosmic-ray spectrum as seen by current experiments can be observed. We have shown that a fraction of $\sim 10^{-5}$ of all Galactic cosmic particles arrives at Earth as a Gerasimova-Zatsepin pair. In practice, these events go unnoticed as such and are registered as normal cosmic particles. This means that, at any given energy, a small fraction of the events is to be attributed to a primary of much higher energy. The actual spectrum then has a spectral index of the order of 10^{-5} less steep than currently assumed; this factor is too small to perceive given current data error margins.

7.7 · CONCLUSION

We have used a set of simulations to calculate in detail the spectrum of very-high-energy cosmic-ray particles breaking up in the Solar magnetic field. Our analysis confirms earlier

findings by Epele et al. (1999) and Medina-Tanco & Watson (1999) that the intrinsic probability of a compound hadronic cosmic-ray particle undergoing disintegration is of the order of 10^{-6} to 10^{-4} in the very-high-energy range, producing a significant flux of disintegrated particles.

We have calculated numerically the amount of deflection of these particles in the magnetic field of our Solar System. The final separation on Earth between the particle pair, ranging from unnoticeably small to millions of kilometers, was found to vary with primary species and energy as expected and with the disintegration position in the Solar System.

Additionally, we have used detector models to estimate realistic detection rates for this phenomenon. We have shown that current experimental setups, including the Pierre Auger Observatory, by far lack either the energy sensitivity or the area to produce any significant amount of detections of the kind, and would detect only a fraction of the Gerasimova-Zatsepin flux predicted by Epele et al. (1999) and Medina-Tanco & Watson (1999). Consequently, the prospects for any future experiment detecting a reasonable amount of Gerasimova-Zatsepin pairs are slim at best.

ACKNOWLEDGEMENTS

This work is part of the research programme of the 'Stichting voor Fundamenteel Onderzoek der Materie (FOM)', which is financially supported by the 'Nederlandse Organisatie voor Wetenschappelijk Onderzoek (NWO)'.

8 · *Summary & conclusions*

In this thesis, I investigate methods to derive properties of high-energy cosmic particles using the radio signal of the extensive air showers they initiate. I consider the entire course of a cosmic particle from its ingression into our Solar system to the short electromagnetic pulse visible by radio antennas on the Earth's surface. Along the way, I present a framework of parameterizations for the accurate and instantaneous description of electron-positron distributions in extensive air showers and the geosynchrotron radiation these particles produce as seen on the ground.

Chapter 2 describes an adaptation of the CORSIKA code to simulate extensive air showers was constructed, allowing us to perform simulations on a large supercomputer. This extension of the CORSIKA code delivers reliable results, and it has proven to run dependably on a variety of computer systems. Using this modified code, a library of air shower simulations for various cosmic-ray primaries for a wide range of energies and angles of incidence was built, resulting in multidimensional datasets of distributions and properties of secondary electrons and positrons in air showers.

Analysis of this library in chapter 3 shows that all extensive air showers show a great level of universality, making the electron-positron distributions dependent only on the atmospheric depth at which the number of particles peaks and the total number of particles present in the shower at this depth. The entire structure of the shower follows directly from these two values, independent of the energy, type and incident angle of the primary cosmic particle. Some exceptions to the universality hypothesis were found, which could theoretically be used to distinguish primaries on a shower-to-shower basis. The deviations are smaller than the statistical deviations between showers, however.

To support the simulation of secondary radiation effects from extensive air showers, such as Cherenkov, fluorescence and geosynchrotron radiation, I have also produced multidimensional parameterizations describing the electron-positron content of extensive air showers in terms of shower development stage, particle energy, momentum angle, lateral distance, and arrival time. These allow one to produce realistic distributions without the need for time-consuming air shower simulations.

Based on the principle of universality, one may conclude that it is possible by statistical means only to derive an air shower's primary particle from its electron-positron content. Since these particles are largely responsible for radiation effects in air showers, we

may extend this conclusion to geosynchrotron radiation as well. It does allow us, however, to make detailed parameterizations of the geosynchrotron pulse shapes in air showers, without the need to incorporate the particle's type. Using the REAS code to simulate the radio emission expected from our library of air showers, in chapter 4 I have constructed a unified description of the complete radio pulse induced by an extensive air shower using only its size and depth, as well as its angle with the geomagnetic field. This parameterization reduces the necessity to run simulations for radio air shower experiments, as one may gain instant access to accurate pulse shapes using this description.

In chapter 5, I have derived a connection between the relative arrival time of the radio pulse emitted by the shower front and the depth of the air shower maximum. This relation can be used to estimate the depth-of-maximum of an extensive air shower if the impact position is known or vice versa, by analyzing radio pulse arrival times of the radio antennas in an air shower array. Successful application in an experimental environment requires accurate knowledge of the arrival direction.

An important test case for the scenario of geosynchrotron emission will be provided by the LOFAR array, the novel radio telescope under construction in the Netherlands. Trigger requirements to successfully employ this array for the detection of extensive air showers were determined, and basic implementations of the desired trigger algorithms are supplied in chapter 6. Also given are estimates for the expected amount of events that will be received by the final LOFAR array.

One way around the impasse in deriving primary particle types is to look for simultaneous air shower events arriving at some distance but from the same direction. These events could be the result of compound cosmic-ray particles disintegrating in the Solar photon field. Though the occurrence of such events is found to be quite frequent in chapter 7, realistic event rates in actual air shower experiments are found to be negligible.

The research done in this thesis proves that identifying the nature of cosmic particles of the highest energies is not possible for individual occurrences when only electromagnetic effects are considered. However, it is possible to derive properties such as the number of particles in the air shower and the depth of its maximum using radio antennas. The prospects that studying cosmic particles with radio antennas will make important contributions to this are very promising.

References

Abraham, J., Abreu, P., Aglietta, M. et al., 2007; Science, 318, 938

Abraham, J., Aglietta, M., Aguirre, I.C. et al., 2004; Nuclear Instruments and Methods in Physics Research A, 523, 50

Abu-Zayyad, T., Belov, K., Bird, D.J. et al., 2001; Astropart. Phys., 16, 1

Agnetta, G., Ambrosio, M., Aramo, C. et al., 1997; Astroparticle Physics, 6, 301

Aharonian, F., Akhperjanian, A.G., Aye, K.M. et al., 2005; Science, 307, 1938

Akasofu, S.I., Gray, P., & Lee, L., 1980; Planetary Space Science, 28, 609

Albert, J., Aliu, E., Anderhub, H. et al., 2006; ApJ Letters, 638, L101

Allan, H.R., 1971; Prog. in Element. Part. and Cosm. Ray Phys., 10, 171

Allan, H.R. & Clay, R.W., 1969; Nature, 222, 635

Allan, H.R. & Jones, J.K., 1966; Nature, 212, 129

Allan, H.R. & Neat, K.P., 1967; Nature, 215, 267

Allard, D. et al., In *Proc. 29th Int. Cosmic Ray Conf.*, volume 7, p. 71 (2005)

Antoni, T., Apel, W.D., Badea, A.F. et al., 2004; ApJ, 608, 865

Antoni, T., Apel, W.D., Badea, F. et al., 2001; Astropart. Phys., 14, 245

Antoni, T., Apel, W.D., Badea, F. et al., 2002; Astropart. Phys., 16, 245

Ardouin, D., Bellétoile, A. et al., 2005; Nucl. Instrum. Meth. A, 555, 148

Askaryan, G., 1965; Sov. Phys. JETP (ЖЭТФ), 21, 658

Askaryan, G.A., 1962; J. Exp. Theoret. Phys., 14, 441

Baggio, R., Mandolesi, N., Morigi, G., & Palumbo, G., 1977; Nuovo Cimento (B), 40, 289

Baltrusaitis, R.M., Cady, R., Cassiday, G.L. et al., 1985; Nucl. Instr. Meth. A, 240, 410

Bass, S.A., Belkacem, M., Bleicher, M. et al., 1998; Prog. Part. Nucl. Phys., 41, 225

Biermann, P.L., 1993; A&A, 271, 649

Billoir, P., Roucelle, C., & Hamilton, J.C., 2007; ArXiv Astrophysics e-prints

Bleicher, M., Zabrodin, E., Spieles, C. et al., 1999; J. Phys. G, 25, 1859

Borzhkovskii, I.A., Volovik, V.D., Kobizskoy, V.I., & Shmatko, E.S., 1966; Soviet Journal of Experimental and Theoretical Physics Letters, 3, 118

Bregman, J.D., In H.R. Butcher (ed.), *Proc. SPIE Vol. 4015, Radio Telescopes*, pp. 19–32 (2000)

Buitink, S., Apel, W.D., Asch, T. et al., 2007; A&A, 467, 385

Chou, A.S. & et al., In *Proc. 29th Int. Cosmic Ray Conf.*, volume 7, p. 319 (2005)
Colgate, S.A., 1967; J. Geophys. Res., 72, 4869
Cronin, J.W., Gaisser, T.K., & Swordy, S.P., 1997; Scientific American, 276, 32
Dawson, B.R. & et al., In *Proc. 30th Int. Cosmic Ray Conf.* (2007)
Dawson, B.R. & Pryke, C.L., 1997; Proc. 25th Int. Cosmic Ray Conf., 5, 213
Dova, M.T., In *Proc. 26th Int. Cosmic Ray Conf.*, volume 1, p. 514 (1999)
Dova, M.T., Epele, L.N., & Mariazzi, A.G., 2003; Astropart. Phys., 18, 351
Elbert, J.W., Stanev, T., & Torii, S., In *Proc. 18th Int. Cosmic Ray Conf.*, volume 6 of *International Cosmic Ray Conference*, pp. 227–230 (1983)
Epele, L., Mollerach, S., & Roulet, E., 1999; Journal of High Energy Physics, 3, 17
Falcke, H. & Gorham, P., 2003; Astropart. Phys., 19, 477
Falcke, H., van Haarlem, M.P., de Bruyn, A.G. et al., 2006; ArXiv, astro-ph/0610652
Falcke, H. et al., 2005; Nature, 435, 313
Felgate, D.G. & Stubbs, T.J., 1972; Nature, 239, 151
Gaisser, T.K. & Hillas, A.M., In *Proc. 15th Int. Cosmic Ray Conf.*, pp. 353–357 (1978)
Gaisser, T.K., *Cosmic Rays and Particle Physics* (Cambridge University Press, 1990)
Gerasimova, N. & Zatsepin, G., 1960; Sov. Phys. JETP (ЖЭТФ), 11, 899
Giller, M., Kacperczyk, A., Malinowski, J., Tkaczyk, W., & Wieczorek, G., 2005a; J. Phys. G, 31, 947
Giller, M., Stojek, H., & Wieczorek, G., 2005b; International Journal of Modern Physics A, 20, 6821
Glasstetter, R., Antoni, T., Apel, W.D. et al., In *Proc. 29th Int. Cosmic Ray Conf.*, volume 6, p. 293 (2005)
Góra, D., Engel, R., Heck, D. et al., 2006; Astropart. Phys., 24, 484
Greisen, K., 1960; Ann. Rev. of Nucl. and Part. Science, 10, 63
Greisen, K., In *Proc. 9th Int. Cosmic Ray Conf.*, volume 1, p. 609 (1965)
Heck, D. & Knapp, J., 2005; *Extensive air shower simulation with CORSIKA: a user's guide*
Heck, D., Knapp, J. et al., 1998; *CORSIKA: A Monte Carlo code to simulate extensive air showers.* Technical Report 6019, Forschungszentrum Karlsruhe
Hess, V., 1912; Phys. Z., 13, 1084

Hillas, A.M., 1982; Journal of Physics G Nuclear Physics, 8, 1461
Horneffer, A., 2006; Ph.D. thesis, Rheinischen Friedrich-Willhelms-Universität Bonn
Huege, T. & Falcke, H., 2003; Astronomy & Astrophysics, 412, 19
Huege, T. & Falcke, H., 2005a; Astronomy & Astrophysics, 430, 779
Huege, T. & Falcke, H., 2005b; Astropart. Phys., 24, 116
Huege, T., Ulrich, R., & Engel, R., 2007; Astropart. Phys., 27, 392
Huege, T., Ulrich, R., & Engel, R., 2008; Astropart. Phys., 30, 96
Hörandel, J.R., 2003; Astropart. Phys., 19, 193
Jelley, J.V. & Fruin, J.H., 1965; Nature, 205, 327
Kahn, F. & Lerche, I., 1966; Proc. of the Royal Society of London (A), 289, 206
Kamata, K. & Nishimura, J., 1958; Progress of Theoretical Physics Supplement, 6, 93
Karakula, S. & Tkaczyk, W., 1993; Astropart. Phys., 1, 229
Keilhauer, B., Blümer, J., Engel, R., Klages, H.O., & Risse, M., 2004; Astroparticle Physics, 22, 249
Knapp, J. & Heck, D., 1993; Technical Report 5196B, Kernforschungszentrum Karlsruhe
Lafebre, S., Engel, R., Falcke, H. et al., 2008a; (Submitted to Astropart. Phys.)
Lafebre, S., Falcke, H., Hörandel, J., & Kuijpers, J., 2008b; Astronomy & Astrophysics, 485(1), 1
Lafebre, S., Huege, T., Falcke, H., Hörandel, J., & Kuijpers, J., 2008c; (To be submitted to Astropart. Phys.)
Lafebre, S., Huege, T., Falcke, H., & Kuijpers, J., In *Proc. 30th Int. Cosmic Ray Conf.* (2007)
Lafebre, S., Huege, T., Falcke, H., & Kuijpers, J., 2008d; (In preparation)
Mandolesi, N., Morigi, G., & Palumbo, G., 1976; J. Phys. A, 9, 815
Medina-Tanco, G. & Watson, A., 1999; Astropart. Phys., 10, 157
Müller, 2008; *A Novel Method of Determining the Energy Scale of the Pierre Auger Observatory.* Diploma Thesis, Univ. Karlsruhe
National Aeronautics and Space Administration (NASA), 1976; *U.S. Standard Atmosphere.* Technical Report NASA-TM-X-74335

Nelson, W., Hirayama, H., & Rogers, D., 1985; *The EGS4 Code System.* Technical Report 265, Stanfod Linear Accelerator Center
Nerling, F., Blümer, J., Engel, R., & Risse, M., 2006; Astropart. Phys., 24, 421
Nigl, A., 2007; Ph.D. thesis, Radboud University
Nigl, A., Apel, W.D., Arteaga, J.C. et al., 2008; A&A, 487, 781
Nishimura, J., 1965; Handbuch der Physik, 46/2, 1
Ostapchenko, S., 2006a; Phys. Rev. D, 74(1), 014026
Ostapchenko, S., 2006b; Phys. Lett. B, 636, 40
Petrovic, J., Apel, W.D., Asch, T. et al., 2007; A&A, 462, 389
Pierre Auger Collaboration & Kobal, M., 2001; Astropart. Phys., 15, 259
Pryke, C.L., 2001; Astropart. Phys., 14, 319
Risse, M., Heck, D., & Knapp, J., In *Proc. 27th Int. Cosmic Ray Conf.*, volume 2, p. 522 (2001)
Rossi, B. & Greisen, K., 1941; Reviews of Modern Physics, 13, 240
Röttgering, H., 2003; New Astronomy Reviews, 47, 405
Schmidt, F., Ave, M., Cazon, L., & Chou, A., 2008; Astroparticle Physics, 29, 355
Scholten, O., Bacelar, J., Braun, R. et al., 2006; Astropart. Phys., 26, 219
Scholten, O., Werner, K., & Rusydi, F., 2008; Astroparticle Physics, 29, 94
Song, C., 2004; Astropart. Phys., 22, 151
The euso Collaboration, 2004; Nuclear Physics B Proceedings Supplements, 136, 415
Ulrich, R., 2007; http://www-ik.fzk.de/~rulrich/coast/
Van den Berg, A.M. & et al., In *Proc. 30th Int. Cosmic Ray Conf.* (2007)
Van der Schaaf, K., Broekema, C. et al., 2004; Experimental Astronomy, 17, 43
Walker, D., 1994; Parallel Computing, 20, 657
Wilczyńska, B., Góra, D., Homola, P. et al., 2006; Astroparticle Physics, 25, 106
Woidneck, C.P. & Bohm, E., 1975; Journal of Physics A Mathematical General, 8, 997
Zas, E., Halzen, F., & Stanev, T., 1992; Phys. Rev. D, 45(1), 362
Zatsepin, G., 1951; Dokl. Akad. Nauk. SSSR (Докл. Акад. Наук. СССР), 80, 577

Samenvatting

Bijna honderd jaar geleden maakte de Oostenrijkse wetenschapper Victor Hess een reeks ballonvluchten om op verschillende hoogtes de hoeveelheid ioniserende straling te meten. In die tijd werd atmosferische ionisatie toegeschreven aan straling door radioactief verval in de Aardkorst, en men verwachtte dan ook dat de hoeveelheid ionisatie met de hoogte zou afnemen. Maar hoe hoger Hess kwam, hoe sterker de ionisatie werd. Voor zijn conclusie dat er straling met een sterk doordringend vermogen vanuit de kosmos moet komen, werd hij in 1936 met de Nobelprijs beloond. Het door Hess ontdekte fenomeen is later *kosmische straling* gaan heten, een verzamelnaam voor allerlei deeltjes met een breed energiebereik die ons vanuit het Heelal bereiken.

Vooral over kosmische deeltjes met een zeer hoge energie is nog maar weinig bekend: er is geen algemeen aanvaarde beschrijving van de bronnen van deze deeltjes, en ook de precieze aard ervan is slechts ten dele bekend. Mogelijk worden ze geproduceerd in energetische processen buiten ons Melkwegstelsel, zoals de kernen van actieve sterrenstelsels, die gevormd worden door zwarte gaten met een massa van miljoenen malen onze Zon. Wanneer kosmische deeltjes in onze atmosfeer terechtkomen, ontstaan zogenaamde cascades of *air showers* van miljoenen deeltjes. In dit proefschrift onderzoek ik de mogelijkheid om eigenschappen van hoogenergetische kosmische deeltjes te bepalen aan de hand van het radiosignaal dat in de Aardatmosfeer door cascades wordt geproduceerd. Hierbij wordt het gehele traject beschouwd vanaf het moment dat het deeltje ons zonnestelsel binnenkomt tot aan de puls die door een radioantenne kan worden waargenomen.

Allereerst wordt de deeltjescascade in detail beschouwd. In hoofdstuk 2 beschrijf ik hoe hiertoe een bestaande computercode voor het simuleren van deze cascades geschikt werd gemaakt om op supercomputers te gebruiken. Na uitgebreide controle werd dit aangepaste programma ingezet om een bibliotheek van cascadesimulaties te bouwen voor een verscheidenheid aan deeltjes bij verschillende energieën. Deze bibliotheek bevat multidimensionale histogrammen van de verdeling en eigenschappen van elektronen en positronen in duizenden gesimuleerde cascades.

Een grondige analyse van gesimuleerde data in hoofdstuk 3 leert dat alle grote cascades tot op gedetailleerd niveau een grote mate van universaliteit vertonen. Concreet betekent dit dat de distributies van elektronen en positronen erin nauwkeurig gereconstrueerd kunnen worden aan de hand van slechts twee parameters: het maximum aantal deeltjes dat zich op enig moment in de cascade bevindt en de diepte in de atmosfeer

waar dit maximum optreedt. De hele structuur van de cascade volgt direct uit deze twee parameters, onafhankelijk van de aard en energie van het primaire kosmisch deeltje. Een paar uitzonderingen op deze regel zijn gevonden, die in principe gebruikt zouden kunnen worden voor het onderscheiden van de aard van het primaire deeltje. De effecten hiervan zijn echter te klein om in een echt experiment te meten. Bovendien zijn er kleine statistische variaties in het verloop van een cascade van ongeveer dezelfde grootte, die het onmogelijk maken om deze verschillen aan te wenden.

Ter vereenvoudiging van het bestuderen van secundaire stralingseffecten in deeltjescascades, zoals Tsjerenkovstraling, atmosferische fluorescentie en synchrotronstraling, heb ik meerdimensionale wiskundige beschrijvingen opgesteld voor de distributies van de elektronen en positronen in cascades. Met deze beschrijvingen heeft men onmiddellijk toegang tot eigenschappen van deze deeltjes, zonder dat men tijdrovende simulaties hoeft te doen. Deze eigenschappen omvatten onder andere energie, bewegingsrichting, afstand tot het centrum van de cascade en tijdsvertraging ten opzichte van het deeltjesfront van de cascade.

Bij één van de eerdergenoemde stralingseffecten in cascades, namelijk synchrotronstraling in het aardmagnetisch veld, verwachten we een significant signaal bij frequenties in het radiogebied. Dit effect heb ik verder onderzocht. In hoofdstuk 4 gebruik ik simulaties van dit signaal om tot een volledige beschrijving van de aankomsttijd, tijdsduur, sterkte en vorm van de radiopuls te komen die men in een antenne kan verwachten. Deze parametrisatie is gebaseerd op twee observaties: het universaliteitsprincipe van deeltjescascades zoals beschreven in hoofdstuk 3 en het besef dat de synchrotronstraling uitsluitend het gevolg is van de interactie van de elektronen en positronen in de cascade met het Aardmagnetisch veld. Dit betekent dat de diepte van het cascademaximum, het aantal deeltjes in de cascade, de sterkte van het magnetisch veld en de invalshoek van de cascade ten opzichte van het magnetisch veld de enige variabele factoren zijn in het geproduceerde signaal. De wiskundige beschrijving die ik op grond hiervan heb opgesteld, maakt een nauwkeurige inschatting mogelijk van het opgevangen signaal in radioantennes zonder het doen van uitgebreide simulaties. Mogelijk kan ze ook gebruikt worden bij de reconstructie van gemeten cascades.

We hebben al gezien dat het niet mogelijk is direct de aard van een kosmisch deeltje te bepalen door de cascade te bekijken, maar de mogelijkheid bestaat wel om dit statistisch te doen, door van een flink aantal gemeten cascades te bepalen hoe diep

de gemiddelde doordringing in de atmosfeer is. In hoofdstuk 5 onderzoek ik de mogelijkheid om deze diepte te meten door de analyse van het verschil in aankomsttijd van het radiosignaal in verschillende antennes op de grond. Dit blijkt inderdaad te kunnen, doordat het front van de radiostraling die door de cascade wordt opgewekt geen vlakke golf is, maar op een zeer specifieke manier gekromd. Uit de sterkte van deze kromming blijkt men een uitermate goede schatting voor de diepte van het maximum van de cascade in de atmosfeer te kunnen maken. Een geslaagde toepassing van deze techniek valt of staat met een nauwkeurige bepaling van de aankomstrichting van het primaire kosmisch deeltje en de plaats van inslag van de cascade.

Een belangrijke test voor het scenario van geosynchrotronstraling uit deeltjescascades zal binnenkort geleverd worden door een radiotelescoop die momenteel in aanbouw is rond het Drentse Exloo. Deze telescoop, de *Low Frequency Array* of LOFAR, bestaat uit vele, simpele radioantennes die samen de gevoeligste radiotelescoop ter wereld zullen vormen. Om deze telescoop geschikt te maken voor de detectie van kosmische deeltjes is een gecompliceerde set algoritmes nodig die de datastroom van elke antenne naspeurt op pulsen. Het voorkomen van zulke pulsen in meerdere antennes binnen een bepaald gebied kan wijzen op het passeren van een deeltjescascade. In hoofdstuk 6 worden de voorwaarden beschreven waaraan deze algoritmes moeten voldoen. Ook geef ik een schatting voor het aantal cascades dat we zullen zien met LOFAR.

Is er dan geen enkele manier om de aard van kosmische deeltjes op individuele basis te bepalen? In hoofdstuk 7 behandel ik een mogelijke omzeiling van dit probleem, die ligt in het detecteren van twee cascades die ons op verschillende plekken op Aarde tegelijkertijd bereiken vanuit dezelfde richting. Deze cascades zouden afkomstig kunnen zijn van één kosmisch deeltje dat onder invloed van het stralingsveld van de Zon al ver van de Aarde uiteengevallen is in twee kleinere kernen. Door te kijken naar de verhouding in energie van deze twee deeltjes, kan onmiddellijk gereconstrueerd worden wat het atoomgetal van het oorspronkelijke kosmisch deeltje was. Hoewel dit fenomeen behoorlijk vaak blijkt voor te komen, maken de grote afstand en grote energieverhouding van de twee cascades het vrijwel onmogelijk dit effect te meten.

Het blijkt dus niet eenvoudig om direct iets over de aard van de hoogstenergetische kosmische deeltjes te zeggen. Indirect kunnen we echter toch belangrijke eigenschappen afleiden. Het ziet ernaar uit dat de nieuwe detectiemethode met radioantennes hier een belangrijke bijdrage aan kan leveren.

Acknowledgments

This thesis would not have been possible without the help, effort, and motivation of many, all of whom are entitled to more than this short testament of my gratitude. In spite of that, I will try.

First of all, let me express my thanks to my supervisors for keeping me on track. Jan's enthusiasm and energy and Heino's ambition and creativity have been a great inspiration to me. I also acknowledge my collaborators in Nijmegen and Karlsruhe, who were always prepared to listen to my ignorant ideas, moulding them into clever ones. Most of all, I am indebted to Jörg, Ralph, and Tim for their never-ending support and assistance.

The people of the young and blossoming Dept. of Astrophysics in Nijmegen have provided me with the stimulating and lively environment which made my time here so enjoyable. Special credit goes to Joachim, Stijn, and Gijs for their excellent company over a mug of coffee or a glass of beer. Some truths are universal, even after five hundred years.

I would like to thank my parents for encouraging me to pursue my current career. I also thank my friends and family who have been supportive of me in some way through the years, even if they don't realise it.

Lastly my wife Carlijn, who has always been my refuge, deserves more recognition than I could ever put down in words.

NIJMEGEN
JULY 2008

Curriculum vitæ

Sven Jacob Lafebre was born on the 7th of April 1980 in Tilburg, the Netherlands. He attended primary school there and, following this, secondary school at VWO level at the Cobbenhagencollege.

In 1998, he moved to Nijmegen to enroll in the Physics and Astronomy programme of the Katholieke Universiteit Nijmegen. During his studies, he was involved in students' association Marie Curie, primarily responsible for the society's periodical and web site. In the master phase of his study, he specialised in the computational aspects of physical research, and he set up an online learning environment for physics students. He switched to astronomy in 2002, which resulted in a master's thesis on differential rotation in main sequence stars, supervised by Prof. Paul Groot.

In 2003, he was offered a position as a graduate student with Prof. Heino Falcke and Prof. Jan Kuijpers at the Dept. of Astrophysics at Radboud University. You are now holding the result of his work there. During his time as a PhD student, he was invited to work with Prof. Bo Thidé for two months at the Institutet för Rymdfysik in Uppsala, Sweden on a special stipend in 2005. He also presented his work at numerous international conferences and workshops in Europe, Asia and the United States.

Currently, Sven is employed as a postdoctoral fellow at the Institute for Gravitation and the Cosmos at the Pennsylvania State University, where he works on neutrino detection with the IceCube telescope at the South Pole.